Title

Facilitating Interfacial Processes for Specific Ion/Molecule Recovery

Permalink

https://escholarship.org/uc/item/287418wz

Author

Iddya, Arpita

Publication Date

2022

Peer reviewed|Thesis/dissertation

UNIVERSITY OF CALIFORNIA

Los Angeles

Facilitating Interfacial Processes for Specific Ion/Molecule Recovery

A dissertation submitted in partial satisfaction of the

requirements for the degree Doctor of Philosophy

in Civil Engineering

by

Arpita Iddya

2022

ABSTRACT OF THE DISSERTATION

Facilitating Interfacial Processes for Specific Ion/Molecule Recovery

by

Arpita Iddya

Doctor of Philosophy in Civil Engineering

University of California, Los Angeles, 2022

Professor David Jassby, Chair

Water stress, resource scarcity, and the interdependency of food, water, and energy sectors highlight the need for developing and improving efficient resource and water management practices. While current wastewater management practices treat large volumes of wastewater and can remove nutrients that would otherwise be released into and pollute the environment, they do not meet the current needs to close the nutrient cycle and effectively recover nutrients present in wastewater. Currently, biological removal and chemical precipitation are the two most common methods employed for nutrient recovery, however, these processes are highly susceptible to feed compositions, temperature, and diurnal variations, and recover nutrients such as nitrogen or phosphorus, as nitrogen gas or struvite, a slow-release fertilizer of low commercial value. To this end, membrane-based wastewater treatment processes have emerged as an efficient alternative to remove and recover these nutrients.

In this work, we develop two novel membrane-based treatment technologies to effectively recover nutrients in their usable form as NH_4^+ and PO_4^{3-}. We first developed an electrically conducting membrane to facilitate interfacial reactions at the membrane surface and recover ammonia from wastewater, while in the second project, we developed a novel ion exchange membrane capable of selectively transporting phosphate ion over other common ions by leveraging intermolecular interactions between the ion and membrane.

The results demonstrate that ammonia was effectively recovered using our novel membrane and setup. Moreover, the process developed here reduced the overall energy consumption by 50% compared to traditional processes. The results also show that the ion exchange membrane is capable of highly efficient phosphate ion separation with a selectivity of up to a 100 compared to other competitive ions in solution.

The dissertation of Arpita Iddya is approved.

Sanjay K. Mohanty

Jennifer Ayla Jay

Eric Hoek

David Jassby, Committee Chair

University of California, Los Angeles

2022

DEDICATION

This dissertation is dedicated to my parents. I would not be who I am, or achieved what I have without your continued guidance, support, and love. I consider myself immensely lucky to have you as my rock. Love you mom and dad!

ACKNOWLEDGEMENTS

Contents

LIST OF FIGURES

LIST OF TABLES

VITA

2015   Master of Science in Chemical Engineering

Carnegie Mellon University, Pittsburgh, PA, USA

2013   Bachelor of Engineering in Chemical Engineering

B.M.S. College of Engineering, Visweswaraya Technological University

JOURNAL PUBLICATIONS

Arpita Iddya, Piotr Zarzycki, Ryan Kingsbury, Charmaine Khor, Shengcun Ma, Jingbo Wang, Ian Wheeldon, Zhiyong Jason Ren, Eric M. V. Hoek, David Jassby, *Under Review: Nature Nanotechnology, 2022*

Shengcun Ma, Fan Yang, Xin Chen, Chia Miang Khor, Bongyeon Jung, **Arpita Iddya**, Gaurav Sant, David Jassby, Water Research, Volume 204, 2021, 117592, ISSN 0043-1354

Yonas Zeslase Belete, Vivian Mau, Reut Yahav Spitzer, Roy Posmanik, David Jassby, **Arpita Iddya**, Nazih Kassem, Jefferson W. Tester, Amit Gross, Bioresource Technology, Volume 333, 2021, 125164, ISSN 0960-8524

Arpita Iddya, Unnati Rao, Jingbo Wang, Yiming Su, David Jassby, Advances in Water Desalination Technologies, 529-581

Unnati Rao, **Arpita Iddya**, Bongyeon Jung, Chia Miang Khor, Zachary Hendren, Craig Turchi, Tzahi Cath, Eric M. V. Hoek, Guy Z. Ramon, and David Jassby, Environmental Science & Technology, 54 (6), 3678-3690

Arpita Iddya, Dianxun Hou, Chia Miang Khor, Zhiyong Ren, Jefferson Tester, Roy Posmanik, Amit Gross, David Jassby. *Environmental Science: Nano 2020*, 7 (6), 1759-1771

Dianxun Hou, **Arpita Iddya**, Xi Chen, Mengyuan Wang, Wenli Zhang, Yifu Ding, David Jassby, and Zhiyong Jason Ren. *Environmental Science & Technology* **2018** *52* (15), 8930-8938

Dianxun Hou, Tian Li, Xi Chen, Shuaiming He, Jiaqi Dai, Sohrab A. Mofid, Deyin Hou, **Arpita Iddya**, David Jassby, Ronggui Yang, Liangbing Hu, Zhiyong Jason Ren. *Science Advances. Vol 5 no.8* **2019**

Tang, L.; **Iddya, A**.; Zhu, X.; Dudchenko, A. V; Duan, W.; Turchi, C.; Vanneste, J.; Cath, T. Y.; Jassby, D. Enhanced Flux and Electrochemical Cleaning of Silicate Scaling on Carbon Nanotube-Coated Membrane Distillation Membranes Treating Geothermal Brines. *ACS Appl. Mater. Interfaces* **2017**, acsami.7b12615.

Duan, W.; Chen, G.; Chen, C.; Sanghvi, R.; **Iddya, A**.; Walker, S.; Liu, H.; Ronen, A.; Jassby, D. Electrochemical Removal of Hexavalent Chromium Using Electrically Conducting Carbon Nanotube/polymer Composite Ultrafiltration Membranes. *J. Memb. Sci.* **2017**, *531* (March), 160–171.

PATENTS

U.S. Provisional Application No. 63/240,682

CONFERENCE PRESENTATION

Highly efficient ammonia recovery from wastewater using electrically conducting gas-stripping membranes. *ACS National Meeting, Fall 2019, San Diego, CA.*

*Reverse Selective Ion Exchange Nanocomposite Membrane: Selective Phosphate Recovery via an Outer Sphere Complexation Diffusion Pathway. *ACS National Meeting, Spring 2022, San Diego, CA.*

Chapter 1:

Introduction

1.1. Water and resource scarcity

Water is a finite resource crucial for human survival and sustainable growth.[1,2] However, increasing water demand due to rapid urbanization, climate change, and increasing population has left about ~30% of the world population under water-stress, of which about 733 million people live in high or critically water-stressed countries.[1,2] To sustain the worlds growing population, it is necessary to meet the growing demands for food and fresh water.

Currently, about three quarters of the fresh water supply is consumed by the agricultural industry, further adding to the increasing water-stress inequitably distributed across different countries.[1,3,4] Owing to the increasing demand for water, fresh water is increasingly sourced by overdrawing from groundwater aquifers, depleting them and also causing seawater intrusion.[5] Therefore, it is imperative to look beyond the traditional fresh water sources for consumption. As a result, there has been a significant shift in the cultural zeitgeist to not only look towards unconventional water sources (such as seawater, brackish water etc.) as well as technologies to obtain fresh water, but also improving existing wastewater management practices for direct application and reuse.

One of the main technologies that gained sufficient momentum is desalination.[6–8] With the oceans containing about 97% of the Earth's water, seawater desalination emerged as an attractive source of a virtually unlimited supply of water.[9] Interest in desalination began in the late 1950s and early 1960s.[10] Although the process currently accounts for a small fraction of the world's potable water supply, the global desalination market has been increasing over the years, estimated to be about 148 million cubic meter per day by 2030.[11–15]

1.2. Food-Water-Energy Nexus

To feed the growing population and specifically the increase in proportion of meat in many diets, global grain production increased three folds over a period of 40 years from 1950 to 1990. This

2

seemingly herculean task of providing enough food for the booming population was possible primarily due to mineral fertilizers.[16] During the same 1950-1990 period, worldwide fertilizer and pesticide use increased tenfolds.[17] Owing to rapid urbanization, and population and economic growth there is an increased pressure on water, energy and food resources.[18,19] The food-water-energy nexus highlights the complicated interdependency of these sectors and signifies the importance of an integrated approach for resource management and recovery.[20–22] Our dependence on fertilizers for food production has led to two major concerns, reliance on non-renewable resources and disruptions to natural mineral cycles.[16,23–25] It is estimated that by 2030 the demand of food will increase by up to 35% leading to further concerns over limited resource availability.[18,19]

Nitrogen (N) and phosphorus (P) are two major ingredients in most commercial fertilizers. The demand for N, P and K (potassium) fertilizers, between 2014-2018, increased annually by 1.4, 2.2 and 2.6% respectively.[26] According to the planetary body framework, which predicts the risk that human activities can destabilize the Earth system at the planetary scale, biogeochemical flows such as the N and P cycles have already reached levels of high risk capable of destabilizing the planet.[27] The high levels of uncertainty can primarily be attributed to the excessive and indiscriminate use of N & P fertilizers.[27] This further results in food and agricultural industry producing high-strength wastewater streams that contain large amounts of these nutrients as well as organic. Although vital, if released in excess these nutrients can lead to eutrophication and harmful algal blooms in receiving water bodies, which lead to depletion in the dissolved oxygen content in water and a decline in aquatic life.[17,28,29] Furthermore, nitrate contamination of aquifers, due to fertilizers, is widespread in many regions of the world and is associated with methemoglobinemia in children as well as gastric, bladder and esophageal cancers in adults, if consumed.[17] As a result, continuous

efforts have been made at developing technologies to remove excess nutrients from wastewater streams.

Increasing demand for phosphorus, a nonrenewable resource, are depleting its natural reserves and is estimated to be over within the next century.[26,30] However, phosphate is an irreplaceable nutrient essential for plant and animal growth and a key ingredient in fertilizers required to increase crop yields.[31] Therefore, it has become imperative to augment existing wastewater treatment practices to recover and recycle phosphate present in wastewater streams.[32–34] Increasing interest in process sustainability, and growing resource and water scarcity has driven the need for recovery of valuable products from wastewater streams. High strength wastewater streams can be employed to recover nutrients that can be reused as fertilizers and/or other chemicals.[30,35–37] Nutrient recovery could be more advantageous over nutrient removal as it can minimize the environmental footprint of the wastewater treatment process, and decrease dependence on natural resources, and produce nutrient based fertilizers.[38]

Conventional processes such as Annamox and nitrification/denitrification require microorganisms to convert nitrogen present in wastewater, as ammonium, to nitrogen gas which wastes this resource.[28,39] Moreover, the process is dependent on temperature sensitive bacteria, reducing the process efficiency and consequently the energy efficiency. Biological nutrient recovery (BNR), an alternative treatment method, can lead to formation of harmful greenhouse gases, making the process unsuitable for nutrient recovery.[39] Owing to high efficiency and stability of the process, chemical precipitation is the most commonly implemented method for nutrient recovery.[38] All the aforementioned processes are, however, susceptible to changes in feed composition, diurnal variations in temperature, and suffer from sludge disposal problems.[33,40] When we look at phosphorus removal/recovery, chemical precipitation and biological recovery are most commonly

4

employed for the process.[41] However, both these processes remove phosphorus along with other waste products, and do not effectively recover valuable phosphorus. Chemical precipitation of phosphorus involves addition of chemicals (iron or aluminum salts) to wastewater. This increases the operational cost in dealing with chemicals and managing disposal. The chemical precipitate can also accumulate in the sludge, adding to the operational costs in treating the excess sludge. Moreover, since the volume of the treatment system is limited, large treatment reactors are required in order to maintain the amount of biological sludge produced.[42]

Currently, wastewater treatment processes focus on nutrient removal and are highly dependent on energy availability. For instance, aeration of wastewater during aerobic treatment (nitrification) requires significant energy input; the nitrogen gas produced during the nitrification-denitrification treatment is then converted to ammonia for further use. Electro-oxidation of ammonium and ammonia ions to generate effluent nitrogen is an attractive option, however it leads to similar problems faced with biological treatment with the production of harmful gases and the increase in overall energy required to convert nitrogen gas to ammonia by the energy intensive Haber Bosch process, which accounts for about 2% of world's energy requirement.[43–45] Thus, it would be beneficial to directly extract ammonia from the wastewater streams. Moreover, for wastewater treatment plants, operation and maintenance account for approximately 24-36% of the total energy requirement, making it imperative to find alternative low energy wastewater treatment processes.[46–49] Thus, an ideal process would work at the intersection of efficient water production, nutrient recovery, and energy consumption.

Membrane based separation processes show potential for recovery owing to their high ion rejection properties.[24,38] Membrane-based processes such as nanofiltration (NF), membrane distillation (MD), reverse osmosis (RO), forward osmosis (FO), and electrodialysis allow for concentration

of nutrients from wastewater stream. For instance, superior rejection of ammonium ions by RO membranes allows for their concentration from source-separated urine[24,50] and ED allows for recovery of nitrogen using gas separation membranes with about 90% recovery.[44,51,52]

1.3. Membrane technology

A membrane is essentially a barrier that allows for specific transport of a particular species in the presence of a driving force such as pressure gradient, vapor partial pressure gradient, concentration gradient, or electrical potential gradient.[53,54] Membranes are used in a broad range of applications where the permeation rate of a specific chemical species needs to be controlled, from water treatment to batteries, pharmaceutical applications, air quality control etc.[55] The field of membrane science has seen significant improvements and developments since its conception in the 18th century. Based on their internal structure polymer membranes can broadly be classified into two categories:

1. Isotropic membrane: Isotropic or symmetric membranes have a homogenous chemical composition and have a rigid structure with randomly distributed interconnected pores (Figure 1A-C).[56] The pore size ranges from 0.01- 10 um in diameter, and separation is highly influenced by the pore size distribution.[53,54] Microporous membranes, nonporous dense membranes, and ion exchange membrane all fall under category.

2. Anisotropic membrane: Anisotropic or asymmetric membranes consist of a layered structure with changing pore size and porosity over the entire thickness (Figure 1D-F). These membranes comprise of a thin surface layer, which provides the advantage of high fluxes, supported on a thicker microporous layer. Loeb-Sourirajan membranes, composite membranes, and liquid can be categorized as anisotropic membranes.[53,54,56]

6
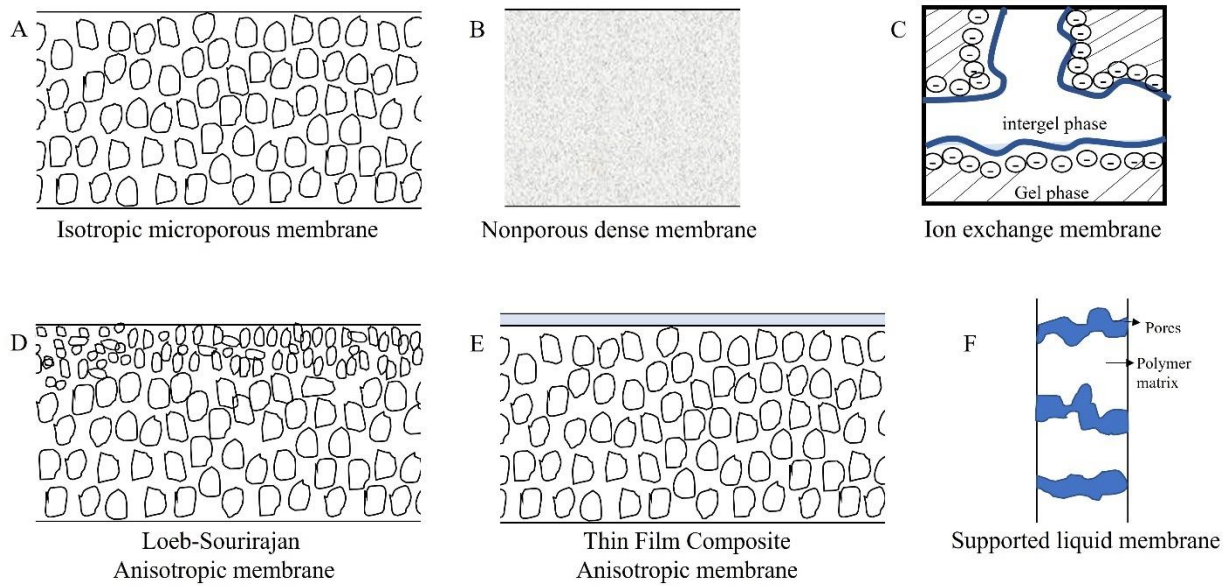
Figure 1: Schematic representation of types of polymeric membranes

Solute transport in membranes is described using two models- solution diffusion model and the pore-flow model.[55] In the solution-diffusion model, the permeant/solute sorb into the membrane on the feed side, diffuse through the membrane along the concentration gradient, and then desorb on the other side. Separation is achieved due to the difference in solubilities and diffusion rates of the permeants within the membrane. On the other hand, in pore-flow model the permeant/solute is transported across the membrane due to pressure driven convective flow through pores. Separation is primarily achieved through size-based exclusion that allows permeants smaller in size than the pore diameter to pass through and retains the larger permeants.

1.3.1. Gas Separation Membranes & Membrane Contactors

Gas separation membranes, as the name suggests, are used to separate gasses from mixed streams. Both porous and dense membranes can be used for selective gas separation; where the membrane essentially acts a selective barrier between the two phases/ components, the feed and the permeate,

and separation is achieved based on the difference in partial pressures on either side, attributed to a difference in chemical potential.

The movement of the solute through the membrane along the gradient can be explained by three transport mechanisms.[55,57] The membrane material plays an important part in determining the transport mechanism. Dense polymeric materials generally have transport taking place by solution-diffusion mechanism, based on Fick's law.[58] For microporous membranes, transport is given by either Knudsen diffusion, selective surface flow, molecular sieving or a combination of these mechanisms.[55,58] The Knudsen number is generally used to identify the correct mode of transport. The Knudsen number is given by:

$$K_n = \frac{\lambda}{d_p} \tag{1}$$

Where, λ is the mean free path of molecules and d_p is the diameter of the pores. If the $K_n > 10$, implying that the collision between molecules is much less than collision between molecules and the wall thus Knudsen diffusion is dominant. When $K_n < 0.1$, the collision between molecules dominates, thus Knudsen diffusion becomes negligible, and the transport is dominated by molecular diffusion. Finally, for when $0.1 < K_n < 10$, the transport mechanism is a combination of the mechanisms as mentioned above.[58]

Membrane Contactors

A membrane contactor is a partitioning device that promotes contact between two fluid phases. The membrane itself does not provide any selectivity to the separation process as it only serves as a physical barrier separating the two phases (as shown in Figure 2) and to increase surface area for mass transfer between the two phases. The small pores in the membrane exert capillary forces that prevents direct mixing of the phases on either side of the membrane. Thus, membrane contactors

are used to increase the fluid-fluid interfacial surface via the membrane pores.[55,59] The driving force of this membrane process lies in the difference of the partial pressure of the species between the feed and receiving chamber/solution.[60]
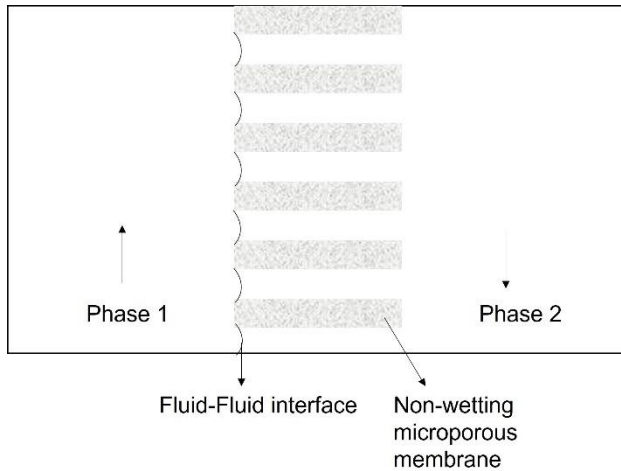
Figure 2: Membrane contactor working principle

By carefully controlling the pressure difference across the membrane, it is possible to immobilize the fluid-fluid interface at the mouth of the pore.[60,61] Contactors can be used to separate gases and liquids (liquid/gas contactor as in Figure 3 A&B), two immiscible liquids (liquid/liquid contactor as in Figure 3C) or two miscible liquids (as in membrane distillation as shown in Figure 3D).
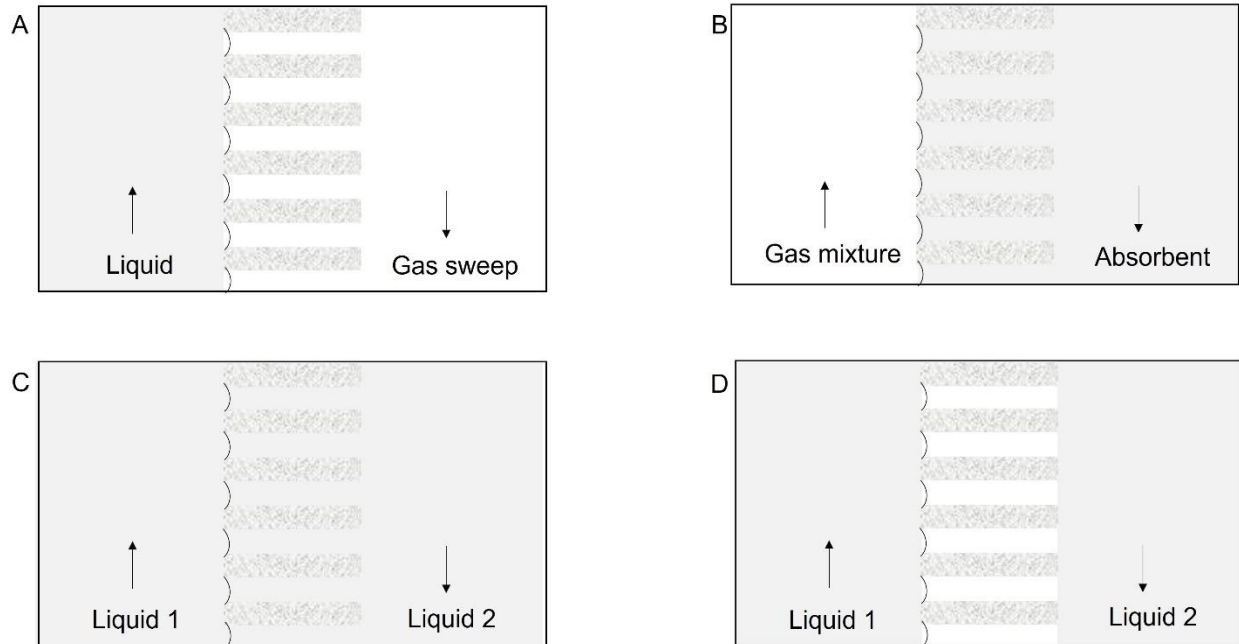
Figure 3: Applications of membrane contactors. A) The membrane contactor is used to separate dissolved gases from solution into the gas sweep, B) Membrane contactor used to facilitate gas dissolution into liquid, C) Separating two immiscible liquids to remove dissolved gases from one solution, and D) Membrane contactor separating two miscible liquids to allow gas transfer from one solution to another.

As seen in Figure 3, the pores in membrane contactors are filled with one of the two fluid phases and determines the breakthrough pressure of the membrane. The breakthrough pressure is the minimum pressure required for one phase to go through the membrane pores to the other side of the membrane. This pressure is calculated assuming that the pores are ideal cylinders:

$$P_c = \frac{4\,\gamma\,cos\theta}{d_p} \qquad (2)$$

Where, P_c is the breakthrough pressure, γ the interfacial tension, θ the contact angle of the liquid to wet the membrane, and d_p the average pore diameter. If the transmembrane pressure (pressure applied across the membrane) is greater than the breakthrough pressure, the liquid will go through the membrane pores.[60]

10

Gas/liquid membrane contactors (Figure 3A&B) can be operated in of two modes: wet mode and dry mode. For dry mode operation (using hydrophobic membrane), the gas phase in present in the pores as in figure 3A; whereas for wet mode operation, for instance when using hydrophilic membranes, the liquid phase in present in the pores (Figure 3B).[61] Generally dry mode operation is preferred due to higher gas diffusivities.

The major resistance to mass transfer in membrane contactors occurs at the liquid-membrane interface.[55] The simplest mass transfer model developed is given by resistance-in-series model. The model assumes that the resistance to mass transfer is occurring only in films of fluid close to membrane interface as well as within the membrane. The solute encounters three resistances in its transfer from the feed to the receiving phase. The resistance in each phase, i.e., the resistance at the feed-side boundary layer, within the membrane, and the receiving phase boundary layer are represented by the inverse of a the individual mass transfer coefficient; and the overall resistance is given by the inverse of an overall mass transfer coefficient.[60,61]

Equation 3 gives the overall mass transfer coefficient ($K_{overall}$) for a gas/liquid membrane contactor:

$$\frac{1}{K_{overall}} = \frac{H_A}{k_g} + \frac{1}{k_m} + \frac{1}{k_l} \tag{3}$$

Where, H_A is the Henry's constant for solute A, k_g is the mass transfer coefficient tin the gas phase, k_m is the mass transfer coefficient in the membrane, and k_l is the mass transfer coefficient in the liquid phase. For a liquid/liquid membrane contactor using a hydrophobic membrane with water on either side (Figure 3D), the overall mass transfer coefficient ($K_{overall}$) is given by:

$$\frac{1}{K_{overall}} = \frac{1}{k_{lF}} + \frac{1}{k_m} + \frac{1}{k_{lR}} \tag{4}$$

11

Where, k_{lF} is the mass transfer coefficient in the liquid on the feed side and k_{lR} is the mass transfer coefficient in the liquid in the receiving side.[61]

1.3.2. Ion Exchange Membranes

Electrically charged membranes can be either nonporous dense films or microporous structures consisting of positively or negatively charged ions decorated on the membrane walls.[56] Ion exchange membrane (IEMs) are one of the most advanced separation membranes.[62] IEMs are a class of dense polymeric membranes that have gained interest due to their application in electromembrane processes, as they can allow for selective recovery of nutrients and/or resources.[63,64] In addition to electromembrane processes such as electrodialysis (ED) and Donnan dialysis (DD), IEMs are also considered key components in battery technology with emerging applications in energy generation (reverse electrodialysis, RED), and desalination in membrane capacitive deionization (MCDI) and reverse osmosis (RO).[64] With increasing usage of ion exchange membranes superior ion exchange properties are desired. Low electrical resistance, high ion exchange capacity, good mechanical and chemical stability, and high permselectivity between co- and counter-ions (and between different counter-ions) are important properties governing membrane performance.[64]

These membranes have fixed charges, imparted by the functional groups of the ion exchange resin, affixed to the polymeric backbone of the membrane material. Based on the charge of these functional groups present, IEMs can be classified into two groups: (i) cation exchange membranes (CEM) with negatively charged functional groups attached to the polymer matrix, and (2) anion exchange membranes (AEM) with positively charged groups attached to the polymer matrix. In these membranes, the fixed ions on the polymer backbone are in electrical equilibrium with the mobile ions, called counter-ions, being transported across the membrane. The mobile co-ions (ions

carrying the same charge as that of the fixed ion), are excluded from the membrane matrix due to Donnan exclusion (or charge exclusion, i.e., solute with the same charge as the ions on the membrane walls is rejected by Coulombic repulsion). Consequently, CEMs are preferentially permeable to cations while AEMs are preferentially permeable to anions.[65,66]

The internal structure of IEMs determines the passage of ions and as a result, its performance in application. Based on the interconnectivity of their charged groups, IEMs can be classified as either homogeneous or heterogeneous membranes.[65,67,68] Homogeneous membranes have an even distribution of charged groups within the matrix and are prepared by introducing ion-exchange moiety into the structure of polymer. Heterogeneous membranes, on the other hand, are prepared by dispersing ion exchange resin powder in a binder polymer, this results in the clustering of ion exchange resin groups and an uneven distribution within the membrane matrix. As a result, heterogeneous membranes have higher electrical resistance, owing to the longer pathway of the mobile ion within the heterogeneous structure, and lower permselectivity due to leakage of co-ions through the water filled gaps in the membrane.[65,67] Permselectivity, an important parameter that judges the performance of IEMs, characterizes the degree to which co-ion passage is prevented by IEMs. An ideal IEM would have a permselectivity of unity, while a non-permselective membrane has a permselectivity of zero.[69]

Ion sorption and transport phenomenon through IEMs has primarily been explained by Donnan theory in literature. As stated by Donnan in his paper on theory of membrane equilibria[70] and reiterated by Luo et. al. in their 2018 review on selectivity in ion exchange membranes[64], Donnan treated the IEM matrix as a solution with homogeneously distributed fixed charges to derive the thermodynamic equilibrium equations. Thus, there exists a potential difference between the solutions separated by the IEM which induces ion migration leading to equilibrium. This electric

potential developed at the solution-membrane interface is responsible for co-ion exclusion, called Donnan effect.[70] Donnan theory thus explains the converse relation between fixed charge density and co-ion sorption in the membrane phase, and the dependence of co-ions in the membrane phase on external electrolyte concentration. However, there exists few discrepancies between the theoretical and the observed experimental co-ion sorption. These discrepancies have been historically attributed to the heterogeneous microstructure of the membranes.[64,70]

To account for heterogeneities in IEM transport properties, three types of models have been suggested to describe the membrane microstructure. (i) The classical model (also used by Donnan theory), considers the membrane as a homogeneous solution[70], (ii) the second model accounts for the structural inhomogeneity and includes the cluster-channel network model of Nafion[71,72], and finally, (iii) the third model, called the microheterogeneous model, divides the membrane into two phases[73]- the gel phase composed of the polymer chain and the attached ion exchange groups, and the interstitial (also called intergel) phase consisting of the void between the gel phase, assumed to be filled with electroneutral solution for a hydrated membrane.[64,72,73]

Ion transport mechanism

Ion transport in IEMs can be best approximated by studying H^+ transport in proton exchange membranes as ion transport mechanisms are complicated and proton transport is the most complex. Theoretically, the extended Nernst Planck equation is used to describe ion flux as:

$$J_i = (vC_i) - \left(D_i \frac{dC_i}{dx}\right) - \left(\frac{z_i F C_i D_i}{RT} \frac{d\varphi}{dx}\right) \tag{1}$$

where v is the convective velocity of the solvent, C_i, D_i, and z_i are the concentration, diffusion coefficient, and valence of ion i, respectively, and x is the distance coordinate across the membrane. The equation describes the three possible mechanisms for ion transport- (i) convection,

represented by the first term in brackets in equation 1, is the convective transport of ions imposed by electro-osmotic solvent transfer, (ii) diffusion, represented by the second term, and (iii) electromigration, given by the third term representing ion migration due to the electric potential gradient. In addition to the aforementioned transport mechanisms, surface site "hopping" of counter-ions from one fixed site to the next is another possible mechanism for ion transport. However, considering that the extended Nernst Planck equation does not contain a term account for ion "hopping", it might suggest that the contribution from diffusion and electromigration to ion migration far exceed that from surface site "hopping". Therefore, surface site "hopping" mechanism is considered a secondary process on the basis of length scales for ions to "hop".[64,74] Ion transport in a perfluorosulfonated ionomer membrane has been proposed to proceed through ionic cluster in membranes implying that membranes with larger cluster regions have greater ionic transport. The size and number of ionic cluster regions is dependent on water content of membrane.[72] Permselectivity in conventional IEMs is governed by the affinity of an ion with the membrane, given by the ion exchange capacity and the mobility ratios of different ions within the membrane.

Cation Exchange Membranes

Cation exchange membranes (CEMs) are used in applications that require only cations to pass through the membrane. The negatively charged fixed groups in the membrane is usually either carboxylic acid based (COO^-), sulfuric acid based (SO_3^-), or phosphonic acid based (PO_3^-). Many different types of CEMs have been used in literature with different polymer backbones, such as perfluorinated copolymer (Nafion©), sulfonated polyvinyldifluoride (sPVDF), poly(ether-ether-ketone) (PEEK), sulfonated poly(ether-ether- ketone) (sPEEK), hydrocarbon (Fumatech).[75–77]

The fixed charge on cation exchange membranes (SO_3^- in Nafion©) is hydrophilic and self-organize into clusters when they absorb water from the environment. As a result, even for dense ion exchange membranes, there is an extended network of pores or channels filled with water in the membrane. Due to electrostatic attraction, cations are localized within a thin Debye layer next to the fixed charges in the pore, surrounded by electrically neutral solution.[78] Increasing water uptake reduces the selectivity of ion exchange membranes. One way to improve selectivity and decrease water uptake of the membranes would be by incorporating inorganic particles within the pores.[79,80] In some cases, incorporation of these particles can also lead to an increase in water uptake and consequently its ionic conductivity due to an incorporation of the nanoparticles, however, in many cases the ionic conductivity increases even though the water uptake decreases.[78] Since dense ion exchange membranes have pores with a diameter measuring 5nm or less, the incorporated particles should be similar in size. Such hybrid membranes, consisting of both inorganic and organic components within the membrane are called mixed matrix membranes.

1.3.3. Mixed matrix membranes

Mixed matrix membranes (MMM) consist of a continuous polymeric phase embedded with nanoporous/ dense inorganic materials, such as zeolites, Si, carbon nanoparticles (or nanotubes) etc.[81] The constituent material and their composition affect the separation efficiency of the membranes. Molecular separation primarily occurs according to solution-diffusion mechanism, however in the presence of microporous fillers, the mechanism is a combination of solution diffusion with surface diffusion or molecular sieving through inorganic phase.

MMMs with carbon molecular sieves combine the high separation capacity of carbon molecular sieves with durability and mechanical properties of polymers, while nanoparticles in MMMs affect the local chain packing, (and the local free volume) and the transport of permeating species. An

increase in free volume would increase molecular diffusion and reduce the sieving nature, thereby increasing permeability and reducing selectivity.[82]

Facilitated transport

Facilitated transport provides a possible mechanism for transport of selective molecules across the membrane interface. It refers to the transport of solute across a membrane due to combination of solution-diffusion mechanism and a complexation reaction. Where the complexation reaction provides an additional transport mechanism for the solute and is similar to chemical absorption of solute on feed side and stripping on permeate side.[55,83]

Carrier mediated facilitated transport membranes designed for ionic selectivity introduce selective molecules called carriers or extractants, into the membrane matrix. These molecules are responsible for selectively binding with target molecules and transporting them across the membrane interface.[84,85] Solute diffusion through a membrane can primarily occur either by diffusion of uncomplexed species or by diffusion of carrier-solute complex. In the latter mechanism, the reaction should be reversible so as to release the solute on the permeate side. In this case, the rate of transport of solute through the membrane thus can either be diffusion controlled or reaction rate (adsorption- desorption) controlled.

The specificity of the facilitated transport lies in the combination of intermolecular interactions and bonds between the carrier molecule and the target ion/solute, such as electrostatic interactions, Van der Waal's forces, hydrogen bond interactions, hydrophobic interactions etc..[86] Based on the mobility of the carriers, facilitated transport membranes can be grouped into three categories:[86]

1. Mobile carrier membrane,

2. Semi-mobile carrier membrane,

3. Fixed-site carrier membrane
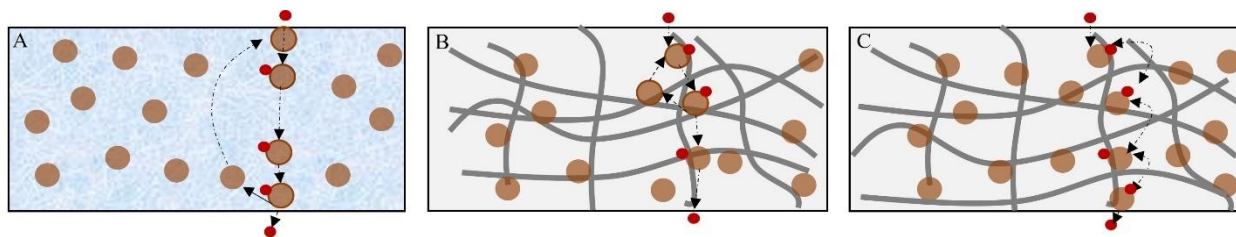
Figure 4: Illustration of solute transport in carrier mediated facilitated transport via (A) mobile carrier membrane, (B) semi-mobile carrier membrane, and (C) fixed-site carrier membrane.

Mobile carrier membranes allow the carrier to diffuse freely through it as seen in Figure 4A. The most common type of mobile carrier membranes are liquid membranes composed primarily of carried bearing solution matrix, e.g., ionic liquids. The target solute complexes with the carrier, and the mobile carrier-solute complex diffuses along the concentration gradient to the receiving side where the carrier is regenerated as the solute is released. The role of the carrier can be compared to that of a ferryboat wherein it serves to only transport the solute across the membrane, called "vehicle transport" mechanism. In fixed site membranes, the carrier position within the membrane is fixed and can only vibrate within a confined space. The transport of the solute occurs vis site-to-site "hopping" of the solute particles as seen in Figure 4C.[87] Carrier mobility in semi-mobile carrier membranes lies between mobile carrier and fixed site membranes. The carriers can diffuse, however, at a high diffusional activation energy cost. Both vehicle mechanism and hopping mechanism play a role in facilitated diffusion for semi-mobile carrier membranes (Figure 4B).

The choice of extractant/carrier is crucial to develop a facilitated transport membrane selective to the solute under consideration. For this reason, the bond energy of the solute-carrier for the reversible reaction should fall within a certain range to be effective. A weak bond energy would cause little solute transport, while high bond energy would lead to reaction reversibility issues.

The development of fixed carrier membranes was proposed as an alternative to the utilization of liquid membranes. The fixed carrier membrane can be an ion-exchange membrane in which the carrier is anchored to a counter-ion found in the polymer backbone, and it can also be a solid polymer electrolyte. In this latter case, the membrane is a solid solution of polymer and salt, in which the salt cations interact with the electrons on a heteroatom or functional group in the polymer backbone.[88] Besides this, the solute a can only be transported by the carrier if two sites are close enough, resulting in a minimum carrier concentration limit, below which no facilitated transport can take place.[87,89]

Currently, facilitated transport membranes are used for separation of gases, such as separation of olefins from an olefin/paraffin mixture, and for carbon dioxide removal from gas mixtures, oxygen enrichment from air, gasoline desulfurization, heavy metal ion extraction etc.[86,90,91] However, the need to develop membranes that allow for fast and selective permeation is critical for future developments. Facilitated transport theories help us understand the chemical microenvironment required within the membrane to promote high solute solubility, diffusivity, and selectivity, and play a crucial role in progressing membrane science towards the overarching goal.

An understanding of facilitated transport chemistries is crucial for rational design of facilitated transport membranes. Specifically for fixed-site carrier membranes, intermolecular forces of attraction between the carrier and solute or the carrier-solute reversible reaction chemistries are necessary to gain knowledge and develop new membranes.

1.4. Intermolecular Interactions

Chemical compounds and molecules are formed due to the attraction between two or more atoms. The two most common examples of bonds seen in nature are:

a. Ionic bonds

Ionic bonds are formed by the electrostatic attraction between two atoms of oppositely charged ions, and the strength of the bonds is dependent on the difference in electronegativity between the two atoms. All ionic bonds have some covalent characteristics.

b. Covalent bonds

Covalent bonds are formed by the sharing of valence electrons between atoms, in contrast to the transfer of electrons in ionic bonds. All covalently bonded molecules with unequal sharing of electrons, owing to higher electronegativity of one atom, form polar covalent bonds. In such atoms, there is a charge separation that draws the electron cloud towards the more electronegative atom and lends it a slightly negative charge. Although the molecule as a whole is electrically neutral,

$$H^{\delta+} \qquad H^{\delta+}$$

$$O^{\delta-}$$
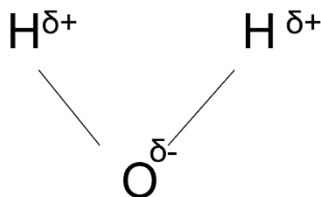
Figure 5: Dipole in a water molecule

the displacement of charges from the center forms a dipole. For example, a water molecule in figure 5 has a dipole moment arising from the electronegativity of the oxygen atom which draws the electron cloud towards it lending it slight negative charge and the hydrogen atoms a slight positive charge.

Intermolecular forces mediate interactions between molecules and are responsible for many macroscopic effects. These intermolecular attractions that bring molecules together, also called Van der Waals forces are composed of several intermolecular interactions that contribute to the energy of interaction and have the following types[92–94]:

a. Dipole-dipole interactions (Keesom forces)

Polar molecules have a permanent partial charge separation in addition to an instantaneous partial charge (London forces, explained below). This partial charge separation is called a dipole.[92–94] Keesom interaction forces arise from the dipole-dipole interaction between two permanent dipoles. The dipole-dipole (Keesom) interaction comes about from the fact that on the average, two freely rotating dipoles will align themselves so as to result in an attractive force, similar to that commonly observed with bar magnets.[95]

b. Dipole-induced dipole interaction (Debye forces)

A permanent dipole can generate an electric field which can induce a dipole in a nearby neutral atom.

c. Instantaneous dipole-induced dipole (London forces)

London forces refer to the attractive forces between two neutral atoms with no charge or permanent dipole. Non-polar molecules have only London forces acting between them. The electron cloud of atoms and molecules are like a swirling fog, and as they spin they produce an instantaneous dipole moment as the electrons pile up at one end and expose the other end. This charge separation leads to a partial positive charge on the exposed end, and a partial negative charge on the other end. These instantaneous dipoles attract one another and stick together.[94]

d. Hydrogen bonding

Hydrogen bonding exists between molecules when the H atom lies between two small and highly electronegative atoms containing a lone pair of electrons (specifically N, O, and F). Hydrogen bonding is the strongest intermolecular force.

Lewis Acid Base Theory

According to Lewis Acid Base theory, Lewis acids are molecules that are electron pair acceptors, while Lewis bases are electron pair donors.[92,93] Lewis acids and bases react to form a Lewis Acid Base complex via a coordinate covalent bond, where both electrons to form the covalent bond come from one species (the electron donor).

Coordination Compounds and Complex ions

A complex ion is formed when a transition metal ion bonds with a ligand, a molecule with a lone pair of electrons that can be donated, such as H_2O, NH_3 etc. A coordination compound is formed when complex ion formed by the transition metal ion bonds with a counter ion.[92]

The interaction between a metal ion and a ligand occurs through Lewis acid base reaction, where the ligand donates its electron pair to an empty orbital on the metal ion forming a coordinate covalent bond.

Complexation reaction chemistries

With this knowledge, we can now proceed to understand the chemistry of facilitated transport using surface coordination chemistry. Surface-ion interaction can occur through one of three ways: inner-sphere complexation, outer sphere complexation, and diffuse layer interaction. The inner- and outer-sphere interactions involve chemical bonding (at discrete sites for inner-sphere complexation), while the diffuse layer interaction is the non-specific electrostatic attractions.[96] An inner-sphere complex is essentially a covalent bond formed between the metal and the electron pair donating ion, while an outer-sphere interaction is the attractive force experienced by the participating species that are within a critical distance in addition to covalent bonding characteristics, finally, the ion may even exist in the vicinity of the surface in the diffuse swarm of the double layer (see Figure 6).[96]
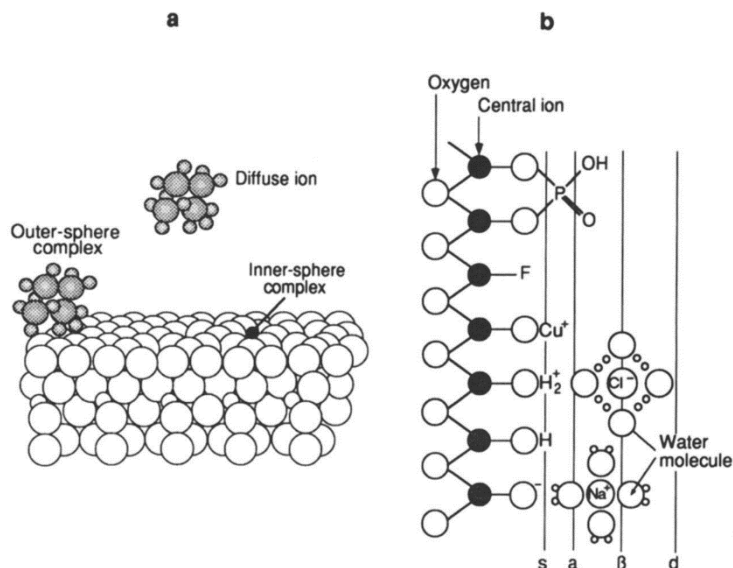
Figure 6: (a) Surface complexation types of an ion on a hydrous oxide surface. The ion may form a covalent bond with the surface (inner-sphere bond) or an ion pair (outer-sphere complex) or may exist within the electrical double layer. [Ref 96. Copyright 1995 (1984)][96] (b) Schematic portrayal of the hydrous oxide surface, showing planes associated with the surface hydroxyl groups (s), inner sphere complexes (a), outer sphere complexes (β), and the diffuse swarm (d). In the case of inner sphere complexes with ligand, the ligand replaces the surface hydroxyl group (ligand exchange). [Ref 96. Copyright 1995 (1984)][96]

Inner sphere complexes are formed when some ligands form coordination complexes with metal ions by replacing the functional groups (e.g., hydroxyl groups) in the first coordination sphere of the metal. Such complexes are specific, however, less than those observed in nature such as the enzyme-substrate complex.[96] Such surface complexation reactions can be equated to a specific-adsorption process.[97]

In surface chemistry, two reactants maybe either form a product that has lower energy than the two individual reactants, or experience attraction and bonding to form a reaction intermediate.[98] These labile compounds can be characterized by the absence of a strong bond between the central metal atom and the ligand, and are formed by bonding with the metal atom in the second coordination sphere of the metal complex, hence called outer sphere interactions.

Outer-sphere complexes are essentially formed between an inner sphere complex, with the coordination number of the central metal atom completely saturated, and ion species in the outer sphere, and is characterized by the absence of a new direct bond.[99] These complexes were initially characterized by ion pairing; however, further research revealed their differences: ion pairs result from coulombic attraction of partly or completely solvated ions, whereas outer-sphere complexes are formed by donor-acceptor interaction and show significant covalent bonding characteristics.[99] The nature of the bond is complex and includes donor-acceptor interaction which plays a major role in complexation, and electrostatic (/Van der Waal's) interactions which are less specific but do contribute to the complexation.

As a reaction intermediate, the outer-sphere complex has low thermodynamic stability and low activation energy (of ligand replacement processes). This facilitates implementation of outer-sphere interactions under dynamic conditions, for instance in electroactive materials, ion exchange, or chromatographic systems requiring repeated sorption-desorption processes. The selectivity of the outer-sphere complexes, although lower selective than inner-sphere complexes, is highly dependent on the nature of the metal ion and the ligand species.[99]

1.5. Carbon Nanotubes

Carbon nanotubes are (CNTs) are 3 dimensional tubes of sp^2 hybridized carbon that resembles graphene sheets rolled seamlessly. There two types of CNTs: single walled (SWNT) and multiwalled (MWNT) carbon nanotubes as shown in Figure 7.[100] Carbon nanotubes are superior 1D conductors and display several interesting mesoscopic phenomena, such as single-electron charging, resonant tunnelling etc., at low temperatures.[101] Owing to their high thermal and electrical conductivity, high specific area, hydrophobicity, mechanical strength, chemical

inertness, and water transport properties CNTs have found a niche application in membrane modification for water treatment.[44,52,102–107]

CNTs also exhibit excellent adsorption, catalytic, and electrochemical properties which enables coupling adsorption, catalytic, or electrochemical operations with membrane separation process, improving water treatment performances of CNTs-based membranes.[107]
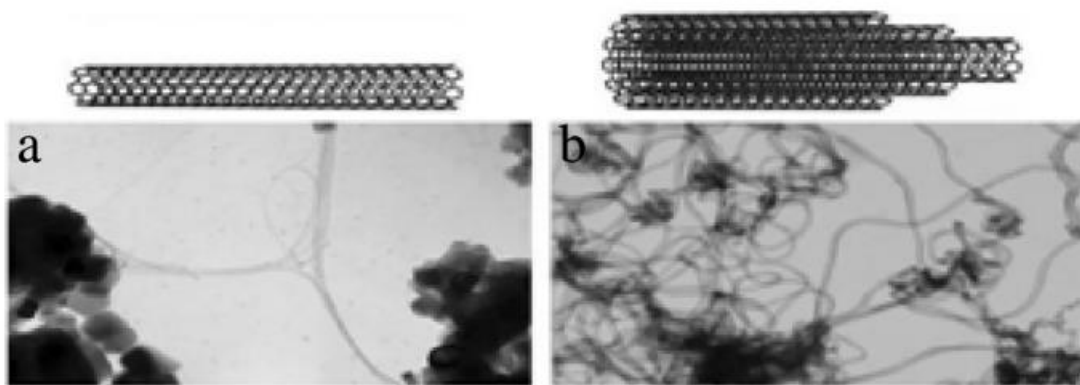
Figure 7: Schematic representation of (a) single walled carbon nanotube (SWNT) and (b) multiwalled carbon nanotube, with typical TEM micrographs. (Adapted from "Different Technical Applications of Carbon Nanotubes" published in Nanoscale Research Letters in 2015)[108]

1.5.1. CNT-based membrane electrodes

Conventional membrane-based processes, such as microfiltration, ultrafiltration, reverse osmosis, membrane distillation etc., are plagued with problems such as fouling and scaling, and inefficient rejection of dissolved solutes, uncharged solutes, or other emerging contaminants.[109] More importantly, these membranes can be altered to serve additional applications, for example, electroactive membranes. Electroactive membranes are a revolutionary technology that integrate electrochemistry with membrane separation with an enhanced mass transport by convection.[109]

Membranes with higher electrical conductivities have been prepared using conductive polymers and inorganic materials such as sub-stoichiometric TiO_2, however, they face problems such as brittleness, low flux, and poor separation performance.

Carbon nanotubes (CNT) have proven to form thin conductive films of functionalized multiwall CNTs over membrane surfaces that increase conductivity, with surface conductivities of ~1000-2000 S/m (metals have conductivities $>10^5$ while insulators have conductivities $< 10^{-6}$ S/m)[110], without compromising on membrane properties.[111] Such electroactive can enable electrical and thermal conduction and its distribution across the network of nanotubes.[109,112] This imparts the membrane with additional properties and can enable new interactions at the membrane-water interface, such as, surface reactions that cause oxidation or reduction of certain chemical compounds present in water[44,52,113], promote physical adsorption onto its surface, improve anti-fouling and anti-scaling ability of membrane can repel like-charged foulants by electrostatic repulsion to prevent fouling and scaling on membrane surface[105,114], and impart heat to the surrounding liquid via joule heating of CNTs.[109,115]

CNT based hydrophobic membranes have been produced by a number of ways including phase inversion, vacuum filtration, chemical grafting, electroplating, and spray coating. Of these methods, spray coating has emerged as the most environmentally friendly, versatile, and inexpensive method.[106] In literature we see two types of CNT membranes; one where the CNT powder is arranged over the membrane in a disorderly fashion or blended into the polymeric matrix to form a dense layer that allows for fluid transport through the gaps in the arrangement, and another where the CNT is vertically aligned in a well-ordered fashion and the internal pores of CNT form the fluid channels.[109] CNT based membranes can also be divided into two categories based on the application; currently, CNT is either deposited onto a hydrophilic polymer membrane support for pressure driven processes, such as reverse osmosis (RO), or onto a hydrophobic polymer membrane and then crosslinked with a hydrophilic or hydrophobic polymer for thermal

desalination, such as membrane distillation (MD).[110] In both these cases, the CNT is deposited in a disordered and non-aligned way as a thin layer that forms a percolating network (figure 8).
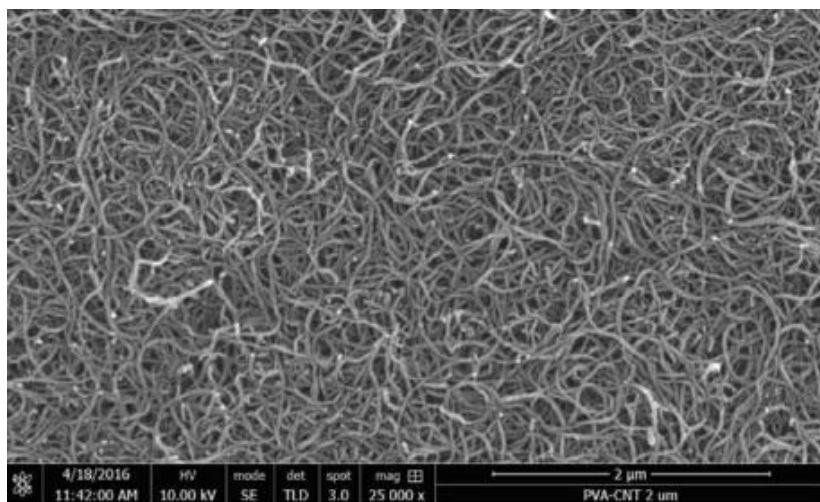
Figure 8: Surface morphology of a CNT- coated polysulfone ultrafiltration membrane with individual non-aligned CNT arranged.[113]

One of the biggest advantages of CNT-coated electroactive membranes is the role they play in mediating interfacial reactions. An application of surface potential transforms the membrane to a membrane electrode facilitating surface reactions such as water splitting, hydrogen evolution, oxygen evolution etc. In case of pressure driven processes, where water containing contaminants is forced through the membrane pores, the diffusion pathway between the contaminant and the electrode is reduced increasing mass transfer rates, and enhancing electrochemical reactions, such as direct electrooxidation/reduction and indirect electrooxidation (e.g., by OH·).[110]

While several studies have demonstrated the advantages of CNT based electroactive membranes, the technology still faces several challenges. For CNT or any other conductive phase deposited onto a non-conductive phase, there exists a threshold concentration called percolation threshold, at which electrical current can flow through the matrix via interconnected particles.[116] Current flows through a CNT network and faces resistance either (i) through intrinsic resistance of the

CNT, and (ii) resistance resulting from electron tunnelling effect at CNT-CNT junction. Studies modelling the role of tunnelling resistance in CNT networks have attributed that tunnelling resistance is the dominant factor contributing to the electrical conductivity of the network.[110,116,117] Therefore, one of the biggest challenges faced in using CNT coated electroactive membranes is the uneven current distribution through the CNT network.

Several studies have looked at improving conductivity of CNT films, such as by electropolymerization of polyaniline over the CNT network[104], enhancing conductivity of CNT based thin films (for electronic applications)[118], or depositing a layer of metal such as Nickel.[44,52]

1.6. Research Objective

The overall objective of this research was to develop novel membranes that promote specific interfacial interactions for precision recovery of ions/solutes from wastewater.

In chapter 2, an electrically conducting hydrophobic membrane to recover nitrogen as ammonia from wastewater was developed. The objective of this research was to study the dependence of ammonia recovery on membrane conductivity and pore morphology. For this, we developed three types of membranes, one with CNT coated onto a hydrophobic polymeric membrane, and two others with an additional metal layer composed of Ni and its (hydro)oxides, on top of the CNT layer, to improve the membrane's electrical conductivity. The two Ni based membranes differed in the quantity and composition of Ni present on the surface, varied by varying its electrodeposition time. The three membranes were characterized via scanning electron microscopy, atomic force microscopy, gas permeability, contact angle measurement, and cyclic voltammetry study. Ammonia recovery in the membranes was studied by circulating an acid solution on the receiving side of the membrane to convert the escaping ammonia to pure ammonium sulfate. The best

28

performing membrane was then used to recover ammonia directly from wastewater by applying a negative pressure on the receiving side of the membrane.

In chapter 3, a novel membrane that allows for highly selective phosphate transport (an anion) through a cation exchange membrane (CEM) was developed. The objective of this study was to investigate the possibility of phosphate recovery as phosphate ion (PO_4^{3-}), as opposed to a precipitated mixed salt (e.g., struvite, $NH_4MgPO_4.H_2O$). This was achieved by developing a facilitated transport membrane by embedding the cation exchange material with nanoparticles capable of binding selectively with phosphate. Membrane performance was evaluated using flux and permeability measurements, and selectivity experiments in the presence of competing anions. The novel membrane was designed to utilize outer-sphere interaction between the phosphate ion and the embedded nanoparticle to provide an innovative pathway for phosphate transport (hopping along adjacent nanoparticles). Molecular dynamics simulations were performed to confirm the hypothesis; and finally, a mathematical model was developed to predict nanoparticle loading required to improve ion transport flux, comparable to that of commercial membranes.

In chapter 4, conclusions from the doctoral research are summarized and a discussion on the impact of these membranes on current and future research is provided. The chapter also highlights drawbacks and avenues for future research directions.

Chapter 2:

Efficient Ammonia Recovery from Wastewater using Electrically Conducting Gas Stripping Membranes

Arpita Iddya, Dianxun Hou, Chia Miang Khor, Zhiyong Ren, Jefferson Tester, Roy Posmanik, Amit Gross, and David Jassby

Abstract

Recovery of nutrients, such as ammonia, from wastewater offers an attractive approach to increase the overall sustainability of waste management practices. Conventional wastewater treatment processes require significant energy input, and the useful form of nitrogen (ammonia), is usually lost. Ammonia, a major component of fertilizers, is convetionanlly manufactured using the Haber-Bosch process, which accounts for approximately 2% of worldwide energy demand. A better approach would efficiently capture ammonia directly from the wastewater. In this study, ammonia is recovered directly by using an electrically conducting gas-stripping membrane that is immersed into a wastewater reactor. Under cathodic potentials, these membranes were used to facilitate conversion of ammonium (NH_4^+) into ammonia (NH_3), which was then extracted by either circulating an acid solution or by applying a vacuum on the back side of the membrane. The mechanism involves water electrolysis, which generates OH^-, and transforms ammonium to ammonia that is stripped through the membrane. By engineering the surface and transport properties of the membrane 68.8 ± 8.0 g-N/m^2/d of ammonia was recovered, with an energy consumption of 7.1 ± 1.1 kWh/kg-N.

2.2. 2.1. Introduction

Increasing interest in process sustainability and a growing water and resource scarcity are driving the need for recovery of valuable resources from wastewater streams.[20–22,119] Wastewater is a potentially attractive source of clean water and nutrients.[120] High-strength wastewater streams contain large amounts of organic matter and nutrients, such as nitrogen (N) and phosphorus (P), that are essential for the growth and development of organisms, and can, if released in excess, lead to eutrophication in receiving water bodies.[28] Therefore, the removal and recovery of nutrients from wastewater streams serves a dual purpose, both eliminating a eutrophication source while simultaneously providing a source of fertilizer and/or energy.[121,122] In particular, nutrient recovery is attractive (compared to simple transformation of said nutrients to N_2 gas, e.g., through nitrification/denitrification) because it (i) provides a source of fertilizers, (ii) mitigates the environmental footprint of wastewater treatment processes, (iii) leads to decreased fossil fuel uses and associated emissions used for the production of synthetic fertilizers.[38] Thus, harvesting and using nutrients from wastewater can lead to potentially significant environmental, economic, and energy savings, increasing the overall sustainability of the wastewater treatment process. [30,35–37] The economic prospects of this process could be enhanced by implementing clean energy incentives, such as carbon credits.

Conventional water treatment relies on biological processes (nitrification, denitrification, or anammox) to remove N, contamination.[28,123]. There are two main drawbacks to this process. First, in raw wastewater, N is primarily found in its useful form, ammonium (NH_4^+). During the nitrification and denitrification process, ammonium is converted to N_2, which is lost to the environment. Nitrogen is then used in the energy- intensive Haber-Bosch process to generate ammonia (which is converted to ammonium when dissolved in water).   Largely as a result of

reforming natural gas to produce the required hydrogen for ammonia synthesis, the Haber-Bosch process accounts for approximately 2% of global primary energy consumption. [124,125] Second, the nitrification/denitrification process, which is a biological process with an initial aerobic phase (nitrification), requires significant energy investment, primarily in the form of aeration.[46] Moreover, N_2O, a potent greenhouse gas, is released during both processes.[119,126] Therefore, the current method of treating N contamination in waste streams requires energy to first convert ammonium to an inert form (N_2), which then requires further energy input to re-convert it back to ammonia. A better approach would allow the capture of this ammonium directly from the waste stream (ideally in pure form), which would eliminate the need for nitrification, as well as decrease the need to convert atmospheric N_2 to ammonia. Another important advantage to the direct capture of ammonium from wastewater involves the removal of organic contaminants. Currently, the dominant process for organic removal is the activated sludge process, which is energy intensive (due to its aerobic nature) and generates large amounts of biosolids.[127,128] Anaerobic treatment of wastewater is an attractive option due to its small energy footprint, its ability to generate energy (in the form of methane), and the small amount of biosolids generated.[129,130] However, the adoption of anaerobic treatment of ammonium-rich streams is hindered by anaerobic bacteria's low N-removal capacity.[131–133] Therefore, developing a N-removal method that is compatible with anaerobic processes could potentially transform wastewater treatment across multiple sectors.[132] Many studies have investigated ammonium removal and recovery from waste streams by non-biological methods, including reverse osmosis, air/vacuum stripping, zeolite adsorption, ion exchange, struvite precipitation, and electrodialysis.[134–140] However, these processes suffer from drawbacks, such as high energy and chemical inputs. For example, air and vacuum stripping, and struvite precipitation, require lime addition to increase alkalinity and/or elevated temperatures

[139,141–143]; reverse osmosis suffers from low selectivity, and ion exchange materials are expensive and can suffer from the presence of competing ions.[144–146]

In an aqueous solution, ammonia and ammonium are in a pH dependent equilibrium, according to the following equation[147]:

$$NH_4^+ + OH^- \leftrightarrow NH_3 + H_2O, \quad pK_a = 9.246 \hspace{2cm} \text{Equation 1}$$

Where ammonia dominates in aqueous alkaline media with pH>10.[45] While the solubility of ammonium is extraordinarily high in water (the solubility of NH_4Cl in water at 25 °C is 383 g/L), the solubility of ammonia is lower (k_H = 0.59 mol m^{-3} Pas^{-1}).[123,148,149] Therefore, shifting the solution pH towards more basic conditions will convert ammonium to ammonia, and enable the extraction of ammonia vapor.[123,124,134,148–152] This approach has been demonstrated through the addition of alkaline chemicals (e.g., NaOH), which increase the pH, and electrochemically modifying the solution pH through water electrolysis (the cathodic part of the electrolysis reaction).[123,124,134,147–151,153–156] The extraction of ammonia from an aqueous stream has been achieved by inducing a partial vapor pressure difference between two streams. For example, Hou et. al. and Tarpeh et. al. used a hydrophobic membrane separating an ammonia-rich feed solution from a highly acidic draw solution, which provided an ammonia sink.[126,154] Increasing the temperature of the ammonia-rich solution also enabled the extraction of ammonia through either a hydrophobic membrane or the reactor's head- space.[147,151,157] In particular, vacuum-based extraction of ammonia is an attractive method, as the resulting ammonia is in relatively pure form, which can be used for more desired applications (e.g., energy generation) than fertilizer.[134] However, the high solubility of ammonia necessitates high vacuum pressures to induce effective extraction.[134,147]

In this study, we fabricated a novel electrically conducting gas stripping electrode by coating a hydrophobic polymeric support membrane with a layer of nickel-functionalized carbon nanotubes (CNTs). The gas-stripping electrodes are used as cathodes in a half-cell that is separated from a simulated high-strength wastewater (the anolyte) by a cation exchange membrane (CEM); using this setup, ammonium from the wastewater migrates in response to an electric field across the CEM. Water electrolysis in the catholyte increases the local pH, which shifts the ammonium to ammonia that is subsequently extracted through the membrane. We provide extensive membrane characterization and demonstrate very high ammonia recovery. Driving force for the extraction is provided through either circulating an acidic solution on the backside of the membrane, or through a vacuum. We also discussed the impact of electrode surface and physical properties on system performance, as well as described the impact of the driving force on the energy intensity and efficiency of the process.

2.2. Materials and Methods

2.2.1. Materials and Chemicals

A commercial hydrophobic polytetrafluoroethylene (PTFE) membrane (0.22 µm, Sterlitech, Kent, WA) was used for this study. Multiwall CNTs (outer diameter: 13-18nm, length: 3-30 µm, purity >99%, and functional group content[124] of 7%) functionalized with carboxylic groups via plasma treatment were purchased from CheapTubes Inc. (Brattleboro, VT). Sodium dodecylbenzenesulfonate (DDBS, technical grade, Sigma Aldrich), nickel sulfate heptahydrate ($NiSO_4.7H_2O$, 98% Alfa Aesar), nickel chloride hexhydrate ($NiCl_2.6H_2O$, reagent grade, Sigma Aldrich), boric acid (H_3BO_3, ACS grade, Fisher), sulfuric acid (H_2SO_4, 96.5%, Fisher), dextrose (ACS grade, Fisher), ammonium sulfate (($NH_4)_2SO_4$, ACS grade, Fisher), ammonium bicarbonate (NH_4HCO_3, 99%, Acros Organics), potassium phosphate monobasic (KH_2PO_4, ACS grade,

Fisher), potassium sulfate (K_2SO_4, ACS grade, Fisher), magnesium sulfate heptahydrate ($MgSO_4.7H_2O$, ACS grade, Fisher), calcium sulfate dihydrate ($CaSO_4.2H_2O$, 98%, Acros Organics), and sodium chloride (NaCl, ACS grade, Fisher) were used as received.

2.2.2. Solution Preparation

The CNT spray coating solution was composed of 0.1 wt% CNT powder dispersed in DI water, stabilized using DDBS at a 1:10 (CNT: DDBS) ratio. The electrodeposition solution for Nickel deposition contained 150 mM $NiSO_4.7H_2O$, 25 mM $NiCl_2.6H_2O$, and 500 mM H_3BO_3 (at pH 2.00, adjusted using H_2SO_4).[126]

The synthetic wastewater (anolyte) was composed of 55.5 mM dextrose; 5.2 mM $(NH_4)_2SO_4$; 43 mM NH_4HCO_3; 4.7 mM KH_2PO_4; 8.51 mM K_2SO_4; 5.89 mM $MgSO_4.7H_2O$; 3.23 mM $CaSO_4.2H_2O$; 0.21 mM Na_2SO_4 in millipure water.[158] Chloride-containing salts were avoided in the anolyte to eliminate the possible formation of chlorine (through chloride oxidation on the anode) that can form chloramines and complicate the analysis of the fate of ammonium in the system; although not representative of many actual wastewater steams, the absence of chloride salts eliminated concerns about alternate pathways for ammonium transformation.[159] In wastewaters containing chlorides, chloramine formation may occur, which can reduce the amount of ammonia that can be recovered. The total electrical conductivity and pH of the feed were 7.51 dS/m, and 7.48 respectively. The catholyte was composed of 0.0705M NaCl and 0.0278M $(NH_4)_2SO_4$ (pH of 7.04) in deionized water.

2.2.3. Membrane Preparation and Characterization

The CNT-coated electrically conducting membrane (ECM) was prepared as previously described by Li et al.[160] In short, CNT powder was suspended in solution using a horn sonicator, followed by centrifugation at 11,000 rcf (Avanti J-E Centrifuge, Beckman Coulter; Brea, CA) in two 10 min

cycles to remove unsuspended particulates. The CNT suspension was spray-coated onto the PTFE membrane support to achieve a thickness of approximately 1 µm. The prepared membrane was washed overnight with deionized (DI) water to remove residual DDBS, and then dried in the oven at 90 ºC for 15 min.

To deposit Nickel onto the membrane, the membrane was taped onto a stainless steel (SS) mesh with a mesh opening size of 0.222" to provide better electrical contact and to minimize the voltage drop across the CNT surface. The membrane-mesh composite was immersed in the electroplating bath and connected to an external power source (Korad KA3005P DC power supply), with the membrane used as cathode and a Ni 200 plate used as anode. The deposition was carried out under constant current conditions (20.4 A/m^2) for 6h (6h-Ni) or 24h (24h-Ni). The prepared Ni coated ECMs were peeled off the SS mesh, rinsed with DI water to remove any Ni residue and dried in an oven at 90 ºC. The 6 and 24h ECMs had a nickel loading of 2.83 ± 0.08 mg/cm^2 and 15.71 ± 2.61 mg/cm^2, respectively.

The hydrophilicity of the ECM surfaces was determined by contact angle measurements (CA; model 250, Rame-hart; Succasunna, NJ). Surface morphology was imaged using scanning electron microscopy (SEM; ZEISS Supra 40VP SEM; Oberkochen, DE) and evaluated for surface roughness (as the root mean square roughness) using ScanAsyst-Air and probes (Camarillo, CA) by Atomic Force Microscopy (AFM; Bruker Dimension FastScan Scanning Probe Microscope; Billerica, MA). X-ray photoelectron spectroscopy (XPS; Kratos Axis Ultra DLD spectrometer equipped with a monochromatic Al Kα X-ray source) was used to characterize the elemental composition of the membrane surface. The permeance of the membrane was measured using a bubble flow meter. The sheet resistance and conductivity of the membrane were determined using a four-point probe (Veeco; Plainview, NY) and cyclic voltammetry (CV). CV was done using a

three-electrode electrochemical analyzer (Potentiostat; CH Instruments 6005E; Austin, TX). A potential range of -1.2 to 0 V vs Ag/AgCl was applied to the ECMs as the working electrode at a scan rate of 0.01 V/s. A platinum wire was used as the counter electrode and all three electrodes were immersed in synthetic feed solution.

2.2.4. Experimental Setup

Experiments were conducted using a two-chamber cell with the chambers separated by a CEM (active membrane area 5.5 cm X 8 m, Fumasep FKE-50, Fuel Cell Store). A platinum coated titanium mesh placed 8 cm away from the CEM was used as an anode, while the ECM placed 5 cm away from the CEM and used as the cathode (Figure 9A-B).

Two experimental setups were used to provide the driving force for ammonia extraction. In the first setup, a 0.01M H_2SO_4 solution was circulated along the back-side of the membrane with a flow rate of 0.026 LPM (Figure 9A); this solution acts as an ammonia sink, providing a partial vapor pressure gradient that draws ammonia from the catholyte to the acid solution.[149,161] In the second setup, a vacuum pressure of -29 inHg (VE 225, 2 stage vacuum pump, 3.0 CFM) was continuously applied to the back of the membrane, which stripped dissolved ammonia through the membrane (Figure 9B). The vacuum stream carrying ammonia from the permeate chamber was directed into an acid trap containing 0.01M H_2SO_4 to convert ammonia into ammonium and prevent escape into the vacuum pump. The acid trap was followed by a water trap to capture any residual ammonia or acid vapors, followed by a desiccator to prevent water vapor from entering the vacuum pump. Each experiment was conducted as a batch experiment for a duration of 6h for each ECM as well as each experimental setup.

The ECM was housed in a custom-built flow cell (Figure 9C) with the membrane sandwiched between a frame and a bottom chamber. The ECM was placed such that the active surface (with

CNT and/or Ni) faces the solution and the permeate side faces the cell bottom. The frame exposes

an active area of the ECM (36 mm X 60 mm) directly to the solution, while the bottom part of the

flow cell acts as a permeate chamber to pass acid solution or apply vacuum. An aluminium shim,

cut to expose the active area of the membrane, was placed over the ECM to provide better electrical

contact and to connect the ECM to the potentiostat. The entire flow cell was immersed into the

cathode chamber (volume = 0.5L) along with the reference electrode while the anode was placed

in the anode chamber (volume = 1.5L).
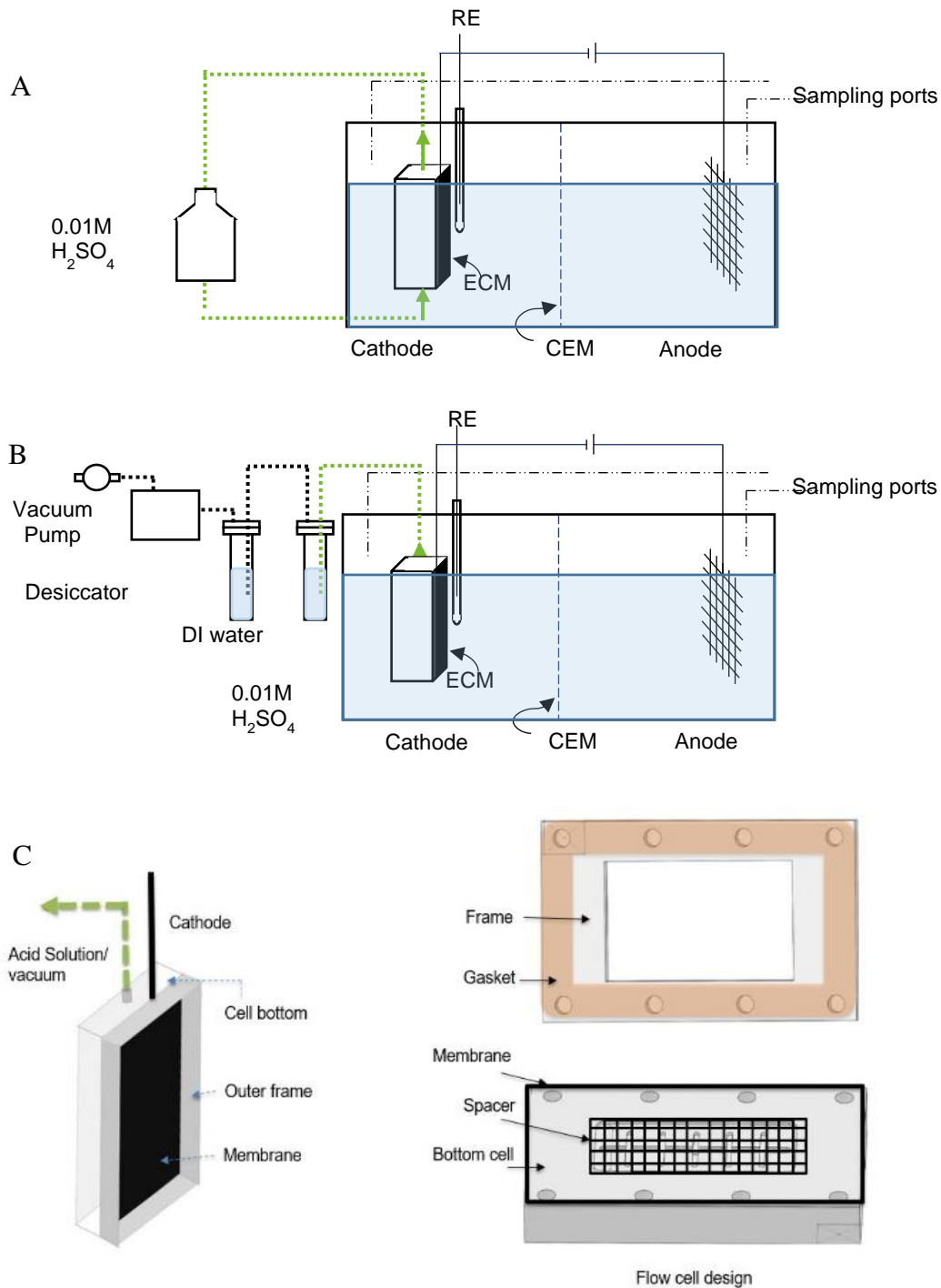
Figure 9: A) Schematic of experimental setup used for ammonia recovery by circulating acid solution (0.01M H_2SO_4) on the back-side of the Electrically Conducting Membrane (ECM). B) Schematic of experimental setup used for ammonia recovery by applying vacuum on the back-side of the ECM. The vacuum line was first passed through an acid scrubber to convert NH_3 back to NH_4^+. This was connected to a water trap to capture any escaping ammonia and/or acid vapour.

The water traps are connected to the vacuum pump through a desiccator to prevent possible water vapour in the air stream. The two chambers are separated by a Cation Exchange Membrane (CEM) C) Flow cell housing for recovering ammonia from solution.

2.2.5. Operating Conditions

Both anode and cathode compartments were continuously stirred using magnetic stirrers. In our experiments, three types of membranes were evaluated: CNT-only, 6h-Ni, and 24h-Ni. To induce electromigration of ammonium from the anolyte to the catholyte and promote water electrolysis on the ECM, a constant DC cathodic potential of 1.2 V vs. Ag/AgCl was applied to the membrane surface using a three-electrode potentiostat (CH Instruments 6005E, Austin, TX). The pH of the anolyte and catholyte was measured throughout the experiment using a pH probe. 10 mL samples were periodically collected from each of the three solutions (anolyte, catholyte, and acid stripping solution) and analyzed for NH_4^+ ion concentration using an ammonia ion selective electrode (Orion^{TM} High performance ammonia electrode, ThermoFisher; Waltham, MA). The presence of possible ammonium transformation products (e.g., nitrate, nitrite, chloramines) were evaluated by testing the samples for total nitrogen and nitrate concentrations using total nitrogen analysis (TOC/TN analyzer, Shimadzu; Kyoto, JP) and a spectrophotometer (HACH DR1900, Loveland, CO), respectively.

The ammonia removal rate, recovery rate, specific energy consumption and recovery were used to evaluate the process:

$$Ammonia\ removal\ rate = \frac{N_{T0} - N_{Tend}}{A_m * t} \hspace{4cm} \text{Equation 2}$$

$$Ammonia\ recovery\ rate = \frac{M_{end} - M_0}{A_m * t} \hspace{4cm} \text{Equation 3}$$

$$Specific\ energy\ consumption = \frac{(V * I * t)}{M_{end} - M_0} \hspace{3.5cm} \text{Equation 4}$$

$$Recovery = \frac{M_{end} - M_o}{N_{T0} - N_{Tend}} * 100 \hspace{3cm} \text{Equation 5}$$

where, N_{T0} and N_{Tend} are the total initial and final mass (in the anolyte and catholyte) of ammonia-nitrogen (NH₃-N) respectively, M_0 and M_{end} are the initial and final mass of NH₃-N in the acid solution, A_m is the area of the ECM, t is the duration of the experiment, V is the potential applied, and I is the current during the experiment. Here, removal rate is defined as the total amount of ammonia removed from the system (anolyte and catholyte), which includes the ammonia recovered across the ECM and the ammonia lost from the system (e.g., due to volatilization to the headspace), and recovery rate is the rate of ammonia transfer across the CEM.

2.3. Results & discussion

2.3.1. Membrane Characterization

The addition of a CNT coating to the surface of a hydrophobic PTFE membrane creates a black surface (Figure 10A); once the CNT network undergoes the Ni deposition step, the surface takes on a silvery sheen, indicative of the presence of a metal coating, with the longer Ni deposition time (24h) leading to a more complete-looking metal coverage (Figure 10B-C). Importantly, membranes undergoing nickel deposition for less than 6 hours showed incomplete metal coverage (not shown). Figures 10(D-F) shows the contact angle images of the three membranes. The CNT membrane is most hydrophobic with a contact angle of 146±8° (Figure 10D). Nickel deposition increases hydrophilicity of the membrane surface as seen by the contact angles for 6h-Ni (93±3°) and 24h-Ni (83±6°). Figures 10(G-I) show the membrane's surface as imaged by SEM. Prior to Ni deposition, CNTs are readily visible to form a uniform dense and porous network on the membrane surface with a pore size of about 0.1-0.2 μm (Figure 10G). Following a 6-h Ni deposition step, a rough-looking metallic cover can be seen to have grown on the CNT surface (Fig. 10H); the longer

Ni deposition time (24 h), led to a rougher looking surface cover (Fig. 2I). Cross-sectional images of the membranes obtained using SEM show the thickness of the layers to be 1.57±0.49 µm (CNT), 2.99±0.60 µm nickel after 6h of electrodeposition (6h-Ni), and 22.49±3.45 µm nickel after 24h of electrodeposition (24h-Ni) (Figure 10J-L). Thus, structure and depth of the Ni layer can be manipulated by varying the Ni deposition time. The root mean square roughness, characterized by AFM, of a 5µm x 5µm segment of CNT coated membrane was 133±2 nm (Figure 10M). The 6h Ni deposition process reduced surface roughness to 63.3±2.90 nm (Figure 10N), while the 24h Ni deposition yielded a surface roughness of 82.7±3.78 nm (Figure 10O).

The sheet resistance of the CNT coated membrane was determined to be 47.59 $\Omega/\square$, while for the nickel membranes the resistance declined to 5.91 $\Omega/\square$ (6h-Ni) and 0.01 $\Omega/\square$ (24h-Ni). Thus, introducing Ni on membrane surface dramatically decreased sheet resistance. Gas permeability measurements of the two nickel membranes revealed their permeance to be 48,000±7,743 barrer for the 6h-Ni and 18,000±5,443 barrer for 24h-Ni, which is 60-90% lower than traditional polymeric membranes[162,163], indicating that the addition of the Ni coating does indeed constrict the flow of gasses through the membrane, possibly due to pore constriction.

XPS was conducted to study the elemental composition of the membrane surface once Ni was deposited. Figure 11A shows the XPS spectra of the Ni($2p_{1/2}$) and Ni($2p_{3/2}$) bands and their satellites for the 6h-Ni and 24h-Ni membranes. The 24h-Ni membrane shows peaks at 852.7 eV and 856 eV, which correspond to Ni(0) and Ni(2+) as Ni(OH)$_2$, respectively. The 6h-Ni membrane shows a pronounced peak for Ni(2+) as Ni(OH)$_2$, and a weak peak for Ni(0).[164–167] It is possible that the smaller Ni(0) peak observed in the 6h-Ni sample is a result of extensive oxidation of the deposited Ni, a result of atmospheric exposure. In contrast, the thicker Ni cover obtained after 24h deposition may provide better oxidation protection, resulting in more abundant Ni(0).[126,168]
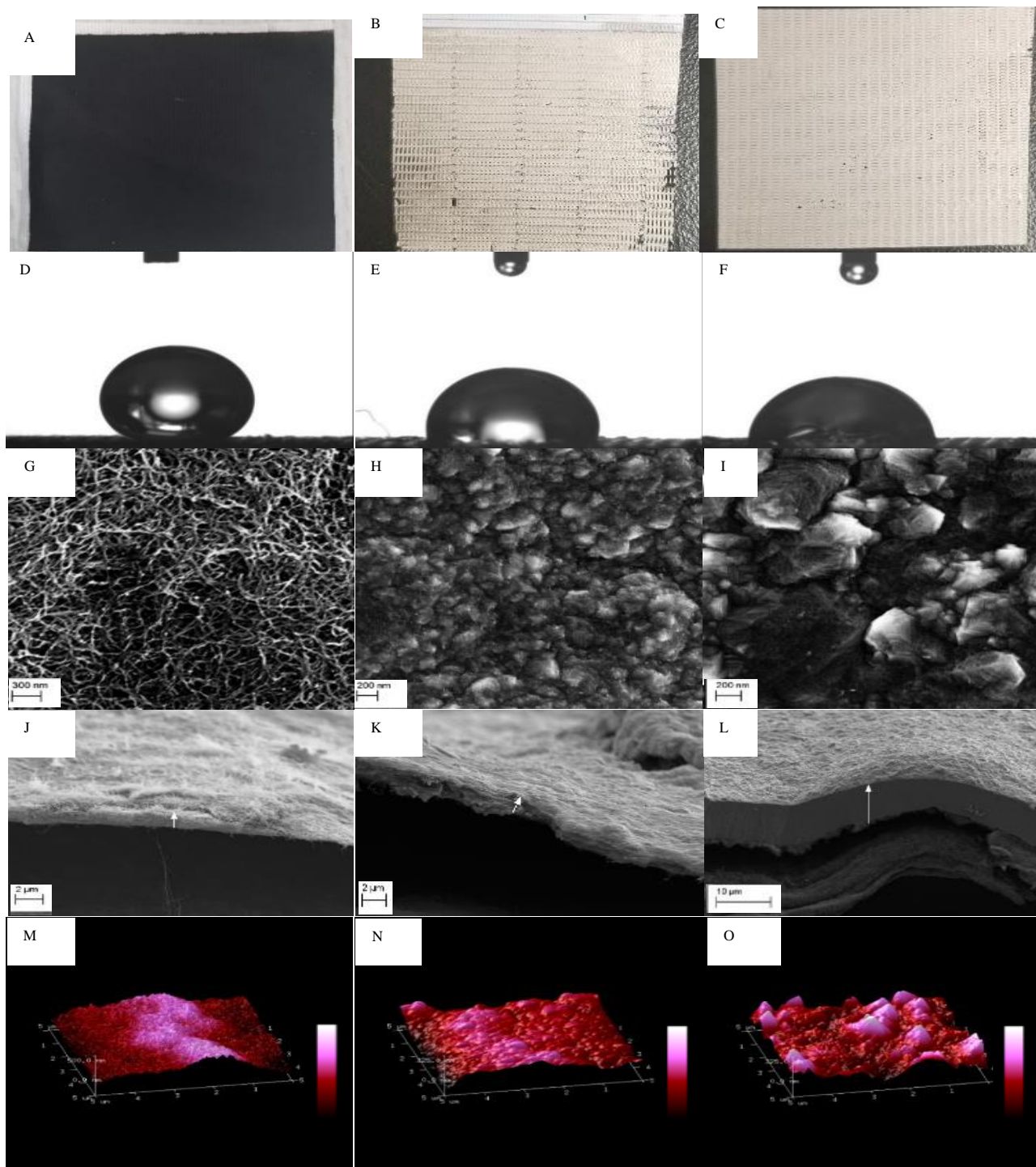
Figure 10: Photographs of A) CNT-coated ECM, B) ECM with Nickel deposited on CNT for 6h (6h-Ni), and C) ECM with Nickel deposited on CNT for 24h (24h-Ni); contact angle measurements of D) CNT- coated PTFE membrane, E) ECM with Nickel deposited on CNT for 6h (6h-Ni), and F) ECM with Nickel deposited on CNT for 24h (24h-Ni); SEM micrographs of G) CNT-coated PTFE membrane, H) ECM with Nickel deposited on CNT for 6h (6h-Ni), and I) ECM with Nickel deposited on CNT for 24h (24h-Ni); cross-sectional SEM micrographs of J) CNT-coated PTFE membrane, K) ECM with Nickel deposited on CNT for 6h (6h-Ni), and L) ECM with Nickel deposited on CNT for 24h (24h-Ni); AFM images of a 5µm x 5µm section of M) CNT-coated PTFE membrane, N) ECM with Nickel deposited on CNT for 6h (6h-Ni), and O) ECM with Nickel deposited on CNT for 24h (24h-Ni).
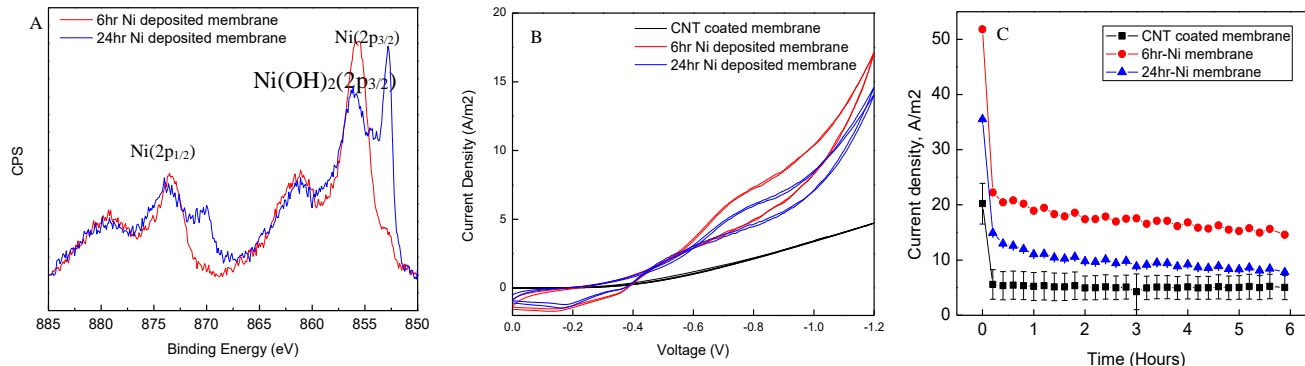
Figure 11: A) XPS spectra of 6h-Ni and 24h-Ni membranes showing Ni(0) and Ni(OH)2 2p peaks. B) CV curves of the three ECMs, obtained at a scan rate of 0.01 V/s. C) Time course change in current during the experiments.

The electrochemical properties of the membranes were characterized using current density versus voltage (CV) measurements (Figure 11B). Nickel is known to reduce the over-potential associated with the hydrogen evolution reaction (HER). [169–173]. To compare the activities of the different ECM materials, we measured the onset potential, defined as the potential at which the electron transfer process for a specific redox reaction begins, translated as an increase in current (Figure 11B).[174] For the HER, the onset of hydrogen evolution gives us insight into the catalytic activity of the surface under study.[175] The CNT ECM shows an onset potential of -0.4 V vs. Ag/AgCl. The 6h Ni and the 24h Ni ECMs have lower onset potentials of -0.24 and -0.2 V vs. Ag/AgCl, respectively. The current at -1.2V for the CNT ECM was 4.7 A/m^2, while for 6h and 24h Ni ECMs the current at -1.2 V was 17 and 14.5 A/m^2 respectively. The higher current at 1.2V for the 6h Ni ECM could be associated to its surface structure. The 6h Ni ECM surface has many small peaks and is more porous as compared to the 24h Ni ECM (which has fewer, more pronounced peaks). Many studies have shown that the edges of Ni(OH)$_2$ promotes water dissociation. Thus, the surface morphology of the 6h Ni ECM could be responsible for the higher observed current and more efficient HER.[164]

2.3.2. Ammonia Recovery Using Acid Stripping Solution

When the 0.01 M H_2SO_4 solution was used as the driving force for ammonia transport across the ECM, the ammonia removal and recovery rate were highest for the 6h Ni ECM, with a removal of 109 ± 21.55 g-N/m^2/d and recovery of 68.8 ± 8.02 g-N/m^2/d. The 24h Ni ECMs exhibited a removal of 99.5 ± 55.15 g-N/m^2/d and recovery of 20.5 ± 3.68 g-N/m^2/d. The CNT coated ECMs showed ammonia removal of 30.3 ± 6.32 g-N/m^2/d and ammonia recovery of 20.7 ± 8.15 g-N/m^2/d. In all cases, a cathodic potential of 1.2 V vs. Ag/AgCl was applied to the ECM. The current in the experiment decreased with time for each ECM (Figure 11C). The current decline could be attributed to the increase in cathodic overpotential as the pH in the catholyte increases with time due to accumulation of OH^-.[126]

Ammonia removal and recovery can be explained by looking at the mechanism for ammonia transport and removal. Ammonia recovery in the system occurs in three steps[134]:

i. NH_4^+ transport from anode to cathode across the CEM.

ii.   Transformation of NH_4^+ to dissolved NH_3 in catholyte (eq. 1).

iii. NH_3 transport from the catholyte into the permeate chamber across the ECM.

Transport across CEM The application of a potential produces a current that leads to electromigration of ions toward the oppositely charged electrode.[176] Effective recovery of NH_3-N depends on the efficiency of its transport across the CEM from the anolyte to catholyte. The efficiency of NH_3-N transport across the CEM depends upon current density, total ammonia nitrogen (TAN) loading rate, pH and continuous removal of ammonia from the catholyte chamber. Since migration of the ions is current driven, it is important to consider the ratio between current

density and TAN loading, termed the load ratio. Load ratio is the ratio of the applied current density to the theoretical amount of charge transported across the CEM as NH_4^+ (eq. 6):[156]

$$L_N = \frac{j_{applied}}{C_{A0}*Q_A*\frac{F}{A_{CEM}}}$$
<div align="right">Equation 6</div>

Where, $j_{applied}$ is the applied current density (A/m^2), C_{A0} is the initial molar concentration of the anode (mol/m^3), F is the Faraday constant (96.485 C/mol), A_{CEM} is the surface area of the CEM (0.004 m^2), and Q_A is the anolyte inflow rate (m^3/s). For our batch system, Q_A is calculated as the volume of anolyte (m^3) divided by the duration of the experiment (s). The significance of the load ratio is understood by looking at its absolute value: L_N <1, implies more N is fed to the system (i.e., a low current that cannot remove ammonia), whereas L_N>1, implies that the produced current is sufficiently high to induce NH_4^+ transport.

In our system, L_N was calculated to be in the range of 0.1 (CNT)- 0.3 (6h-Ni & 24h-Ni), implying that ammonia transport across the CEM is limited by electrical current.[156,177] This low L_N value suggests that higher current densities may increase the transport of ammonium across the CEM, which would increase ammonium removal.

Mass transport across the CEM results in a decrease in mass of NH_3-N in the anode chamber and an increase in the cathode chamber (Figure 12A& B). In the anode chamber, the mass of NH_3-N decreases from 942.58 $\pm$ 29.27 mg to 811.08 $\pm$ 39.44 mg when the CNT ECM was used as the cathode. For Nickel ECMs, the mass of NH_3-N decreased from 1034.52 $\pm$ 24.95 mg to 856.55 $\pm$ 29.47 mg for 6h-Ni, and from 1050.67 $\pm$ 32.12 mg to 868.01 $\pm$ 35.65 mg for the 24h-Ni materials. Ammonia flux across the ECM can be seen in Figure 13. Due to low the low current in the CNT ECM setup, the NH_3-N transport rate across the CEM was also the lowest (111.76 $\pm$36.87 g-N/m^2/day), while for the nickel membranes the transport was similar (177.96 $\pm$13.77 g-N/m^2/day

for 6h-Ni and 182.66 ±20.50 g-N/m^2/day for 24h-Ni membrane). The decrease in NH$_3$-N concentrations in the anode chamber is accompanied by a corresponding increase in the NH$_3$-N concentrations in the cathode chamber. For CNT ECMs, the mass of NH$_3$-N increased from 500.70
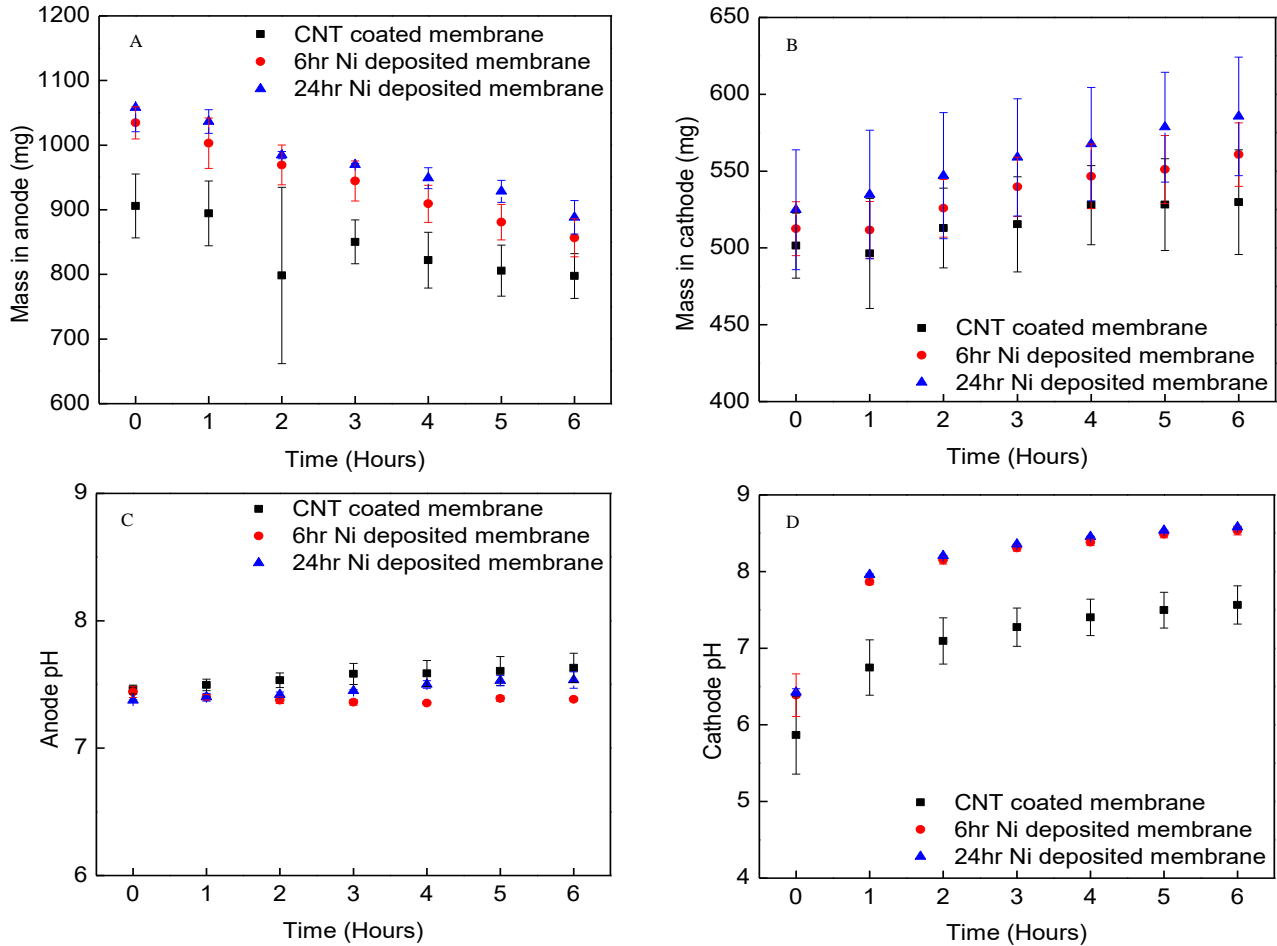
Figure 12: Change of mass of NH$_3$-N over time in the a) anolyte and b) catholyte chambers. And pH change over time in the c) anolyte and d) catholyte chambers.

±22.14 to 529.77 ± 34.10 mg, while for 6h-Ni membrane, the mass of NH$_3$-N increased from 512.54 ± 17.55 to 560.75 ± 20.73 mg, and from 512.14 ± 36.60 to 567.63 ± 40.47 mg for 24h-Ni ECMs. The decrease and corresponding increase in mass of NH$_3$-N, in the anolyte and catholyte is due to migration of ions under the applied electric field across the CEM, the conversion of ammonium to ammonia, and its subsequent extraction from the catholyte limits the back diffusion of ammonia, as well as tempers the increase of ammonium in the cathode chamber.
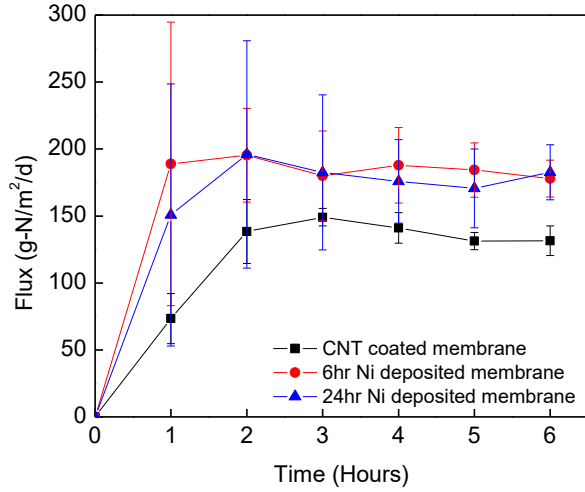
Figure 13: Variation of flux of NH_3-N with time. The flux, normalized to the ECM surface area, decreases as the current decreases and ECM fouls over time.

Conversion of ammonium to ammonia In addition to providing a driving force for ion transfer, the current also helps in splitting water to effectively modify the pH in both chambers. On the ECM cathode, the following reaction takes place[178]:

$$H_2O + e^- \rightarrow \frac{1}{2}H_2 + OH^- \qquad\qquad \text{Equation 7}$$

Assuming the applied current only triggers water electrolysis, pH along the surface can be calculated as a function of the applied current density (j), and the diffusion of H^+ and OH^- within the diffusion boundary layer (where ion convection can be neglected) as given by (eq. 8)[179,180]:

$$j = \frac{F}{\delta}\left[D_{H^+}(c_{H^+}^s - c_{H^+}^b) - D_{OH^-}K_w\left(\frac{1}{c_{H^+}^s} - \frac{1}{c_{H^+}^b}\right)\right] \qquad\qquad \text{Equation 8}$$

Where, F is the Faraday's constant, δ is the boundary layer thickness, D_i is the diffusion coefficient and c_i the concentration of species i and K_w the ionic product of water. Eq. 8 can be used to calculate the pH along the cathode surface at the applied current density. For current densities of

~17A/m^2, the pH along the cathode at a distance of *30 μm* from the surface was calculated to be approximately ~13.8, considerably higher than the pKa of ammonium (eq. 1) required to shift the equilibrium toward producing ammonia.

Figures 12C and 12D show the pH trend in the anolyte and catholyte. The pH in the anode chamber varies between 7.38 ± 0.04 − 7.6 ±0.2 over 6 h for all three membranes. It is likely that the carbonate ions in the anolyte act as a buffer to help maintain the anode pH.[39,176] The pH of the catholyte increased from 5.9 ± 0.47 to 7.75 ± 0.35 for CNT ECM, while for 6h Ni and 24h Ni ECMs the pH increases from 6.42 ± 0.3 to 8.5 ± 0.05. For all three ECMs, pH in the catholyte increases linearly in the first few time steps and then plateaus as production of OH$^-$ is countered by conversion of NH_4^+ to NH_3.[126]

Transport and recovery of ammonia In this study, ammonium transport across the ECM represents NH_3-N recovery. Although transport across the CEM is current limited, the mass transport of NH_3-N across the CEM is higher than that across the ECM, leading to the accumulation of ammonium in the catholyte. Of course, the accumulation of ammonium in the catholyte is strongly dependent on the membrane area (both the CEM and ECM), with larger ECM areas enabling larger mass removal.

Figure 14 also compares the overall NH_3-N removal rate (i.e., NH_3-N removed from the anolyte) with the NH_3-N recovery rate (i.e., NH_3-N that passed through the ECM and accumulated in the acid solutions). CNT and 6h Ni ECMs show the highest percentage of NH_3-N recovery (% of ammonia recovered in acid solution over total ammonia removed from the catholyte), ~65 %, while the percent of NH_3-N recovered is ~21% for 24h Ni ECM. However, the NH_3-N recovery rate was the highest for the 6h Ni ECM (68.86 ±8.02 g-N/m2/day), while it was similar for 24h Ni and CNT ECM (20.51 ±3.69 g-N/m^2/d and 26.06 ±0.87 g-N/m^2/d, respectively). Lower recovery by 24h Ni

ECM could be attributed to its lower gas permeability, a result of the longer nickel deposition time that increased pore blocking. The recovery rate measured in our experiments was higher than that of reported in other studies utilizing an electrical current to facilitate the conversion of ammonium to ammonia gas. For example, Hou et. al. reported a recovery rate of 36.2 g-N/m^2/d for a Nickel membrane electrode, while Zhang et. al. recovered ammonia using a carbon slurry in a capacitive desalination unit, with a reported recovery rate of 19.5 g-N/m^2/d at a current density of 17.2 A/m^2.[126,181]
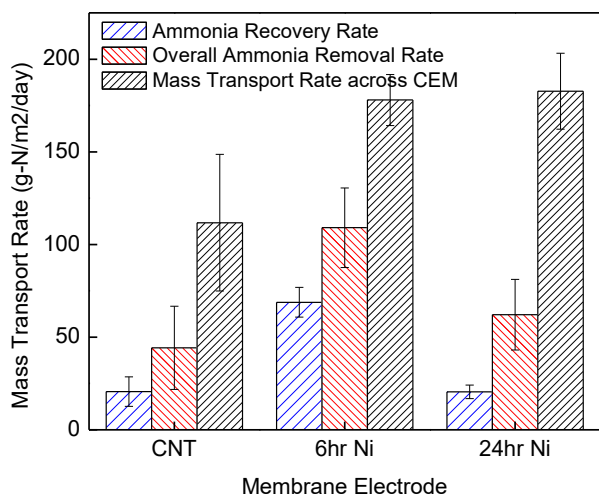
Figure 14: Comparing nitrogen flux across the CEM with overall ammonia removal and recovery rate for each ECM.

A mass balance on NH$_3$-N shows a significant amount of unaccounted ammonia. As discussed above, of the total amount of ammonia removed, between 35–79% is unaccounted for. We speculate that the unaccounted ammonia volatilized and is either present in the headspace or escaped from the acid stripping solution. The ammonia loss was also measured by checking for nitrate/nitrite formation. Measurement revealed no nitrate or nitrite formation in either solution (anolyte or cathoyte). Moreover, total nitrogen concentration matched the concentration of NH$_3$-

N leading us to conclude that ammonia in the catholyte was either recovered as ammonium sulfate (i.e, passed through the ECM), volatilized, or remained in solution.[181]

2.3.3. Vacuum extraction of ammonia

For recovering ammonia with vacuum as the driving force, 6h Ni ECM was used for its improved performance compared to the other membranes. Figure 15 shows an NH_3-N removal rate of ~62 ±15.30 g-N/m^2/d, and a recovery of ~17.56 ±5.60 g-N/m^2/d. Similar to the acid circulation experiments, the mass transport of NH_3-N across the CEM was much higher than the mass transport across the ECM, demonstrating the importance of the ECM area.

Gas transfer across a highly porous membrane occurs mainly by Knudsen diffusion, and as a result, the permeability of the transporting species depends on the geometry and structure of the membrane, and on the molecular weight of the permeating species.[147,182] Most notably, the mass flux across the membrane is directly proportional to the pressure difference across the membrane.[183]

Flux of ammonia, J, through the ECM under an applied vacuum can be described by (eq. 9): [134,183,184]

$$J = \alpha * (P_{fNH_3} - P_v Y_{vNH_3}) \quad [mol/m^2/s]$$ Equation 9

Where, α is the membrane permeability coefficient, P_{fNH_3} is the partial pressure of ammonia on the feed side, P_v, the vacuum pressure on the permeate side, and Y_{vNH_3} the mole fraction in vapor phase on the vacuum side. The partial pressure of ammonia at the feed side, P_{fNH_3}, can be calculated using Henry's law as (Equation 10)[134]:

$$P_{fNH_3} = \frac{100 * \gamma * m_{NH_3}}{K_H} \quad [kPa]$$ Equation 10

Where, m_{NH_3} is the molality of ammonia in the feed, γ is the activity coefficient, and K_H the Henry's constant for ammonia. Assuming an activity coefficient of 1 and a Henry's constant of 55.96 mol/(Kg atm) at 25ºC, the partial pressure of ammonia on the feed side is calculated to be 0.0271 in Hg. Therefore, mass transfer of ammonia under vacuum is inhibited by its high Henry's constant, which is responsible for the low partial pressure.[123,148,154,185] This effect is enhanced due to the external applied potential that causes other cations in solution to compete with NH_4^+ ion migration to the cathode (ECM) surface.[186] Ammonia transfer is also affected by flux of water vapor and hydrogen gas across the ECM.[126,134,149,187]

The overall NH₃-N removal rate for the vacuum experiments is considerably lower than that measured using the circulating acid solution. The disparity in the recovery and removal rates for vacuum and acid circulation can be attributed to the higher driving force for systems using acid solutions, which provide an essentially infinite sink for ammonia transfer. Figure 15 shows that at the applied vacuum, 30% of the NH₃-N is recovered compared to the 63% recovery for
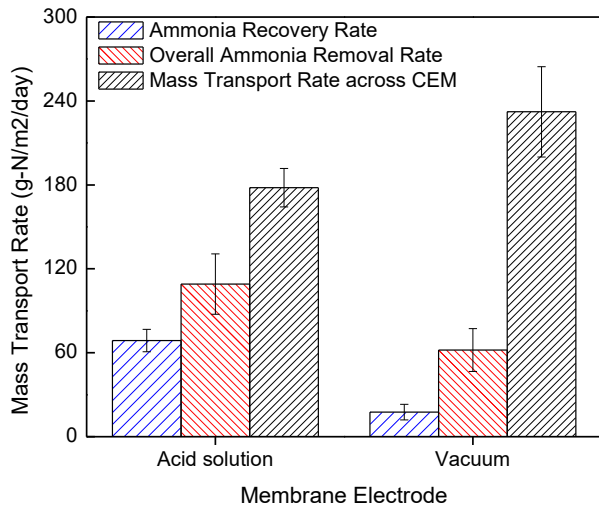
Figure 15: Comparing mass transport rates for 6h-Ni membrane for the two experimental setups to extract ammonia, circulating acid solution and vacuum.

experiments with circulating acid solution. NH_3-N recovery could therefore be improved by applying a higher vacuum, provided the ECM does not wet under the applied pressure.

2.4. Conclusions

The energy consumption for the ECMs was ~40% lower than conventional nitrogen removal processes such as the nitrification-denitrification process (12.5 kWh/Kg-N).[188] Although this energy consumption is higher than that associated with the Annamox process (4.4-5.3 kWh/Kg-N), the current process benefits as it recovers nitrogen as ammonia, a valuable commodity.[177,188] The specific energy demand based on ammonia recovered in the stripping solution was 7.0±2.40 kWh/kg NH_3-N for the CNT coated membrane, and 7.06±1.06 kWh/kg NH_3-N for the 6h Ni membrane. However, for the 24h Ni membrane, due to its low ammonium recovery, the specific energy demand was significantly higher (20.45±6.25 kWh/kgNH$_3$-N). Energy consumption of the process can be further lowered if the unaccounted ammonia, likely present in the headspace, is also recovered. Based on total ammonia removal (ammonia recovered using stripping solution and the missing ammonia that is likely volatilized), the energy consumption of the process is reduced by 35–74%, to 3.66±0.94 kWh/kg NH_3-N for the CNT coated membrane, 4.53±0.77 kWh/kg NH_3-N for the 6h Ni membrane, and 5.28±2.64 kWh/kg NH_3-N for the 24h Ni membrane.

For NH_3-N recovery via vacuum, the specific energy requirement based on NH_3-N removed was 11.68±2.8 kWh/Kg-N, which is 22.3% lower than the amount of energy required to produce ammonia via the Haber-Bosch process in a large-scale commercial installation. However, the amount of ammonia actually recovered in the vacuum trap was much lower than the amount of ammonia removed, driving up the specific energy costs. The decrease is ammonia recovery could be attributed to insufficient vacuum due to the very low vapor pressure of ammonia, high Henry

constant, and incompatibility of the vacuum pump with ammonia leading to decline in pump performance over time. Thus, work is still needed to develop better vacuum extraction methods capable of overcoming ammonia's high solubility (and low partial vapor pressure) to recover ammonia with reduced specific energy requirements.

Chapter 3:

A Reverse-Selective Ion Exchange Nanocomposite Membrane: Selective Phosphate Recovery via an Outer Sphere Complexation-Diffusion Pathway

Arpita Iddya, Piotr Zarzycki, Ryan Kingsbury, Charmaine Khor, Shengcun Ma, Jingbo Wang, Ian Wheeldon, Zhiyong Jason Ren, Eric M. V. Hoek, David Jassby

Abstract

Polymer nanocomposite materials are used across multiple fields such energy storage, power generation, water treatment, and resource extraction. Here, we report on a new discovery that enables phosphate-specific, reverse selectivity in cation exchange membranes. The specific selectivity is enabled through the in-situ growth of hydrous manganese oxide (HMO) nanoparticles (NPs) throughout a cation exchange membrane material that provide a diffusion pathway for phosphate, via reversible outer-sphere interaction. Other competing anions do not form these interactions with the NPs and are prevented passage through the membrane by the fixed negative charges of the polymer backbone. Upon incorporating the HMO NPs, the membrane's phosphate permeability increased 30 times compared to an unmodified membrane, and the membrane showed improved selectivity of 42, 37, and 43 for phosphate over other competing anions such as sulfate, nitrate, and chloride, respectively. By pairing the interactions of target ions with specific NPs, such nanocomposite ion exchange materials represent a new route for the synthesis of highly selective membranes capable of targeting a range of target ions for multiple applications.

3.1. Introduction

Ion selective separation membranes are used in clinical, environmental, food, and analytical applications. However, despite their extensive use, high-precision separations using membranes remains a challenge. Fine-tuning the selectivity of membranes could increase the efficiency of existing applications and enable novel processes in new fields such as smart materials, electronics, renewable energy, and resource extraction.[189] Increasing demand for resources and the depletion of natural reserves have made it imperative to find alternate sources and technologies to meet the growing need of a modern society.[190] For instance, deposits of phosphorus and potassium, critical ingredients in fertilizers, are expected to be significantly depleted by the end of the century.[191,192] Phosphate sequestration has been achieved through precipitation (as struvite), or extraction using organic solvents. These processes require substantial infrastructure investment, high maintenance costs, and may require further separation procedures.[193] Adsorption of phosphate onto various substrates has been extensively described. Phosphate-specific sorbents include zeolites, slag (produced during steel refining), and metal (hydro)oxides.[194–196] However, the recovery of phosphate from these adsorbents requires dramatic pH swings, making the process a batch process by nature. Furthermore, the use of strong acids/bases to drive the pH swing can damage the adsorbent, reducing its lifetime and requiring frequent replenishment.[194,197] In contrast, a membrane-based phosphate separation process will enable the continuous extraction of phosphate from wastewater without the need for material regeneration or the addition of chemicals to drive a pH swing, enabling the treatment of an environmental contaminant responsible for water resource eutrophication, and the production of a valuable commodity chemical.[193,194,198,199] However, few reports on membranes that are exclusively selective towards specific anions such as phosphate exist.[8,191,192,200–202] In addition, while phosphate is almost always mined, the continuous extraction

of phosphate ions from waste streams (such as municipal wastewater) would enable simultaneous treatment of an environmental contaminant responsible for water eutrophication and production of a valuable commodity chemical.[193,194,198,199]

Facilitated transport membranes (FTM) have been used to increase the selectivity of membranes towards specific targets by pairing the target molecule with "extractant" particles/functional groups embedded within the membrane matrix.[83,85,86,203] These extractants selectively bind with the target molecule or ion to form a complex, and transport of the target is then facilitated by either the motion of the complex (mobile carrier FTM) or hopping of the target from one carrier to another (fixed carrier/fixed-site FTM).[86] For ion separation, facilitated transport has been demonstrated using polymer inclusion or liquid membranes, but they suffer from poor stability.[90,204] To solve this stability limitation, we synthesized a novel organic/inorganic composite that enables facilitated transport of target ions through specific outer-sphere interactions between the target and an inorganic component within the membrane. Many transition metals, such as Zr, Cu, and Fe, have hard Lewis acid properties and exhibit preferential adsorptive selectivity toward phosphate.[205,206] Hydrous manganese oxide (HMO) has also been demonstrated to be an effective phosphate sorbent.[194,207–209] However, unlike other transition metals, HMO forms weaker outer-sphere complexes with phosphate, which can allow for phosphate ion hopping between adjacent manganese (di/hydro)oxide groups. [208,210] Embedding HMO NPs throughout a cation exchange membrane (CEM) (Figure 16A), which contains multiple fixed negative charges (e.g., from sulfonate groups) attached to the polymer backbone, creates a diffusion pathway for phosphate across the polymer matrix; other anions (e.g., Cl^-, NO_3^-, SO_4^{-2}) that do not form complexes with HMO are denied passage due to charge exclusion forces exerted by the CEM's fixed negative functional groups (Figure 16B).

Here we report on the synthesis, testing, and characterization of a facilitated transport mixed matrix membrane capable of selectively extracting phosphate from a mixed anion solution. The membrane is fabricated via *in situ* oxidation of manganese in a CEM to form HMO NPs embedded throughout the CEM (HMO-CEM). Through a combination of experimental and theoretical analysis, we characterize the transport properties of the hybrid material towards phosphate, explain the mechanisms responsible for phosphate transport, and determine that the rate-limiting step for phosphate transport is the complexation reaction between the HMO NPs and phosphate ions. This study explores the fundamental principles behind the selective transport of ions, and paves the way towards a new class of selective membrane materials.
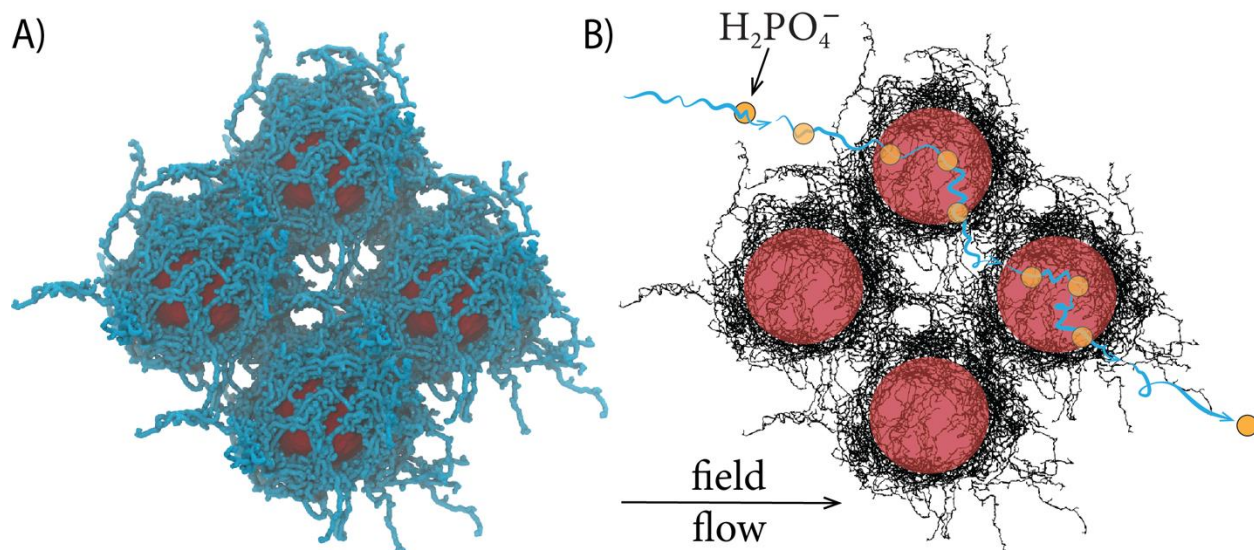
Figure 16: Molecular representation of the HMO-CEM membrane (A) and proposed mechanism of selective phosphate transport. The weak outer-sphere complexes $H_2PO_4^-$/HMO are formed within the Stern part of the EDL, which are relatively mobile and can migrate around HMO particle if subjected to external driving force like flow or weak electric field. The $H_2PO_4^-$ ions jump from one HMO particle to another through the intergel solution phase, that is, through the fluid-saturated micro and mesopore spaces. The phosphate ions adsorbed to HMO diffuse within the particle EDL in the direction of the flow or applied electric field.

3.2. Materials and Methods

3.2.1. Materials

A commercial CEM (Fumasep FKS-PET-130, FuelCellStore, College Station, TX) was used for this study and was either used without further modifications or modified as described below. Manganese chloride tetrahydrate ($MnCl_2.2H_2O$, Reagent grade, Sigma Aldrich), manganese (II) sulfate monohydrate ($MnSO_4.H_2O$, 99%, extra pure, ACROS Organics), sodium hydroxide (NaOH, pellets, certified ACS, Fisher), Sodium hypochlorite (NaOCl, 7.1% available chlorine, Clorox), sodium phosphate monobasic monohydrate ($NaH_2PO_4.H_2O$, 98%, ACS reagent, Sigma Aldrich), sodium sulfate (Na_2SO_4, Certified ACS, Fisher), sodium nitrate ($NaNO_3$, Certified ACS, Fisher), and sodium chloride (NaCl, ACS grade, Fisher) were used as received.

3.2.2. Preparation of HMO-CEM

HMO was loaded into the CEM, to form the Mixed Matrix Membrane (MMM) HMO-CEM, by using a three step process, modified from Qing and Pan.[211,212]

First, the CEM in its dry form was immersed in a solution containing 2.5 M $MnCl_2 \cdot 4H_2O$ and 3 M $MnSO_4 \cdot H_2O$ (5.5 M total Mn^{2+} concentration) for either 1 hour or 24 hours (to form a low-loading and high-loading (fully loaded) HMO-CEM, respectively). As a result, Mn^{2+} in solution exchange with H^+ in the membrane:[211]

$$2R - SO_3^- H^+ + Mn^{2+} \rightarrow (R - SO_3^-)_2 Mn^{2+} + 2H^+$$
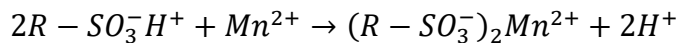
Next, an oxidizing solution was prepared by dissolving NaOH into a sodium hypochlorite solution to prepare a 1M NaOH solution with 7% NaOCl (w/w). The Mn-exchanged membrane was then immersed into the oxidizing solution for either 1 hour or 24 hours, for the low- and high-loading

HMO-CEM, respectively, and the Mn^{2+} counter-ions were oxidized to produce HMO (unbalanced):

$$(R - SO_3^-)_2 Mn^{2+} + NaOCl + NaOH \rightarrow 2R - SO_3 Na + HMO\ (MnO_2) + HCl$$
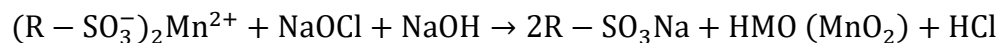
Finally, The HMO-CEM was then washed with copious amounts of deionized (DI) water and vacuum dried at 50 ºC for at least 12 hours. The prepared HMO-CEM was immersed in a 0.5 M $NaH_2PO_4.H_2O$ solution prior to experiments.

3.2.3. Membrane Characterization

The surface morphology and cross-sectional structure of the unmodified CEM and HMO-CEM were studied using scanning electron microscopy (SEM) equipped with energy dispersive X-ray spectroscopy (EDX) (ZEISS Supra 40VP SEM), and transmission electron microscopy (TEM; TF20 High Resolution EM, FEI). X-ray photoelectron spectroscopy (XPS; Kratos Axis Ultra DLD spectrometer equipped with a monochromatic Al Kα X-ray source) was used to characterize the elemental composition of the membrane surface and the oxidation state of manganese; all binding energies were referenced to the C 1s peak at 284.8 eV, and X-ray diffraction (XRD) was used to study the HMO structure. Chemical bonds in the membranes were evaluated using Fourier transform infrared spectroscopy (FTIR) operated in transmission mode (Thermo Scientific FTIR iS10 Smart iTR Basic), with a Ge prism as an internal reflection element. FTIR was also used to evaluate possible Mn-P interactions in the phosphate loaded HMO-CEM; for this, the sample was prepared by soaking the membrane in 0.5M $NaH_2PO_4 \cdot H_2O$ solution for 24 hours, rinsed with DI water, and dried at 50 ºC for 12 hours. To measure the total amount of HMO NPs incorporated, the HMO loaded membranes were weighed before and after placing them in a high temperature furnace. The weight of the ash is subtracted to achieve the weight of HMO nanoparticles. The HMO quantity is normalized to the membrane surface area to calculate HMO loading.

Water Uptake and Ion-Exchange Capacity (IEC) measurement

Water uptake by the membranes was determined by noting the weight after soaking them in DI water for 48 hours (w_w, g), followed by weighing the dried membranes (w_d, g) after placing them in a vacuum oven at 50 °C for 48 hours. The water uptake (w_u, g water/g of dry polymer) was given by[213]:

$$W_u = \frac{w_w - w_d}{w_d} \tag{1}$$

The IEC of the unmodified and HMO-CEM membranes was determined by a titration method.[214,215] The membranes were first soaked in 1 M HCl for 1 hour, followed by soaking in DI water for 30 minutes to remove residual acid. The prepared membranes were then soaked in 1N NaCl for at least 48 hours to allow for Na+ ions to exchange with H+ ions at the ion exchange sites. At the end of 48 hours, the NaCl solution was titrated against 1M NaOH solution to calculate ion exchange capacity of the membranes as:

$$IEC = \left[\frac{V_{NaOH}}{w_d}\right] * M_{NaOH} \tag{2}$$

Where, V_{NaOH} (L) is the volume of NaOH consumed, and M_{NaOH} is the molarity of the NaOH solution used. The concentration of fixed ions within the membrane (C_{fix}, mol charge/L water absorbed by the membrane) was then calculated using the equation[216]:

$$C_{fix} = \frac{IEC * \rho_w}{w_u} \tag{3}$$

Where, ρ_w is the density of pure water (g/cc).

3.2.4. Experimental Setup

Unmodified Anion Exchange Membrane (AEM), Cation Exchange Membranes (CEM) and HMO-CEMs were evaluated for phosphate (and other ion) transport using diffusion cells operated in

concentration-driven (Donnan dialysis) or concentration + field-driven (electrodialysis) mode as shown in Figure 17. In all experiments, membranes were prepped by immersing in a 0.5 M $NaH_2PO_4 \cdot H_2O$ solution for ~24 hours, followed by rinsing with DI water for 1 hour prior to the experiment. Experiments were conducted using either DI water or a 0.05 M Na_2SO_4 solution as the draw solution/anolyte. All experiments were conducted in triplicates, unless specified otherwise. 2 ml of sample was collected hourly from each of the chambers and analyzed for the various ion concentrations and pH. Ion exchange membranes are designed to minimize water transport. In our experiments, the solution volumes in both chambers did not change over time, indicating that osmosis was not a significant problem.

Phosphate transport was studied by graphing the normalized phosphate concentration in the receiving compartment (y) as a function of time (x). The normalized concentration (y-axis) was the concentration increase in the receiving compartment normalized to the concentration of the chamber at the end of the first hour.
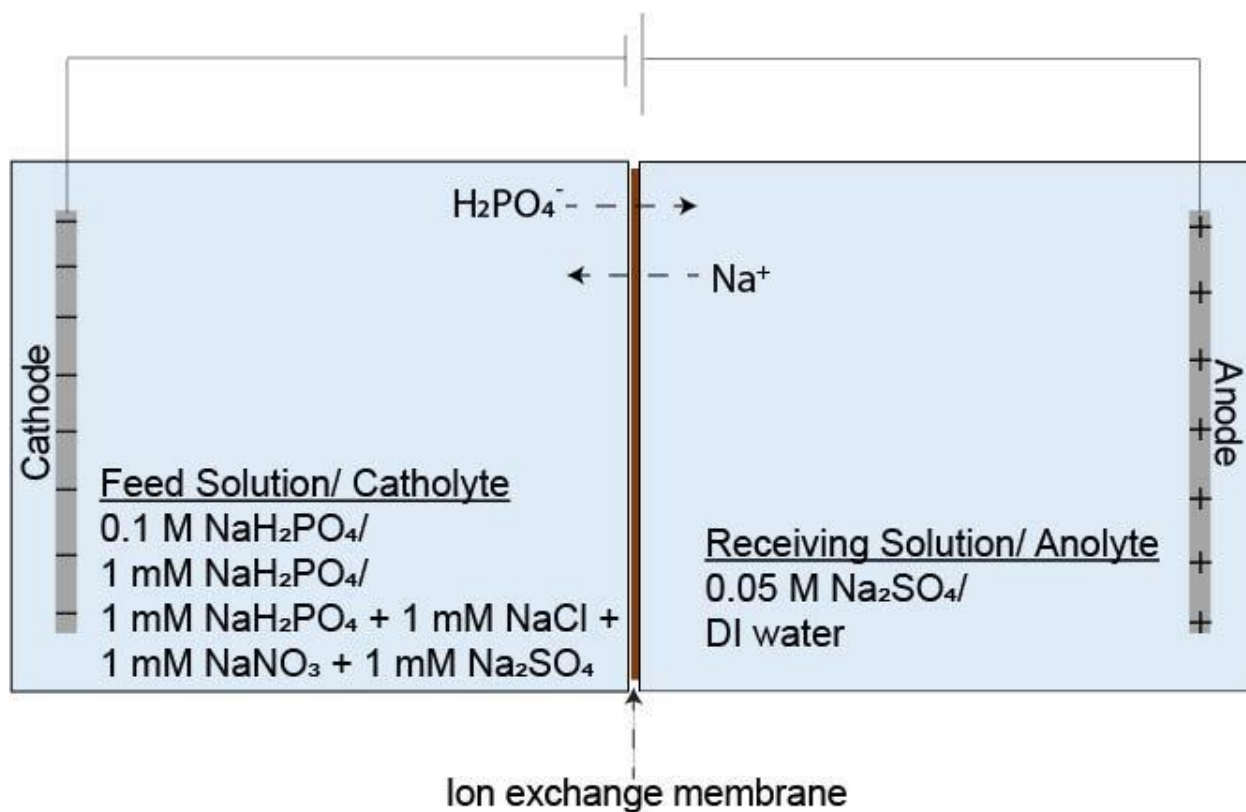
Figure 17: Schematic of experimental setup

Phosphate transport across the modified and unmodified membranes was tested using the following configurations:

Phosphate transport via Donnan dialysis

To demonstrate phosphate transport across the HMO-CEM, we first performed experiments without equilibrating the HMO-CEM in phosphate solution. The prepared membrane was kept in DI water before placing in the diffusion cell. One chamber of the cell was filled with 0.1 M $NaH_2PO_4 \cdot H_2O$ solution, and the other side with DI water. The increase in phosphate concentration in the receiving chamber was noted over a period of 6 days.

For transport of phosphate across the HMO-CEM solely due to a concentration difference, the prepared fully loaded HMO-CEM membrane was placed in a diffusion cell where one chamber was filled with a 0.1 M $NaH_2PO_4{\cdot}H_2O$ solution, and the other side with a 0.05 M Na_2SO_4 solution.

Finally, to study the presence of any ion exchange effect due to Na_2SO_4 in the receiving chamber, we performed similar Donnan dialysis experiments with an HMO-CEM equilibrated in NaH_2PO_4 solution with 0.1 M $NaH_2PO_4{\cdot}H_2O$ solution as the feed and DI water as the receiving chamber solution.

Phosphate transport under an applied electric field (electrodialysis)

For all experiments involving the application of electrical potentials as a driving force, Pt wires were used as both anode and cathode.

For transport of phosphate under an externally applied field in addition to a concentration difference, the membrane (unmodified, low loading HMO-CEM, or fully loaded HMO-CEM) was placed in a diffusion cell where one chamber was filled with a 0.1 M $NaH_2PO_4{\cdot}H_2O$ solution (the catholyte), and the other side with either a 0.05 M Na_2SO_4 solution (the anolyte). A potential of 0.8 V vs. Ag/AgCl (applied on the cathode, 2V cell potential) was applied to the anode using a potentiostat (CH Instruments 6005E; Austin, TX).

Phosphate selectivity test

The selectivity of the membranes towards phosphate over other common anions was tested by placing the modified or unmodified in a diffusion cell separating a solution containing an equimolar (1 mM) solution of $NaH_2PO_4{\cdot}H_2O$, Na_2SO_4, NaCl and $NaNO_3$ on one side (catholyte), and DI water on the other (anolyte). A potential of 0.8 V vs. Ag/AgCl (applied on the cathode; 2V cell potential) was applied across the membrane using a potentiostat. The selectivity of phosphate

was also measured under real-world competing ion concentrations in duplicates. In these experiments, the feed was composed of 5 mg/L PO_4^{3-}, 15 mg/L SO_4^{2-}, 10 mg/L Cl^- and 5 mg/L NO_3^- (using their sodium salts) and DI water was used as the receiving chamber solution.[217]

The effect of the competing ions on phosphate transport was studied by measuring phosphate flux in the absence of the competing ions and comparing it with the flux measured in the presence of competing ions. For this, a fully loaded HMO-CEM was placed in a diffusion cell where the catholyte was a 1 mM $NaH_2PO_4 \cdot H_2O$ solution, and DI water was the anolyte. A potential of 0.8 V vs. Ag/AgCl (applied on the cathode, 2V cell potential) was applied to the anode using a potentiostat.

Both experiments, the phosphate transport under applied electric field and the phosphate selectivity test, were also conducted for non-selective Anion Exchange Membranes (AEM) to compare performance, shown in Figure 18.
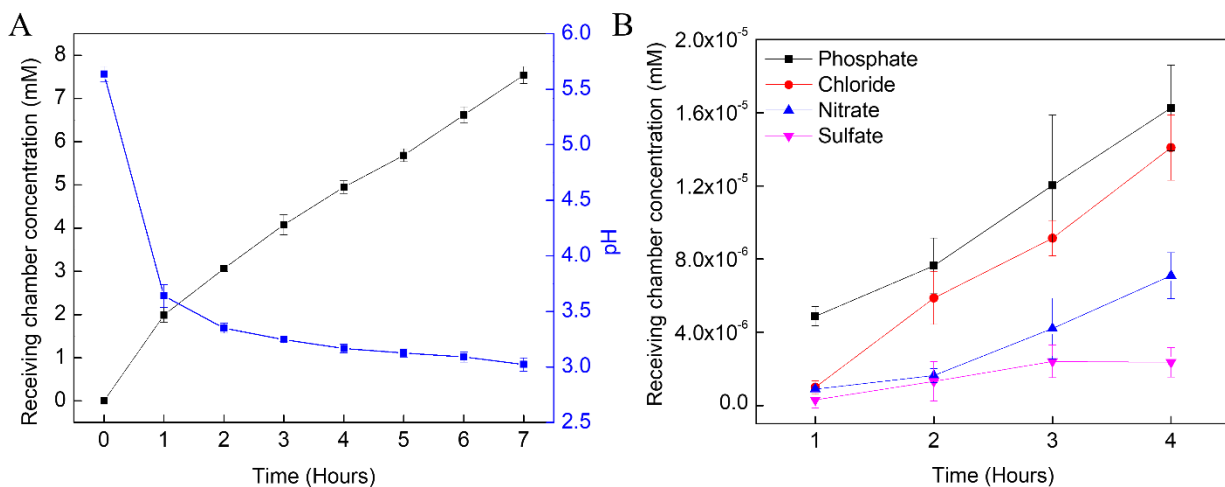
Figure 18: A) pH change and increase in phosphate concentration in the receiving chamber for an AEM under a potential driving force of 0.8V Vs Ag/AgCl with feed as 0.1 M $NaH_2PO_4.H_2O$ and 0.05M Na_2SO_4 as the receiving chamber solution. (B) Anion selectivity experiments using an AEM under a potential driving force of 0.8V Vs Ag/AgCl with feed as an equimolar solution

(1mM) of NaCl, $NaH_2PO_4 \cdot H_2O$, Na_2SO_4, and $NaNO_3$ and DI water as the receiving chamber solution.

3.2.5. Phosphate Concentration Measurements

Phosphate ion concentrations were determined by two methods. For experiments involving only phosphate ions, a spectrophotometric method using colorimetric test kits (HACH TNT844) were utilized, while for experiments with mixed anions, an ion chromatograph (IC) was used (Dionex Integrion HPIC System, ThermoFisher). When comparing the two analytical methods against each other using standard solutions, we observed a maximum error of ~20% at low concentrations. The sensitivity of HACH DR1900 decreases as the concentration reaches the instrument's detection limit of 1.5 mg/L. However, the two methods were used to measure solution concentrations in different ranges: IC for when phosphate concentration < 1.5 mg/L and HACH otherwise.

IC detection limit

For the selectivity experiments conducted with the feed composed of equimolar concentrations of NaCl, Na_2SO_4, NaH_2PO_4, and $NaNO_3$, Figure 19 depicts ion concentrations in the receiving chamber as calculated from the IC. The high variability in IC data is attributed to the concentrations of respective ions being close to the detection limit of the IC.
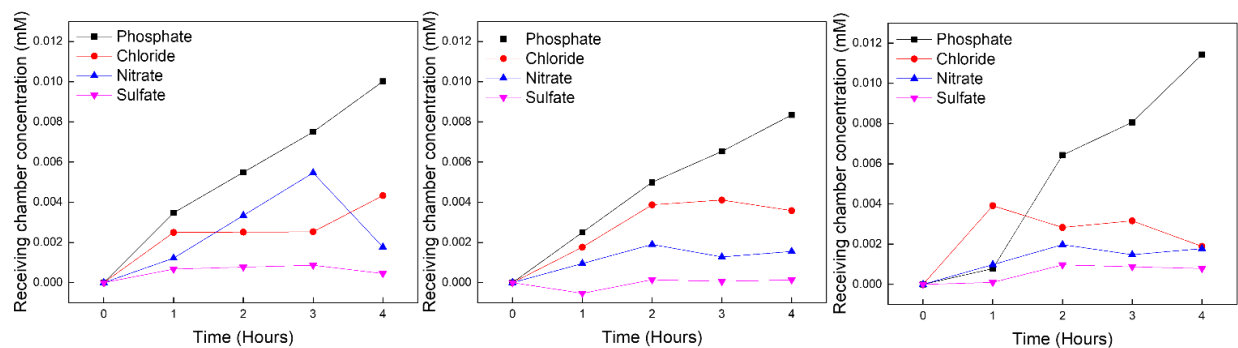
Figure 19: Results from triplicate experiments for phosphate selectivity using an HMO-CEM. High variability in the chloride and nitrate measurements as the concentrations are low and near the detection limit of the instrument.

The flux, J_i, of each anion was determined by calculating the slope of the concentration vs. time data generated during the transport experiments (m, moles/s), normalized by the membrane surface area (A_m):

$$J_i = \frac{m}{A_m}, \text{mol/m}^2/\text{s} \tag{4}$$

The separation factor of phosphate over other anions is expressed as a ratio of their individual fluxes (Equation 4) since the starting upstream concentrations for all anions in our experiments were the same (1mM); otherwise, separation factor is calculated as the ratio of flux normalized by the upstream concentration.[218]

$$\text{Separation factor} = \frac{Flux_{phosphate}}{Flux_{anion}} \tag{5}$$

Experimental transport numbers are calculated as the fraction of the overall current carried by the phosphate ion according to[219–221]:

$$t_{H_2PO_4^-} = \frac{nF}{It} * (C_0 V_0 - C_{end} V_{end}) \tag{6}$$

Where, n is the charge on the ion, F is Faraday's constant (96485 C/mol), C_0 and C_{end} are the initial and final concentrations in the anodic compartment respectively, and V_0 and V_{end} are the initial and final volumes of the anodic compartment. The denominator is the average current (I, A) recorded over the duration of the experiment (t, s). The experimental transport numbers are reported over the time period with constant phosphate flux, giving us the maximum transport number.

3.2.6. Specific Energy Consumption

The specific energy consumption (SEC) was calculated as:[222]

$$SEC_{phosphate} = \frac{(moles_{cf} - moles_{ci})M}{E_{mem}} \tag{7}$$

Where, $moles_{cf}$ is the final number moles in the feed chamber, $moles_{ci}$ is the initial number of moles in the feed chamber, M is the molecular mass of phosphate, and E_{mem} is the total energy consumption of membrane calculated as:

$$E_{mem} = \int_0^t UI(t)\, dt \tag{8}$$

Where, U is the applied voltage, and I is the current (as a function of time).

3.3. Molecular Modelling

In order to provide molecular-level insight into phosphate ion transport across, and interaction, with the HMO-CEM, we carried out a series of molecular dynamics simulations for: *i)* NaH_2PO_4 electrolyte solution, *ii)* NaH_2PO_4 electrolyte solution in the presence of the HMO particle, *iii)* within the CEM membrane, and *iv)* within the composite HMO-CEM membrane. Prior to running molecular dynamics simulations, we have developed the interaction models (i.e., force-field parameters) for poly(ether ether ketone)s (PEEKs) and sulfonated poly(ether ether ketone)s (sPEEKs) and $H_2PO_4^-$ ions using the ab initio calculations. This step consisted of geometry optimization, population analysis of the electron density to assign partial charges to atoms, and vibration analysis to determine force constants for bond stretching and angle bending dynamics. The ab initio calculations were carried out using the Density Functional Theory (B3LYP exchange-correlation function with 6-311++G** basis set) as implemented in the potential with parametrization taken from existing datasets.[223–225]

Next, we tested these force fields in the bulk water phase, which was modeled using rigid three-point water model OPC3.[226] We chose the OPC3 model because it accurately predicts solutes hydration environments and water dielectric properties.[225,227] Finally, we constructed a polymeric membrane by randomly arranging 150 sPEEKs polymers (70% sulfonated) polymer molecules in

the bulk water phase and allowing compaction using the Grand Canonical Monte Carlo scheme that gradually increases the polymer/water ratio via progressive dehydration until the experimentally determined water uptake was reproduced. In the last step of preparation of the input configuration for molecular dynamics, we inserted $H_2PO_4^-$ and Na^+ ions into the water-saturated polymeric matrix to generate 0.1 M NaH_2PO_4 solution. We have also developed a similar simulation system with an embedded spherical HMO particle (diameter ~ 10 nm). We used the pyrolusite crystal structure[228] to generate initial atomic coordinates for the HMO particle. The surface oxygen atoms were replaced by the hydroxyl groups resulting in the charge-neutral particle. The structure of the spherical HMO particle was allowed to relax at elevated temperature (T = 500K) to resemble the less-ordered HMO particles in the HMO-CEM composite. To compare ions mobility in the system without sPEEK membrane, we prepared two additional simulation systems: $H_2PO_4^-$ and Na^+ ions immersed in water with and without the HMO particle.

All simulations were carried out using an identical simulation protocol. The initial atom configurations were minimized using the mixture of the steepest descent and conjugate gradient minimization schemes. In all simulations, the number of water molecules and $H_2PO_4^-$ were kept constant, which allows for the comparison of phosphate mobility under different conditions. The simulations were carried out with 100 $H_2PO_4^-$ and the fluid flux through the membrane and electrolysis of water were neglected. Next, the systems were brought to the desired temperature and density by heating for 200 ps in the canonical ensemble (NVT), followed by 25 ns simulation run in the isobaric–isothermal ensemble (NPT). Finally, the production simulations were carried out in the canonical ensemble for another 100 ns. The final production runs were carried out with and without the static electric field and repeated 10 times for each system composition, starting from slightly different initial configurations of atoms. We analyzed the last 50 ns to gain insight

into ion mobility and modes of interaction with the HMO-CEM membrane. The pressure was controlled using Berendsen barostat[229] with the pressure relaxation time equals 2 ps, whereas temperature was controlled using Langevin thermostat[230] with collision frequency equals 1.0 ps^{-1}. The molecular simulations were carried out using two GPU-optimized simulation engines: PMEMD simulation engine from Amber[231] and GMX-MDRUN from GROMACS[232].

Table 1: Diffusion coefficient of sodium (Na^+) and phosphate ($H_2PO_4^-$) ions from equilibrium molecular dynamics simulations with and without an electric field.

	Diffusion coefficients D_i (10^{-9} m^2/s)				
	NaH$_2$PO$_4$ solution		Unmodified CEM	HMO-CEM	HMO-CEM
	c=0.003 mol/dm^3	c=0.1 mol/dm^3	No field, w_u=0.16 g/g	No field w_u=0.24 g/g	Field E=0.33 V/cm w_u=0.24 g/g
Na^+	1.345	0.691	0.0796	0.0869	0.1067
$H_2PO_4^-$	0.899	0.313	0.0318	0.0886	0.1272

*The diffusion coefficients used in the mathematical model (Table 2) are self-diffusion coefficients of ions and thus correspond to the infinitely diluted solution. The interaction model used here reproduces these values accurately (see diffusion coefficients for c=0.003 mol/dm^3 solution above, and Figure 20). The diffusion of ions decreases with increasing electrolyte concentration (Figure 20) and heterogeneity of the system. The diffusion coefficients calculated for the ions within the membrane reflect the complexity of the intermolecular interaction, presence of the external electric field, confinement due to polymeric membrane, and restriction in mobility due to ion complexation and sorption to negatively charged sPEEK polymer and HMO particle.
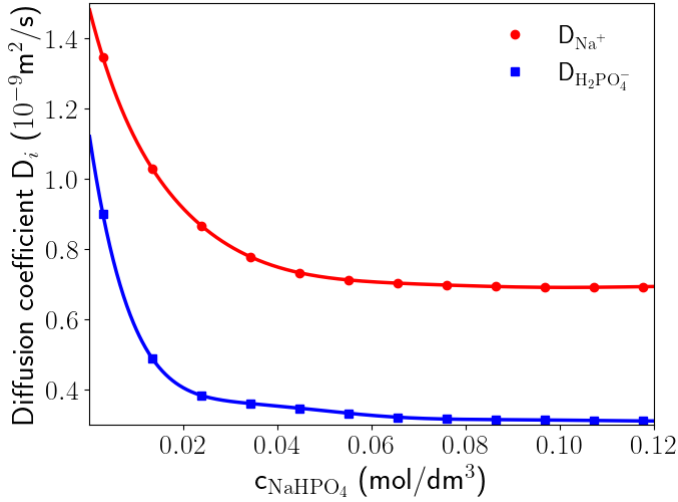
Figure 20: Diffusion coefficients of sodium (Na^+) and phosphate ($H_2PO_4^-$) in aqueous solution as a function of NaH_2PO_4 concentration. Results obtained using the lowest concentration tested (0.003 mol/dm3) are used to estimate the self-diffusion coefficients (see Table 1, 2).

3.4. Phosphate Transport Mathematical Modelling

The mathematical model for phosphate ion transport was developed based on the microheterogeneous model for ion exchange membranes.[73,233] Traditionally, the model describes two distinct phases within the membrane - a "gel phase" and an "intergel solution phase". The gel phase encompasses the microporous regions containing the polymer chains with fixed charges, with the counter and co-ion containing solution balancing these fixed charges; the intergel phase consists of the meso- and macroporous spaces filled with electroneutral equilibrium solution (equivalent to the bulk external solution).[73] The ion flux density of species i (counter/ co-ion), J_i, in a two-phase membrane is proportional to the gradient of electrochemical potential across it, given by[73]:

$$J_i = -L_i^* \frac{d\mu_i}{dx} \tag{9}$$

Where, L_i^* is the effective conductance coefficient characterizing the multiphase system (similar to a diffusion coefficient), μ_i is the electrochemical potential of species i, and x is the differential length under consideration in the direction of transport. The electrochemical potential, μ_i, in equation 9 can be presented as a function of concentration of species i, C_i, and electrical potential φ, as[234]:

$$J_i = -L_i^* * \left(\frac{d\mu_i^0}{dx} + RT\frac{dC_i}{dx} + z_iF\frac{d\varphi}{dx}\right) \tag{10}$$

Where, μ_i^0 is the standard chemical potential, z_i is the charge of species i, and F, R, and T are the Faraday's constant (C/mol), gas constant (J/mol/K), and temperature (K), respectively. Using the microheterogeneous model for the two-phase system where the superscript g refers to the 'gel phase' and the superscript 'int' refers to the intergel phase within the membrane, L_i^* is calculated as:

$$L_i^* = [f_g(L_i^g)^\alpha + f_{int}(L_i^{int})^\alpha]^{1/\alpha} \tag{11}$$

Where, f_g and f_{int} are the volume fractions of the gel and intergel phases, respectively, which were approximated from the water uptake capacity of the membrane as:

$$V_{water} = \frac{w_u * w_d}{\rho_w} \tag{12}$$

$$V_{gel} = \frac{w_d}{\rho_{gel}} \tag{13}$$

$$f_{int} = \frac{V_{water}}{V_{water} + V_{gel}} \tag{14}$$

$$f_g = 1 - f_{int} \tag{15}$$

Where, V_w is the volume of water taken up by the membrane during water uptake measurements assuming the water is present in the intergel region and V_{gel} is the volume of the polymer gel phase. Although this assumption slightly contradicts equation 3, where the water uptake is assumed to contribute entirely to the non-electroneutral solution phase next to the fixed charges in membrane, the value of f_{int} and f_g obtained using this approximation fall within the acceptable range reported in literature.[235,236]

In equation 11, α is the structural parameter of the membrane, which varies from -1 to 1 and represents the connectivity of the two phases (where -1=series and 1=parallel),[73] and $L_i{}^g$ and $L_i{}^{int}$ are the effective conductance coefficients of the gel and intergel phases, respectively, calculated from the Nernst-Einstein relation as:

$$L_i^g = \frac{D_i^g C_i^g}{RT} \tag{16}$$

$$L_i^{int} = \frac{D_i^S C_i^S}{RT} \tag{17}$$

Where, $D_i{}^g$ and $D_i{}^S$ are the diffusion coefficients of the species i in the gel and solution phase, respectively, $C_i{}^g$ and $C_i{}^S$ are the concentrations of ions in the gel and solution phase, respectively, where i represents either co-ions (co) or counter-ions (ct). Their values are obtained from equations described below. R is the universal gas constant, and T is the temperature (K).

The co-ion (C_{co}^g) and counter-ion concentration (C_{ct}^g), at the membrane- feed interface (within the membrane) are calculated using Donnan equilibrium, assuming that the co-ion is $H_2PO_4^-$, and the counter-ion is Na^+.[237]

$$C_{co}^g = C_s * \sqrt{\Gamma} \exp\left(-asinh\frac{C_{fix}^g}{2C_s\sqrt{\Gamma}}\right) \tag{18}$$

$$C_{ct}^g = \frac{-(z_{co}C_{co}^g + z_{fix}C_{fix}^g)}{z_{ct}} \tag{19}$$

Where, C_s is the solution concentration, z_{fix} is the dimensionless signed charge and C_{fix} the concentration of the fixed charges on the membrane, respectively, z_{co} and z_{ct} are the dimensionless signed charges of the co- and counterions, and Γ is assumed to be 1 for an "ideal" Donnan model, meaning that both the bulk electrolyte and ions inside the membrane behave as ideal solutions, i.e., the activity coefficients of the solutions inside and outside the membrane are the same.[237]

The diffusion coefficients (D_i) in the gel phase are calculated by simultaneously solving equations for the ionic conductivity of the membrane (κ) and the salt coupled diffusion coefficient (D_s^m)[218,238] obtained from experiments:

$$\kappa = \frac{F^2}{RT}(z_{ct}^2 D_{ct}^g C_{ct}^g + z_{co}^2 D_{co}^g C_{co}^g) \tag{20}$$

$$D_s^m = \frac{D_{ct}^g D_{co}^g (z_{ct}^2 C_{ct}^g + z_{co}^2 C_{co}^g)}{(z_{ct}^2 D_{ct}^g C_{ct}^g + z_{co}^2 D_{co}^g C_{co}^g)} \tag{21}$$

Where κ is the membrane ionic conductivity, obtained from membrane specifications, F is the Faraday constant, D_{co}^g and D_{ct}^g are the diffusion coefficients of the co- and counter ion respectively in the gel phase of the membrane.

Accounting for embedded nanoparticles in the CEM

The presence of NPs with a certain volume fraction alters the transport properties of the membrane. According to the microheterogenous model presented by Porozhnyy et. al., for the case of charged NPs, the particle body is considered to be a non-conductive phase, and the ions are assumed to transport through the electrical double layer (EDL) adjacent to each particle.[73] In our system as well we consider the particle body to be a non-conductive phase. For simplicity, we also assume

that the NPs within the HMO-CEM are uncharged. These uncharged HMO NPs are immobilized in the meso- and macropores and occupy part of the volume in the intergel solution phase, with the remainder occupied by the external electroneutral solution as before. This divides the intergel phase of the membrane into a two-phase system with the volume fraction of the gel, f_{sin} (volume of solution/ total volume of intergel phase). The effective conductance of the membrane can then be described as[73]:

$$L_i^* = [f_g(L_i^g)^\alpha + f_{int}(f_{sin}^{1/\beta} * L_i^{int})^\alpha]^{1/\alpha} \tag{22}$$

Where, β is another structural parameter of the membrane, similar to α. Equations 9-25 are then used to calculate the effective conductance coefficient for each ion for each case (presence and absence of HMO), which are then used to calculate the transport number. The transport number (t^*, unitless) can be described as the fraction of total current carried by each ion.[237] A higher transport number thus implies greater transport of an ion in relation to other species present in solution:

$$t_i^* = \frac{L_i^*}{\Sigma_i L_i^*} \tag{23}$$

Where, i is the specific ion under consideration. The model here calculates the transport number as a function of the effective conductance coefficient for a two ion system (Na^+ and $H_2PO_4^-$), and does not consider the effect of the pH change in the catholyte and anolyte. However, under electrodialysis conditions, water electrolysis leads to dramatic pH swings in both chambers. The increasing concentrations of protons in the anolyte leads to a greater driving force for these ions, which decreases the portion of current carried by phosphate ions.[239] Therefore, to account for the protons that carry a large amount of current, we calculate transport numbers by extrapolating the sum of sodium and proton transport (in moles) from the experiment (from equation 6), and use it

to calculate the transport number in the model, assuming that the sodium and proton transport are minimally affected by the presence of HMO NPs:

$$t^*_{H_2PO_4} = \frac{L^*_{H_2PO_4}}{L^*_{H_2PO_4} + L_{(Na^+ + H^+)expt}} \tag{24}$$

The flux of the ions is calculated using equation 9, expanded as:

$$J_i = L^*_i * (RT\frac{dC_i}{dx} + F\frac{dE}{dx}) \tag{25}$$

The concentration profile for the co-ion along the length of the membrane is modeled using an empirical equation proposed by Galama et. al., as used by Kingsbury et. al.[237,240]:

$$C^m(x) = C^m_L + (C^m_0 - C^m_L) * (\frac{\delta - x}{\delta})^n \tag{26}$$

Where, the superscript m refers to the membrane phase values, C^m_L refers to ion concentration at the membrane-permeate interface (assumed to be 0 for no phosphate ion present in the receiving compartment), C^m_0 refers to the ion concentration at the membrane-feed interface (calculated using eq.18), δ is membrane thickness, x the position within the membrane, and n is an adjustable parameter that modifies the shape of the curve (Figure 21); for $n = 1$, the profile is linear, growing increasingly exponential as the value of n increases. The parameter, n, in equation 26, and the structural parameters, α and β, are treated as adjustable parameters and fit to the model. The performance of the model, based on the average flux and transport number, was evaluated using n values of 1, 5, 10, and 25. The structural parameter of the membrane, α, which represents the connectivity of the two phases (gel and intergel) in series or parallel was varied as -0.1, 0.1, 0.35, 0.5, 0.7, and 1, and β was optimized to give lowest RMSE value (table 3).

The transport numbers and fluxes for the three membranes (unmodified, low loading HMO-CEM, and high loading HMO-CEM), are calculated by discretizing the membrane thickness into 25 smaller segments of equal length and applying an iterative approach to solve the equations given above using Python (v.3.8). The parameters used in the model such as membrane thickness (δ) and the membrane conductivity (k) for an unmodified membrane were obtained from membrane specifications, while the concentration of fixed charges (C_{fix}), concentration of feed (C_i^S), and water uptake (w_u) were obtained from experiments. The water uptake measurements were then used to calculate the volume fractions of each membrane phase, and the values for ion diffusion coefficients in solution (D_i^S) were obtained from literature.[241,242] The value of each parameter used in the model is listed in Table 2.

The effective conductance coefficient is a complex descriptor of the mutual-diffusion (conductance) coefficients accounting for ion-ion interactions in the EDL, membrane properties, and coupled charge transfer across membrane. The coefficient value is governed by model input parameters such as feed concentration, applied potential, IEM properties, and the coupled diffusion coefficients of the ions across the IEM. As a result, the conductance coefficient is unique for a specific set of conditions and can be altered to simulate fluxes at different concentrations and applied fields.
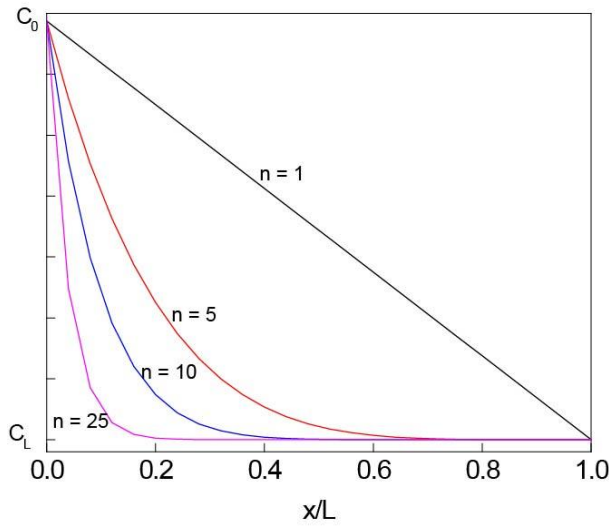
Figure 21: Concentration profile of co-ions calculated using equation 26.

Table 2: Parameters used in the mathematical model

Ion exchange membrane properties						
IEC (unmodified) [meq/g]	IEC (low HMO) [meq/g]	IEC (HMO) [meq/g]	w_u (unmodified)	w_u (low HMO)	w_u (HMO)	δ (thickness) [μm]
0.73 ± 0.01	0.71 ± 0.01	0.69 ± 0.06	0.162	0.168	0.237	110
Solution Properties			Constants			
C^S [M]	D_{Na^+} [m²/s]	D_{H2PO4^-} [m²/s]	R [J/mol/K]	T [K]	ρ_w [g/L]	E_{cell} [V]
0.1	1.33E-9	0.879E-9	8.314	298	998	2
Volume fractions						
Unmodified CEM		Low loading CEM			High loading CEM	
f_g	f_{int}	f_g	f_{int}	f_p	f_g $\quad$ f_{int} $\quad$ f_p	
0.872	0.128	0.795	0.191	0.013	0.741 $\quad$ 0.235 $\quad$ 0.024	

Table 3: RMSE values when optimizing n and α (β = 1)

Flux (RMSE*)				t_{PO4} (RMSE*)	
α = 0.3, n = 1	2.81E-07	n = 10, α = -0.1	3.14E-08	n = 10, α = -0.1	2.47E-03
α = 0.3, n = 5	4.55E-08	n = 10, α = 0.1	5.8E-08	n = 10, α = 0.1	2.63E-03
α = 0.3, n = 10	8E-08	n = 10, α = 0.3	3.28E-08	n = 10, α = 0.35	2.29E-03
α = 0.3, n = 15	9.69E-08	n = 10, α = 0.5	1.56E-08	n = 10, α = 0.5	2.01E-03
α = 0.3, n = 25	1.11E-07	n = 10, α = 0.7	3.65E-08	n = 10, α = 0.7	2.57E-03
α = 0.3 & 0.5[#], n = 15,10` &5[#]	**1.6E-8**	n = 10, α = 1	9.33E-08	n = 10, α = 1	5.11E-03

		n =15,10` &5[#], α = 0.3 & 0.5[#]	**1.6E-8**	n = 10 &5[#], α = 0.3 & 0.5[#]	**1.79E-3**

* Root-mean-square error is defined as $\sqrt{\frac{\sum_n(prediction-experiment)^2}{n}}$, where n is indexed over all data points (from the three HMO loadings).

` For Low loading HMO-CEM

[#] For high loading HMO-CEM

3.5. Results and Discussion

HMO loading for the two membranes, high loading HMO-CEM and low loading HMO-CEM, was determined to be 117 mg MnO_2/g of membrane and 69 mg MnO_2/g of membrane, respectively. The effect of increasing the HMO loading on the membrane properties such as ion exchange capacity, water uptake, and volume fraction have been described in the SI (Table 2).

Visual investigation of the membranes demonstrates the successful modification of the CEM with HMO; while the pristine CEM is a white, slightly transparent material, the HMO-CEM is transformed into a solid black material (Figure 22A, B). The structure and uniformity of the HMO immobilized within the membrane was investigated using transmission electron microscopy (TEM), and X-ray photoelectron spectroscopy (XPS), and X-ray diffraction (XRD). Cross-sectional TEM micrographs of the HMO-CEM clearly show the presence of HMO NPs distributed uniformly throughout the membrane, with an average size of approximately 79.4 ±23.1 nm, while TEM micrographs of the unmodified CEM show no distinguishing features (Figures 22C, D). XRD analysis of the particles and HMO-CEM membrane showed no distinguishing peaks associated with the HMO particles, suggesting that the particle had an amorphous structure (Figure S23). The XPS spectrum of the modified HMO-CEM shows a distinct Mn peak at ~ 642.8 eV, demonstrating the successful incorporation of Mn, at least at the surface of the material (Figure 22E).[243,244] Fourier transform infrared spectroscopy (FTIR) peaks (Figure 22F) of the HMO-CEM show a weak broad

band with a peak centered around 3400 cm^{-1} resulting from the stretching vibrations of –OH following HMO loading, a broadening of a peak at 600 cm^{-1}, and two additional peaks at 712 cm^{-1} and 681 cm^{-1}, corresponding to the MnO$_x$ stretching, bending, and wagging vibrations, respectively.[245,246]
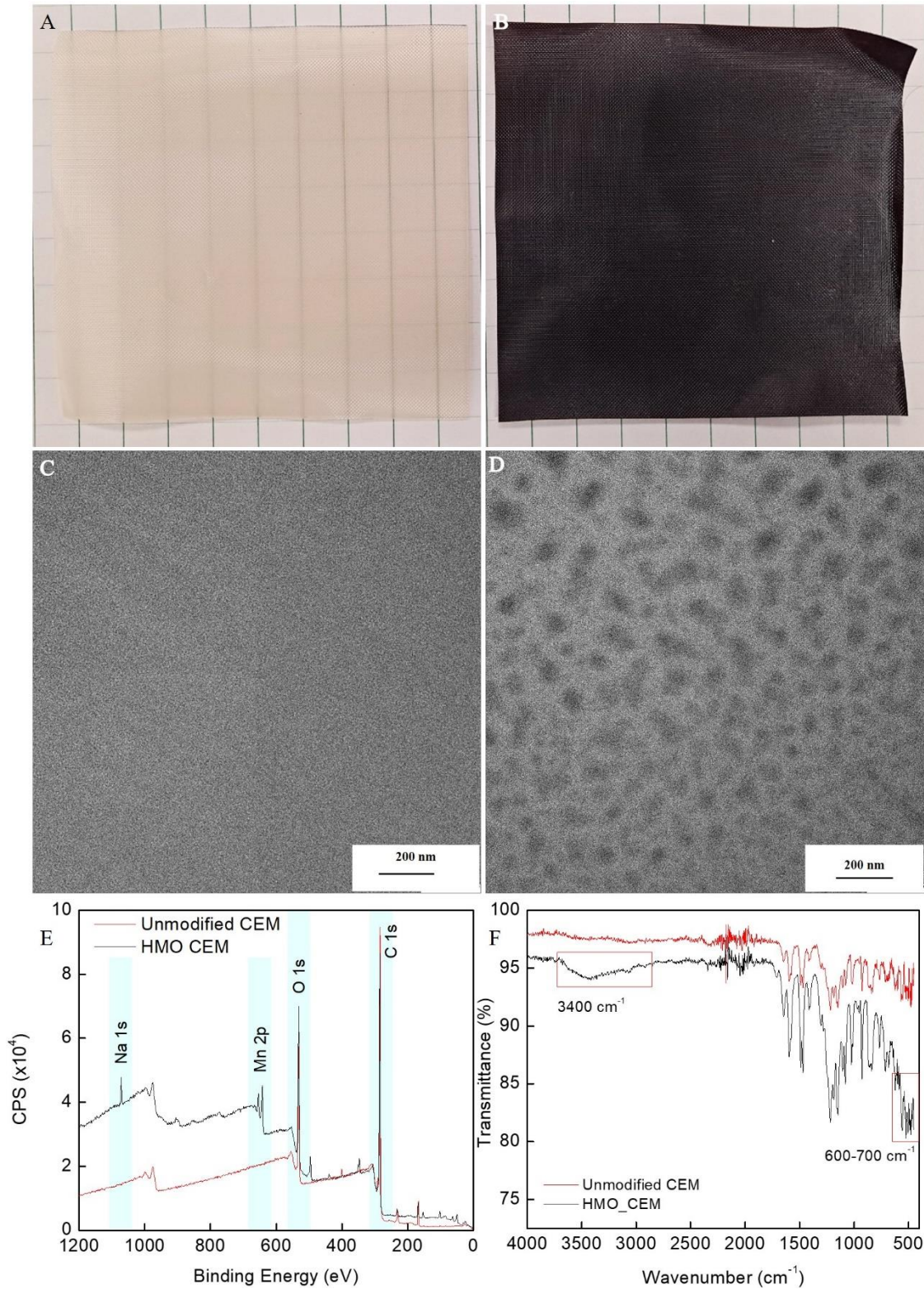
Figure 22: Photographs of the A) unmodified CEM and B) HMO-CEM. Cross-sectional TEM micrographs for C) unmodified CEM and D) HMO-CEM show Mn nanoparticles embedded uniformly within the HMO-CEM matrix with an average particle size of ~79.4 ±23.1 nm. XPS

spectra (E) shows the Mn peak of the HMO-CEM at ~642.8 eV, demonstrating successful incorporation of Mn into the CEM; and FTIR spectra (F) shows a weak band at 3400 cm^{-1} resulting from stretching of –OH, and peak broadening at 600-700 cm^{-1} corresponding to MnO$_x$ stretching and bending vibrations.

The HMO crystal structure of the nanoparticles, as well as its structure within the membrane was studied using X-ray diffraction (XRD; Panalytical X'Pert Pro X-Ray Diffractometer). The lack of clear diffraction peaks in the pattern presented in Figure 23 indicate that the HMO nanoparticles have an amorphous, glassy, or disordered crystalline nature of the HMO nanoparticles.
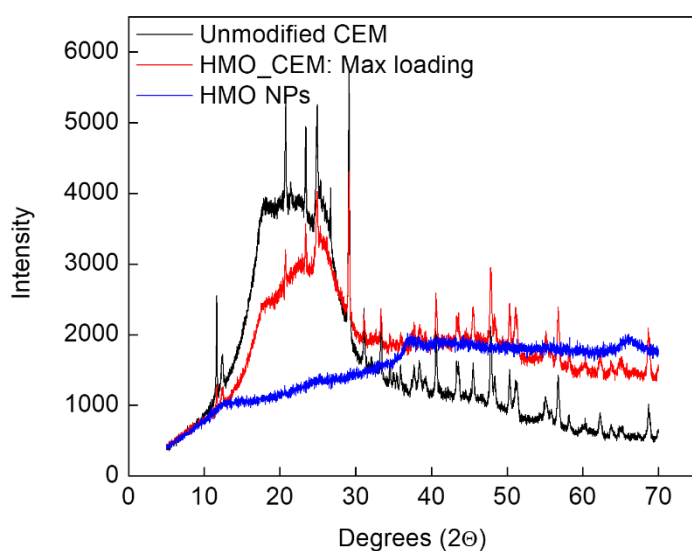
Figure 23: XRD pattern of an unmodified CEM, high-loading HMO-CEM, and HMO nanoparticles formed outside of the membrane.

Identifying Fumasep FKS Polymer

The CEM used in this study (Fumasep FKS PET-130) has a polymer backbone based on a proprietary hydrocarbon structure (as per the manufacturer's specifications). The lack of F peaks (688-689 eV) in the XPS spectra of the unmodified CEM (Figure 22E), indicates that the Fumasep FKS polymer is not a fluorinated polymer. Moreover, comparing FTIR spectra of a Nafion® membrane with that of our FKS PET-130, we see a clear difference between the two polymers

(Figure 24A). Therefore, to identify the FKS polymer, we compared the FTIR spectra to that of other non-nafion based cation exchange polymers from previous studies.[247,248]

FTIR analysis of the FKS polymer shows the presence of sulfonate groups with peaks at 1155-1207 cm^{-1} and 1050-1100 cm^{-1}, which correspond to SO_3^- symmetric and asymmetric stretching, and SO_3^- symmetric stretching, respectively (Figure 24A).[247] Additionally, the peak at 950-1000 cm^{-1} can be attributed to C=C (monosubstituted alkene) bending. With this information, we can narrow down the possibility of the polymer to either sPEEK or PSS.[248] Comparing the FTIR spectra of the FKS polymer membrane with that of sPEEK and PSS, we conclude that sPEEK exhibits the best overall fit (Figure 24B). [249–252]
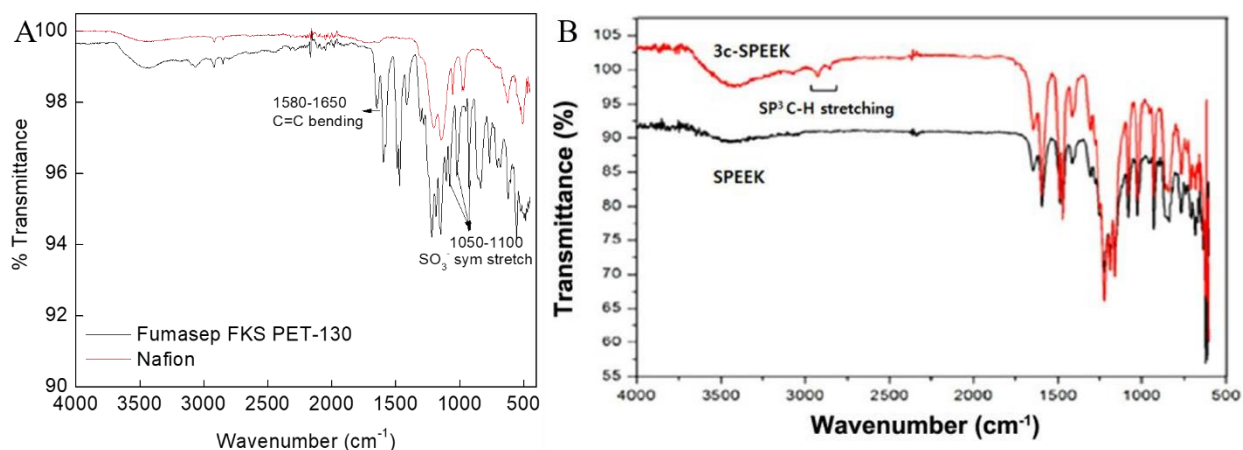
Figure 24: A) FTIR spectra of the unmodified CEM, Fumasep FKS PET-130, compared to that of Nafion®. (B) FTIR spectra of sPEEK and 3c-sPEEK (KBr), published in *Macromolecular Research*, 2014.[252]

Transport and Selectivity of Phosphate using HMO-CEM

Phosphate transport across an unmodified CEM and HMO-CEM with two different HMO loadings shows that the transport rate is highly dependent on HMO loading. The setup for these experiments is described in supplementary materials (section 1) and follows the schematic in Figure 17. As seen in Figure 25A, the unmodified CEM showed extremely low transport rates (0.8 x10^{-8} mol·m$^-$

$^{2}\cdot s^{-1}$, Figure 25A). This result is not surprising considering the high concentration of fixed, negatively charged sulfonate groups within the polymer matrix, which prevent the uptake and passage of phosphate anions. Phosphate transport across the HMO-CEM (with no applied potential, i.e., Donnan dialysis, and with an applied potential, i.e., electro-dialysis) is shown in Figure 25A and 26. For both HMO-CEM loadings, the phosphate concentration in the receiving compartment increased over time. For the high HMO loading case, under the effect of the combined driving forces (concentration gradient + electric field; black triangles, Figure 25A), phosphate concentration in the receiving (anolyte) compartment increased for the first three hours, with a flux of 21.7×10^{-8} mol$\cdot$m$^{-2}\cdot$s^{-1} (while this flux is low compared to anion fluxes through anion exchange membranes, the flux can be increased by increasing the driving force and, in addition, the membrane exhibits dramatically enhanced selectivity towards phosphate – more on this below). However, after three hours the flux declined to 5.4×10^{-8} mol$\cdot$m$^{-2}\cdot$s^{-1}. We speculate that this flux decline is a result of pH-induced changes in phosphate speciation. As the experiment progressed, the pH of the anolyte rapidly declined from 5.5 at t=0 h to 2.9 at t=3 h as a result of water electrolysis (Figure 25A). Under the applied electric field, protons generated at the anode migrate towards the cathode, penetrating the HMO-CEM as they migrate between the two chambers, and reducing the inter-membrane pH. Since the pKa$_1$ of phosphate is 2.1, as the pH approaches this level, fewer phosphate molecules complexed with the HMO NPs are ionized ($H_2PO_4^-$ vs. H_3PO_4), making them less susceptible to the electrophoretic driving force and slowing their transport across the membrane. Under Donnan dialysis conditions, the pH decline was not as significant (possibly as a result of accumulation of phosphate ions) compared to the pH under electro-dialysis conditions (pH declined to 4.7 from 5.7 after 7 hours). Because the pH never dropped to extreme levels under these conditions, phosphate flux was constant throughout the experiment (5.1×10^{-8} mol$\cdot$m$^{-2}\cdot$s^{-1}).

This is further evidenced by the lower phosphate flux and pH drop under an applied potential when using an HMO-CEM with low HMO loading (2.6×10^{-8} mol·m^{-2}·s^{-1}) (Figure 25A, 26 and section 2.3 of supplementary materials). The pH in the anolyte, for the low HMO loading experiments, declined to 3.3 over the duration of the experiment, and the flux remained fairly constant as compared to that using a high-loading HMO-CEM. The lower flux for the low-loading HMO-CEM highlights the importance of the embedded HMO NPs in enabling phosphate transport across the CEM. Table 4 summarizes the permeability values measured under donnan dialysis conditions for all membranes.

Membrane selectivity towards phosphate

Membrane selectivity experiments revealed superior selectivity of the HMO-CEM in transporting phosphate over other competing anions (Figure 25B). The experiments were conducted under electrodialysis conditions with a mixture of electrolytes, all at an initial concentration of 1 mM, in the catholyte and DI water as the anolyte. For the unmodified CEM, extremely low transport of all anions was observed with a slight preference for Cl$^-$ transport over other species. (Figure 25C). This result is attributed to the large concentration of negatively charged sites on the CEM. We also tested the selectivity of an anion exchange membrane (AEM). The AEM showed high transport rate for all anions, with little selectivity of phosphate over other anions (Figure 25A). The separation factor of phosphate over other anions was determined to be 1 (for chloride), 5 (for sulfate), 1.5 (for nitrate) (Figure 25B). In contrast to both, the HMO-CEM enabled phosphate to pass through the membrane (with a flux of 11.9E-8 mol/m^2/s), while still rejecting all other anion species (Figure 25D). While the unmodified CEM shows a gradual increase in Cl$^-$ concentration over time, the HMO-CEM shows an increase in Cl$^-$ concentration only in the first hour followed by a much lower Cl transport rate. This initial increase in Cl$^-$ concentration for HMO-CEM is

attributed to the chloride ions added into the matrix as a result of using NaOCl during membrane preparation. Moreover, the drop in Cl$^-$ transport rate across the HMO-CEM as compared to the unmodified CEM could be due to the decrease in the intergel (the region of the CEM that allows co-ion transport) volume upon introduction of HMO NPs.[78,253] Based on the fluxes of the different anions measured in these experiments, the separation factor of phosphate over chloride, nitrate, and sulfate was determined to be 20, 100 and 47, respectively. The large standard deviation in separation factors for the competing anions are due to the low concentrations of these ions (near the detection limit of the IC), resulting in large variability in concentration measurement, as shown in Figure 19.
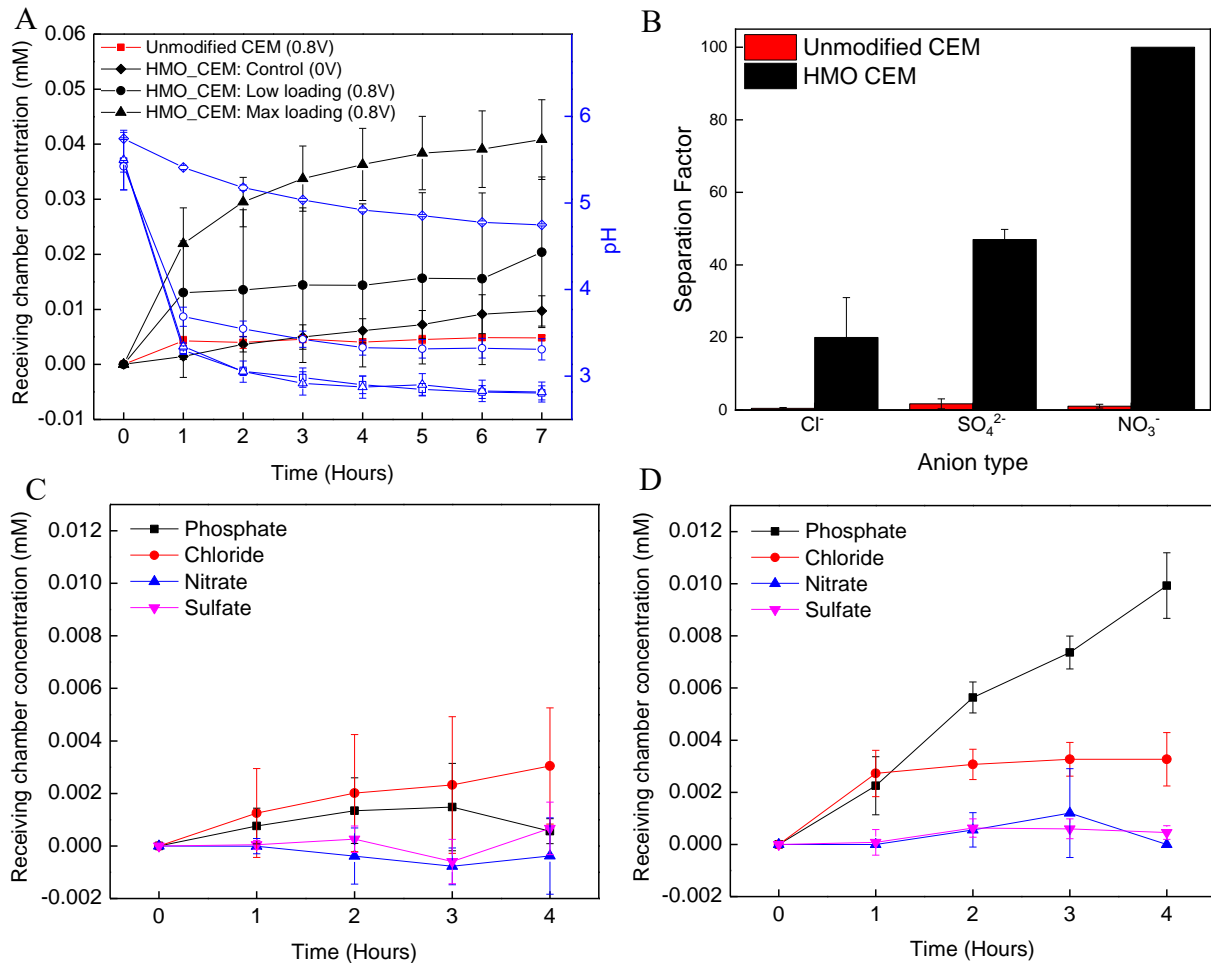
Figure 25: A) Phosphate concentration and pH in the receiving chamber for an unmodified CEM, high-loading HMO-CEM, and low-loading HMO-CEM in the presence and absence of an applied potential. The feed solution was composed of 0.1 M NaH_2PO_4, while 0.05M Na_2SO_4 was used as the receiving solution. A potential of 0.8 V vs. Ag/AgCl (2V cell potential) was applied across two Pt wires used as electrodes in the feed (cathode) and permeate (anode) chambers. (B) Phosphate selectivity over competing anions (Cl^-, SO_4^{2-}, and NO_3^-) for an unmodified and HMO-CEM. Phosphate concentration in the receiving chamber for the (C) unmodified CEM, and (D) HMO-CEM for an equimolar solution (1mM) of NaCl, Na_2SO_4, $NaNO_3$, and NaH_2PO_4 as the feed solution, and 18M☐ de-ionized water as the permeate; a potential of 0.8V Vs Ag/AgCl (2V cell potential) was applied across two Pt wires used as electrodes in the feed (cathode) and permeate (anode) chambers. Error bars represent standard deviations.

Phosphate Transport Rates

During experiments where an electrical field was used to provide the driving force, current measurements over the duration of the experiment can help elucidate the evolving conditions in the system (Figure 26A). For experiments involving HMO-CEM under electrodialysis conditions with Na_2SO_4 as the anolyte, the initial current was high (13.6 A/m^2), but declined over the duration of the experiment. This is likely because the pH in the anolyte dropped from 5.5 ± 0.3 to 2.8 ± 0.1, due to H^+ accumulation in the compartment, increasing the over-potential.[52,126] During the phosphate selectivity experiments, where the feed is composed of an equimolar mixture of anions, using DI water as the anolyte results in high electrical resistance in the anode chamber. Over time, as phosphate migrated towards the anode, the conductivity of the anolyte increased (from 2.2 to 5.8 μS/cm after 4 hours), increasing the current. However, it is not clear why the current was higher in the absence of competing ions (at low feed concentration, 1mM NaH_2PO_4, and DI water in the receiving compartment) while the phosphate transport rate in the presence of competing ions was higher (Figure 26A).

The maximum phosphate fluxes across the HMO-CEM under all experimental conditions are summarized in Figure 26B and the permeabilities, calculated using the equations derived by Kingsbury et. al.[254], for the 3 types of membranes under all experimental conditions, are reported

in table 4. Not surprisingly, the highest flux was observed under electrodialysis conditions where the catholyte was 0.1 M NaH_2PO_4 and anolyte was 0.05 M Na_2SO_4; in these conditions, the conductivity of the anolyte was high due to Na_2SO_4 and the phosphate concentration in the catholyte was highest, thus providing the largest driving force for phosphate transport. However, the flux under these experimental conditions (21.6E-8 mol/m^2/s) is only 2-3 times greater than fluxes measured under all other conditions, while the current was more than 10 times greater. Comparing the transport number of phosphate for the three membranes under similar experimental conditions, i.e., for a feed concentration of 0.1 M NaH_2PO_4, and receiving compartment concentration of 0.05 M Na_2SO_4 under electrodialysis conditions, the transport number is highest for the case of the high loading HMO-CEM (0.0054), and decreases with decrease in HMO loading (0.0018 for low loading HMO-CEM, and 0.0004 for the unmodified membrane). In all three cases however, the transport number is extremely low despite high current in the system, suggesting that majority of the current was transported by the proton and sodium ions in solution. Moreover, the low transport numbers for phosphate also indicate that under the conditions explored here, phosphate flux is limited by transport through the membrane, and not by the driving force.

This was further explored by looking at the current and HMO loading under three experimental conditions: electrodialysis of phosphate using an unmodified membrane, electrodialysis of phosphate using a low-loading HMO-CEM, and Donnan dialysis with a fully loaded HMO-CEM; the concentrations of phosphate and other supporting electrolytes were identical for all three configurations. While the electrical current using the unmodified membrane was the highest among these three (average current 4.1 A/m^2), this configuration exhibited the lowest phosphate flux (0.8E-8 mol/m^2/s). Phosphate flux measured during experiments conducted using the low-loading HMO-CEM were 2.6E-8 mol/m^2/s (average current 2.1 A/m^2), although the current in the

90

system was lower than that for the unmodified membrane (average current 4.1 A/m^2). Finally, the phosphate flux was highest (among the 3 experiments) under Donnan dialysis for a fully loaded HMO-CEM in the absence of current (5.1E-8 mol/m^2/s), implying that although a driving force is necessary, the flux of phosphate ions is limited by transport through the membrane.

Also, the data demonstrates that the presence of competing anions does not significantly impact phosphate transport rates, as evident by the similar phosphate flux under experiments conducted under similar conditions in the presence and absence of competing ions. While the HMO-CEM material exhibits very good selectivity towards phosphate, as evidenced by Figures 25C&D, the ion flux is low compared to the cation flux through the CEM, which was measured to be 5E-6 mol/m^2/s into the feed chamber for phosphate selectivity experiments, where the feed composed of equimolar concentrations (1 mM) of phosphate and other competing ions and DI water was used as permeate under an applied potential. Since the concentration gradient was in the direction opposite to the electric potential gradient, the Na$^+$ flux was positive into the permeate. For the case where feed was composed of 0.1 M NaH$_2$PO$_4$ and permeate was 0.05 M Na$_2$SO$_4$, under Donnan dialysis condition for an HMO-CEM, the Na$^+$ migrated into the feed with a flux of about 4.7E-5 mol/m^2/s. Therefore, more optimization work needs to be performed with the goal of increasing phosphate flux while maintaining the material's selectivity. Possible routes forward include the optimization of HMO loading, HMO NP size, and HMO NP surface properties.
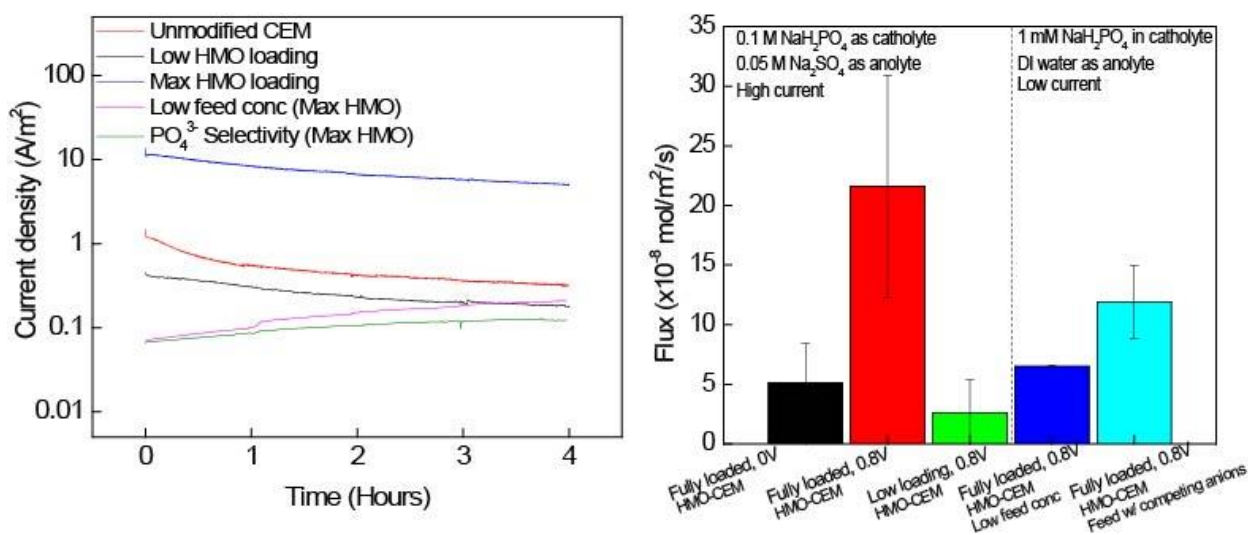
Figure 26: A) Current density for the 5 experimental conditions tested. B) The maximum phosphate flux across the HMO-CEM under various experimental conditions. All concentrations were normalized to concentration at time t= 1hour.

Table 4: Summary of permeability values for all experimental conditions

Experimental description	Permeability ($m^2 \cdot s^{-1}$)
Phosphate transport under Donnan dialysis; 0.1 M $NaH_2PO_4.H_2O$ as feed and 0.05 M Na_2SO_4/ DI water as receiving chamber solution. Membrane used: Fully loaded HMO-CEM (11.7% w/w)	$8.7 \pm 0.3 \times 10^{-14}$
Phosphate transport under Donnan dialysis; 0.1 M $NaH_2PO_4.H_2O$ as feed and 0.05 M Na_2SO_4 as receiving chamber solution. Membrane used: Low loading HMO-CEM (6.9% w/w)	$4.2 \pm 0.5 \times 10^{-14}$
Phosphate transport under Donnan dialysis; 0.1 M $NaH_2PO_4.H_2O$ as feed and 0.05 M Na_2SO_4 as receiving chamber solution.	$1.4 \pm 0.2 \times 10^{-14*}$

Membrane used: Unmodified CEM	
Phosphate transport under Donnan dialysis; 0.1 M $NaH_2PO_4.H_2O$ as feed and 0.05 M Na_2SO_4 as receiving chamber solution. Membrane used: AEM	$5.6 \pm 0.4 \times 10^{-11}$

* The permeability is determined from the change in concentration over time; however, all measurements are near the analytical method's detection limit, and hence, the flux of phosphate is likely effectively zero.

Phosphate Separation Factors

Testing selectivity under real–world wastewater concentrations

Phosphate selectivity under real-world wastewater concentrations was determined by calculating the separation factor under these conditions using a fully loaded HMO-CEM. Figure 27 shows the increase in ion concentrations in the receiving chamber with time. Owing to its high concentration in the feed (5X higher than that of phosphate), chloride concentration shows the most increase in the receiving chamber. However, despite having lower concentration, phosphate is competitively transported across the HMO-CEM with much higher separation factors compared to other ions. For these experiments, the membrane separation factor was calculated to be 10.8 ± 5.3 for chloride, 14.6 ± 2.5 for nitrate, and 72 ± 57 for sulfate ions. The separation factor of chloride at an initial concentration 5X higher than phosphate is only half its value when the initial chloride and phosphate concentration were equal, thus showing exceptional performance. Meanwhile, the separation factor of nitrate and sulfate have reduced significantly (or has high standard deviations), possibly due to low concentrations near the detection limit of the IC.
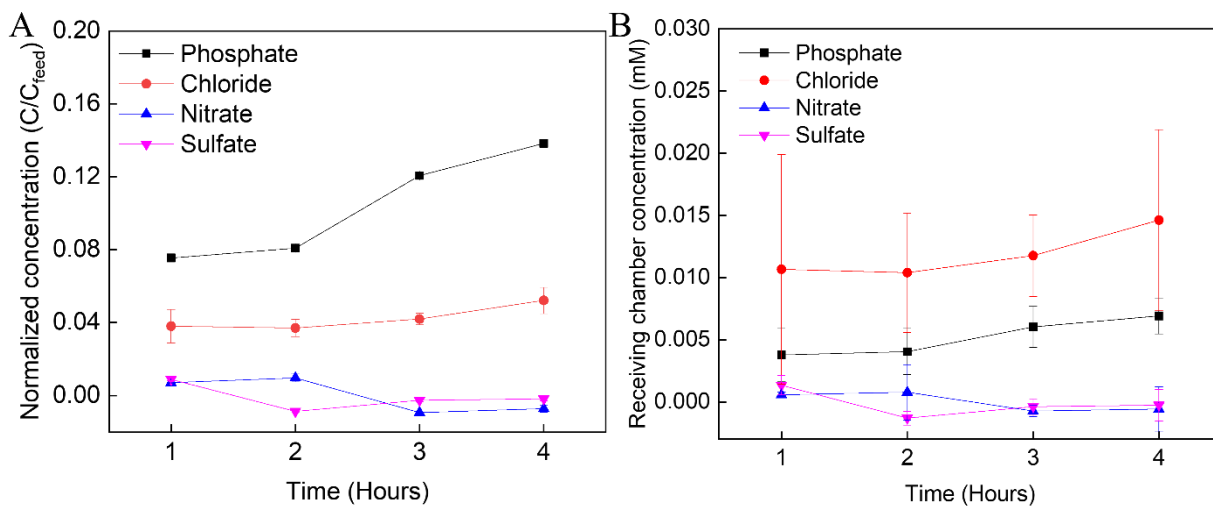
Figure 27: A) Receiving chamber concentrations of all anions normalized to their initial feed concentrations with feed composed of real-world concentrations of chloride, sulfate, nitrate, and phosphate (B) Absolute receiving chamber concentrations of the competitive anions.

When exposed to high pH conditions during preparation, the membrane did not show a decline in performance. Therefore, we anticipate that under the relatively mild conditions existing in municipal wastewater streams, the membranes will remain stable. However, long-term performance tests are needed to confirm this.

Donnan dialysis of phosphate

Donnan dialysis with DI water in the receiving chamber

Figure 28A depicts the phosphate increase in the receiving chamber for the Donnan dialysis experiment conducted with DI water in the receiving chamber (instead of 0.05 M Na_2SO_4 solution). Similar to the Donnan dialysis experiments with Na_2SO_4 as the receiving chamber solution, the pH decline in the receiving chamber was not as significant compared to the pH under electro-dialysis conditions. As a result, the rate of phosphate transport was also constant throughout the experiment, with a flux of $4.3 \pm 1.5 \times 10^{-8}$ $mol \cdot m^{-2} \cdot s^{-1}$. This flux is statistically

94

identical to that observed during the Donnan dialysis experiment when using 0.05 M Na_2SO_4 as the receiving chamber solution ($5.1 \pm 2.5 \times 10^{-8}$ $mol \cdot m^{-2} \cdot s^{-1}$).

Transport across a non-equilibrated membrane

Figure 28B shows the increase in phosphate concentration in the receiving chamber when using a membrane not pre-equilibrated in 0.5 M $NaH_2PO_4 \cdot H_2O$ solution. Figure 28B also shows that the slope of the phosphate concentration vs. time graph decreases progressively. The lower flux of phosphate across the membrane ($\sim 2.3 \times 10^{-8}$ $mol \cdot m^{-2} \cdot s^{-1}$), compared to that of a pre-equilibrated membrane under the same driving force (4.3×10^{-8} $mol \cdot m^{-2} \cdot s^{-1}$), can be attributed to insufficient phosphate at the exchange sites, leading to further depletion as phosphate is transported to the receiving chamber.
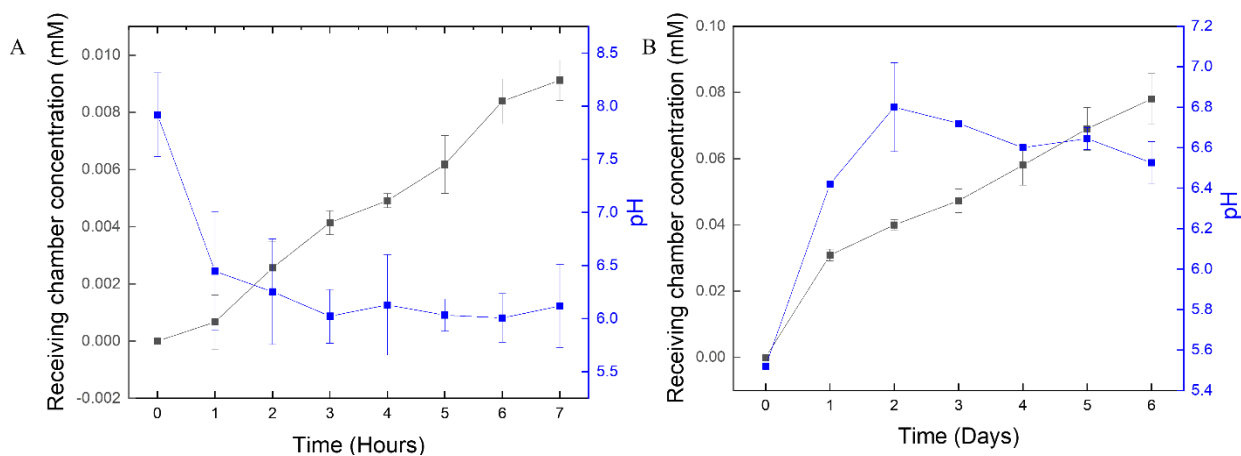
Figure 28: A) pH drop and phosphate concentration increase in the receiving chamber for Donnan dialysis with DI water in the receiving chamber. (B) pH change and increase in phosphate concentration in the receiving chamber in experiments testing phosphate transport without membrane pre-equilibration in 0.5 M NaH_2PO_4.

Donnan dialysis of low loading HMO-CEM and an unmodified CEM

Figure 29A and 29B depict the pH change and phosphate increase in the receiving chamber for Donnan dialysis experiments (0.1 M NaH_2PO_4 as feed and 0.05 M Na_2SO_4 solution in the receiving

chamber) for the low loading HMO-CEM and unmodified CEM, respectively. The rate of phosphate transport was constant throughout the experiment, with a flux of $1.6 \pm 0.01 \times 10^{-8}$ mol·m^{-2}·s^{-1} for a low loading HMO-CEM, while for an unmodified CEM the flux was measured to be $7.5 \pm 5.5 \times 10^{-10}$ mol·m^{-2}·s^{-1}. However, since the phosphate concentration values measured in the unmodified CEM experiments were close to the detection limit of the instrument, the calculated flux is not reliable, and likely represents an over estimation.
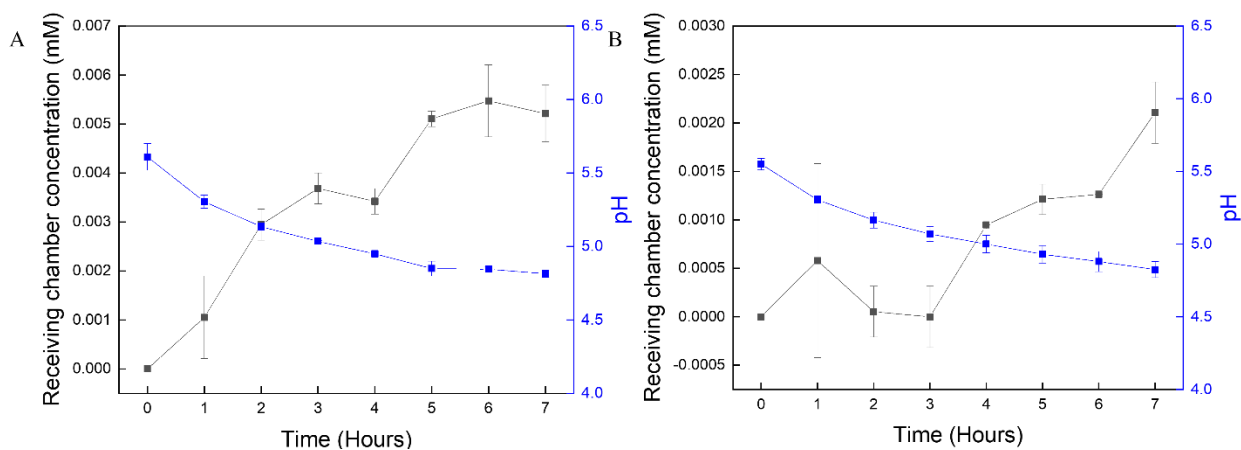
Figure 29: A) pH drop and phosphate concentration increase in the receiving chamber for Donnan dialysis with low loading HMO-CEM. (B) pH change and increase in phosphate concentration in the receiving chamber in Donnan dialysis experiments using unmodified CEM.

Mechanism of Phosphate Removal

We used XPS and FTIR (Figure 30 & 31, respectively) to probe the interactions of phosphate ions with the various membrane components, as well as surface charge analysis to understand the impact of adding HMO to the CEM matrix on the overall surface charge of the material.

XPS measurements

XPS analysis was conducted on the unmodified CEM, pristine HMO-CEM, and HMO-CEM after it was immersed in a phosphate solution and dried. All peak positions are referenced to the C 1s peak of adventitious carbon at 284.5 eV. The binding energy measured by XPS is highly sensitive

to the chemical environment of the element. Therefore, an atom interacting with another chemical species leads to a change in the binding energy of the core electron, which is represented by a binding energy shift. A broad-spectrum scan of the HMO-CEM shows the presence of sodium, manganese, carbon, sulfur, and oxygen (Figure 30 A). After immersing the material in a phosphate solution (followed by rinsing with copious amounts of DI water), a peak associated with phosphorous emerged in the spectrum (Figure 30 A). XPS analysis of the unmodified membrane and HMO-CEM (before and after immersion in a phosphate solution) was carried out in the binding energy regions of the Mn2p, Na1s, C1s, O1s, and P2p orbitals. The peaks of Na1s (1071.80 eV), Mn2p (642.8 eV), O1s (531.80 eV), and C1s (284.8 eV) were detected from an HMO-CEM immersed in DI water. The O1s peaks of the unmodified and the two HMO-CEMs were deconvoluted to discern the speciation of O within the membranes. For the unmodified membrane, the O peak was composed of a background O peak (532.76 eV) and H_2O (534.35 eV), whereas for the HMO-CEM immersed in DI water, three peaks corresponding with background O (531.83 eV), O^{2-} (533.58 eV), and H_2O (534.98 eV) emerged; the O peak associated with O^{2-} correspond to the oxygen in MnO_2, further evidenced by the Mn peak deconvolution as MnO_2 (641.62 eV and 645.91 eV).

After immersing the membrane in a phosphate solution, the O peaks shifted to background O (530.58 eV), O^{2-} (532.63 eV), and H_2O (534.53 eV) (Figure 30 B). Further, the Mn $2p_{3/2}$ peak in the HMO-CEM material located at 641.62 eV, shifted to 641.24 after phosphate adsorption (Figure 30 C), and a new peak associated with phosphorous (P2p) emerged at a binding energy of 129.24 eV corresponding to (NaH_2PO_4)[255] (Figure 30 D).[256] The emergence of this peak indicates the successful uptake of phosphate by the HMO-CEM.
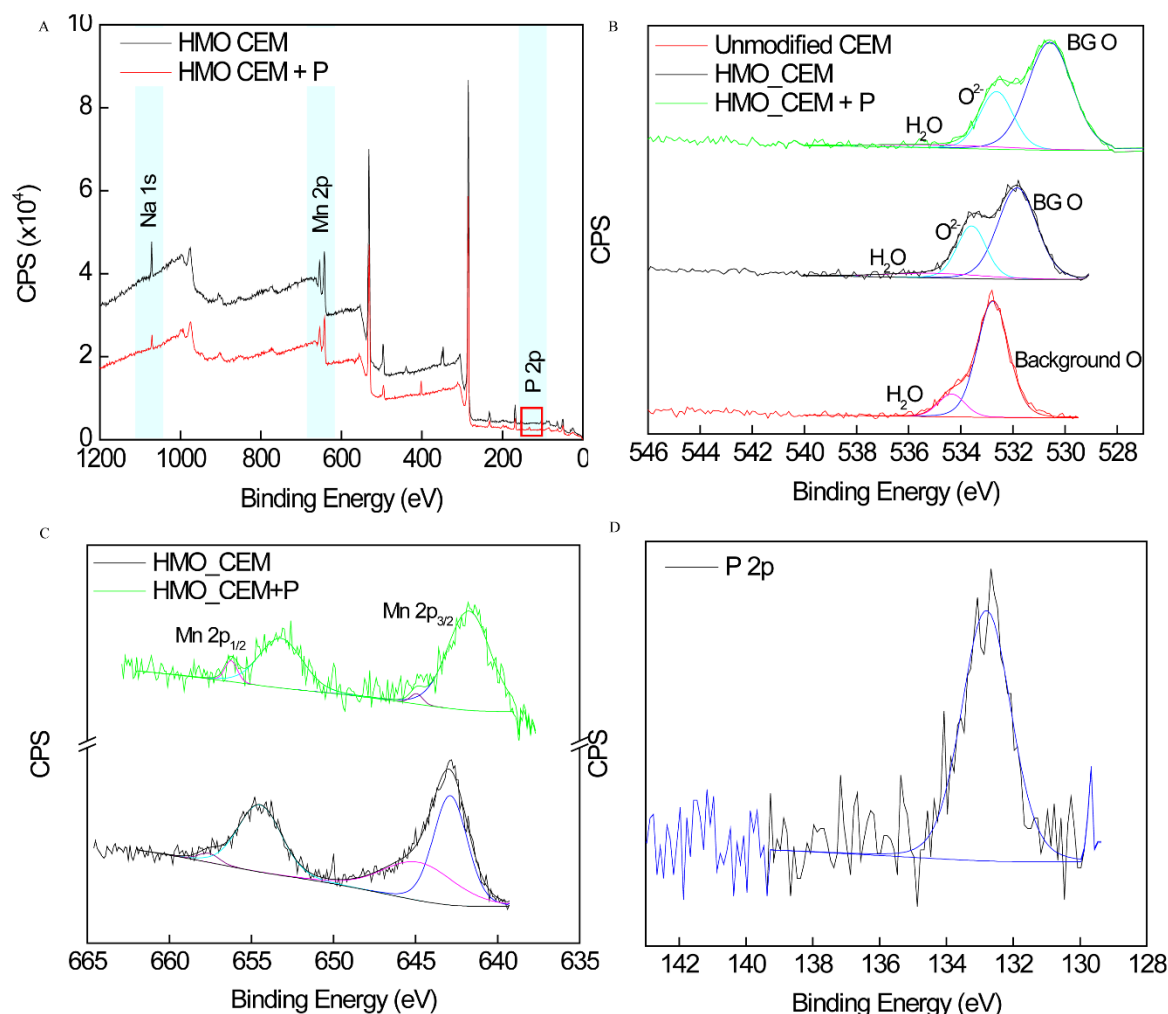
Figure 30: XPS spectra for HMO-CEM and HMO-CEM immersed in 0.5 M $NaH_2PO_4.H_2O$ for 24 hours and rinsed with DI water and dried in oven at 50 ℃ for 24 hours; (A) shows the wide scan XPS spectra for the two samples, and high resolution (B) O1s peak for an unmodified, pristine HMO-CEM, and phosphate embedded HMO-CEM (C) Mn2p for the pristine HMO-CEM, and phosphate embedded HMO-CEM, and (D) high resolution P2p for the HMO-CEM+P membrane.

FTIR Spectra

FTIR spectroscopy was used to study the interaction of phosphate with HMO NPs embedded in the HMO-CEM. An inner-sphere interaction between phosphate and HMO would be evident in the FTIR spectra as a peak centered at 1053 cm^{-1}, which corresponds to the v_3 band vibration of HPO_4^{2-} or $H_2PO_4^-$.[256–258] However, when the HMO NPs and HMO-CEM were exposed to a phosphate solution, no such peak was observed in their FTIR spectrum (Figure 31). The absence

98

of this peak potentially points to an outer-sphere complex formation between the Mn-P species.[208,210,246]
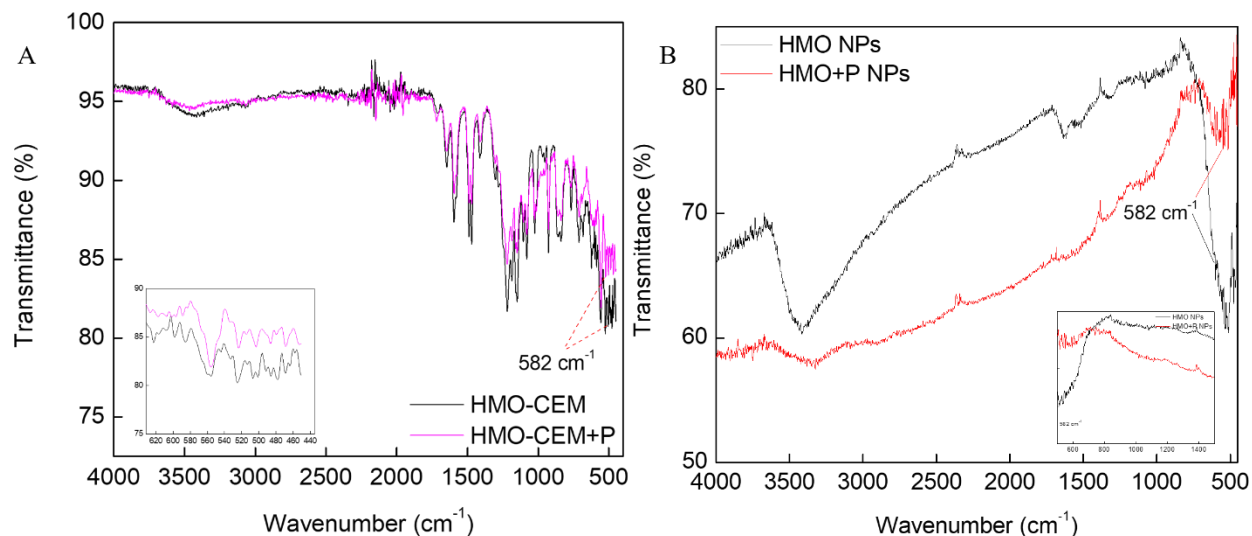
Figure 31: FTIR spectra for (A) the HMO-CEM and HMO-CEM immersed in 0.5 M NaH$_2$PO$_4$.H$_2$O for 24 hours, rinsed with DI water and dried in oven at 50 ºC for 24 hours (HMO-CEM+P); FTIR absorption spectra from 450-630 cm^{-1} (inset). (B) FTIR spectra for HMO NPs, and HMO NPs immersed in 0.5 M NaH$_2$PO$_4$.H$_2$O for 24 hours and rinsed with DI water and dried in oven at 50 ºC for 24 hours (HMO +P NPs); (inset) FTIR spectra from 500-1500 cm^{-1} with no observable Mn-P peak, suggesting an outer sphere interaction between the HMO NPs and phosphate.

Molecular Dynamics Simulation

To understand the interactions and transport of the ions through the HMO-CEM membrane on the molecular level, we carried out molecular dynamics simulations of H$_2$PO$_4^-$ and Na$^+$ ions in configurations that resemble the gel and intergel phases of the HMO-CEM (section 2.2 in supplementary text). The all-atoms simulation protocol imposes a severe restriction on the size of the simulation cell. Consequently, the size of the embedded HMO particle and pore are scaled down compared to the experimental conditions. Specifically, the diameter of the simulated HMO particle is 10 nm, and the ions can explore the micro- and mesopore spaces of the HMO-CEM composite membrane. In our model, we constrained the size of the HMO particle to 10nm to

99

minimize the computational load. However, we do not anticipate that the nature of phosphate-HMO interaction is impacted by the particle size, although we have not verified this. The impact of nanoparticle size is beyond the scope of this paper and is a topic for future studies. The system size is still sufficient to reveal the modes of interactions/complexation by polymer and particle and the molecular mechanism of phosphate transport through the HMO-CEM membrane. In Figure 32A-B, we show molecular snapshots of the HMO-CEM system and the molecular model of the model ion exchange polymer molecule.

The values of the diffusion coefficients of the $H_2PO_4^-$ and Na^+ ions obtained from the molecular dynamics trajectories are listed in Table 1 (averages over 10 independent simulation runs), where each simulation started from a slightly different initial configuration. The diffusion coefficients for the ions in the aqueous solution are representative of the intergel solution phase, whereas those along the HMO-CEM are representative of the gel phase. As can be seen, the calculated ion diffusivities in the gel phase are approximately three ($H_2PO_4^-$) and two (Na^+) times lower than their diffusivities inside the intergel solution phase. The presence of the HMO particle increases the mobility of phosphate by about 20%, but has a negligible effect on the mobility of sodium, whose mobility drops by 8% (Table 1). The electric field accelerates the ionic mobility within the gel phase of HMO-CEM by 21% and 27% for phosphate and sodium ions, respectively.

The ions have the lowest mobility in the system composed of electrolyte solution in contact with the HMO particle (Table 1). Both sodium and phosphate adsorb at the HMO particle surface, forming outer-sphere complexes (Figure 32D). The presence of the negatively charged polymeric matrix accelerates ion transport due to disruption of the weak electrical double layer formed around the HMO particle. Because the negatively charged polymeric matrix attracts Na^+ and repels $H_2PO_4^-$ ions, the Na^+ ions are pulled away from the HMO vicinity, and $H_2PO_4^-$ ions are pushed away from

the polymer. Critically, $H_2PO_4^-$ ion interaction with the particle weakens due to the depletion of Na^+ ions around the HMO particle, and electrostatic attraction between $H_2PO_4^-$ and Na^+ ions accumulated near negatively charged groups in the ion exchange polymer. As a result, the mobility of $H_2PO_4^-$ increases nonlinearly in the gel phase of HMO-CEM compared to the cases of CEM or HMO-only systems (Table 1). This nonlinearity is due to the complexity of the ion pathways across the HMO-CEM matrix. First, ion fluxes through the micro and mesopores differ due to the variation in the solvent properties, different proximity of the polymer chains and particle surfaces, and pore-size-dependent permeability. Second, an ion's ability to diffuse against the field or in the direction perpendicular to the field decreases with increasing voltage. As the strength of the field increases, the thermal motion of ions diminishes, and the translation along the field lines dominates their dynamics. If the ion reaches the HMO surface, it can diffuse around it as an outer-sphere complex. However, if the ion becomes trapped in the dense polymer pocket with no exit channel, it will not escape by diffusing against the electric field lines. The voltage-dependent diffusivities (Figure 32C) capture this phenomenon, showing subtle deviation from the expected exponential dependence. While the diffusivities of the individual phosphate ions vary in any given simulation, the simulation shows that the slowest ions are moving through the polymeric channels while the fastest move through the intergel solution phase or near the HMO particles. The molecular dynamics simulations provide a molecular-level understanding of phosphate transport through the HMO-CEM membrane. Simulations confirm experimental observations (section 2.2 in supplementary text) that $H_2PO_4^-$ ions are forming only outer-sphere complexes with HMO, enabling their uptake onto the HMO-CEM material, and facilitating their diffusion across the membrane. This transport is driven by an electric field or concentration gradient across the

membrane. The simulations also confirm that phosphate mobility is much higher in the HMO-CEM compared to the pure CEM.
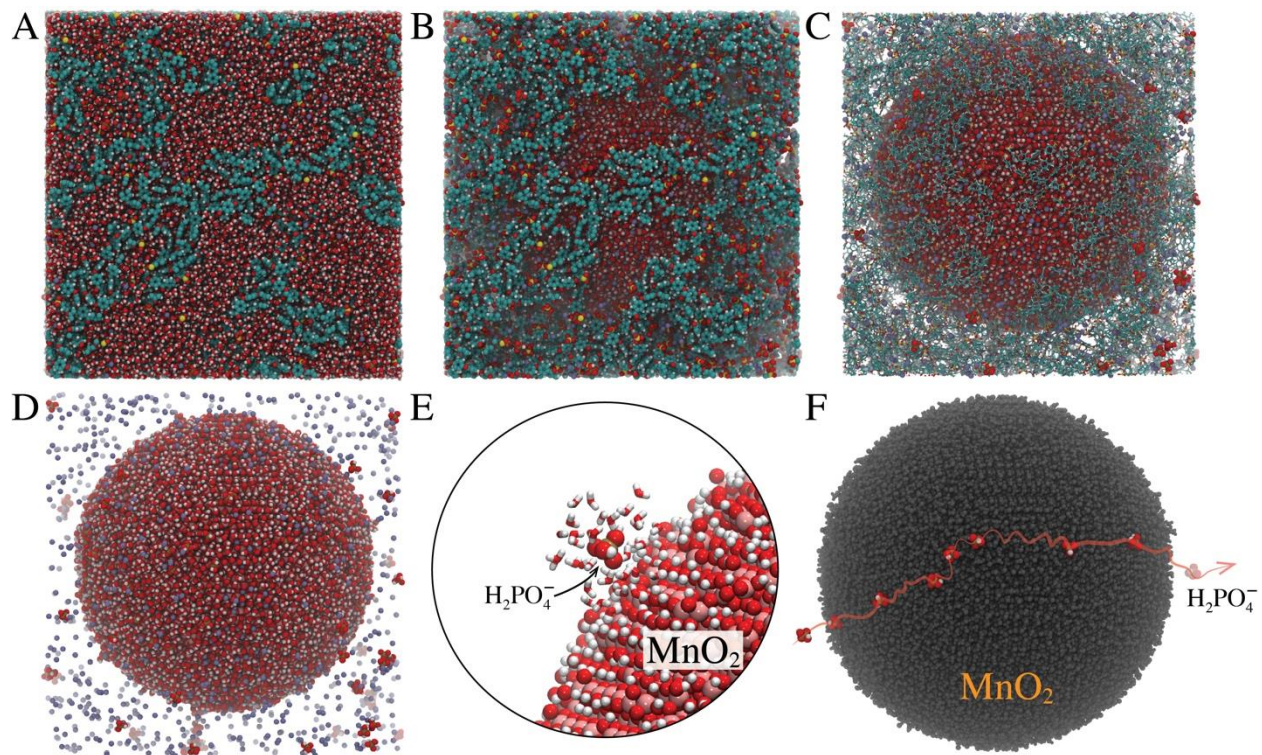
Figure 32: Example of the simulation cell used in the molecular dynamics simulations: A) all atoms shown as vdw-spheres, B) water molecules are hiden, C) water moelcules hidden and polymer represented by the ball-and-stick model, D) only HMO particlesa and ions are shown, E) example of the H2PO4- ion with its hydration water in the outer-sphere complex geometry, F) illustration of the diffusion pathway of adsorbed $H_2PO_4^-$.

Phosphate Transport Model

Using our experimental observations, a model describing ion transport across the HMO-CEM was developed based on the microheterogeneous model for ion exchange membranes (section 2.1 in supplementary text).[73,233] The model was used to predict the flux and transport number for phosphate, and was then used to estimate the HMO loading needed to increase phosphate transport across the membrane. Phosphate flux and transport number were calculated using equations 9- 25 using the parameters given in Table 2, with the concentration profile for the ions throughout the

membrane given by equation eq. 26. The parameter, n, in equation 26, and the structural parameter, α, in equations 11 & 22, were treated as adjustable parameters and fit to the model. The value of n (Eq. 26) defines the concentration profile across the membrane thickness; an $n = 1$ value corresponds to a linear concentration profile, with increasing n values corresponding to a more rapid, exponential decline (Figure 21).[237] The value of α can vary from –1 to 1, and represent the connectivity of the gel and intergel phases (α) in the microhetergoneous model, with $\alpha = -1$ referring to their respective phases connected in a series, while $\alpha = 1$ refers to a parallel connection.[73] We obtained the lowest root mean square error values for the transport number and flux of the unmodified and low-loading HMO-CEM with $n = 10$, $\alpha = 0.3$, compared to our experimentally-determined values (Table 3); the predicted vs. observed phosphate flux values can be seen in Figure 33A. Although the flux predictions for the unmodified and low-loading HMO-CEM are within 30% of the experimental results, the predicted flux for the high-loading HMO-CEM, using these n and α values, is almost 2 times lower than the experimental flux (data not shown). However, since hydration of a polymeric membrane leads to the formation of micro and meso-pores, which swell strongly as water intercalates between the polymeric chains within the membrane,[259] it is possible that the modification of the membrane by the *in situ* growth of HMO NPs affects the internal membrane structure and changes the α parameter, and by extension, the concentration profile of co-ions within the membrane (the n-parameter). By adjusting the parameters n and α to 5 and 0.7, respectively, the predicted flux had an error of about 11% (Figure 33A). Physically, n = 5 implies that the concentration decline of the phosphate anion across the high-loading HMO-CEM is more gradual compared to that of an unmodified membrane (Figure 33A). This implies that the high concentration of ion-exchange groups in an unmodified membrane limit the presence of co-ions within the membrane, which are thus present primarily near the

feed/membrane interface leading to an exponential decline across the membrane thickness (i.e., higher n values). In contrast, in the HMO-CEM, due to phosphate's ability to form outer-sphere complexes with HMO NPs (section 2.6 in SI), phosphate concentrations throughout the material are higher resulting in a linear decline in concentration as one moves away from the membrane/feed interface. Similarly, introduction of a large quantity of HMO NPs alters the internal structure of the membrane; an increased value of α ($\alpha = 0.7$) represents a more parallel orientation of the gel and intergel phases in relation to the transport axis (perpendicular to the membrane surface) as compared to that of an unmodified membrane.

The ion transport numbers predicted by the model were compared to those obtained from the experiments in Figure 33B. Transport numbers describe the fraction of current carried by a particular ion species relative to the overall current passing through the system (eq. S23). For the case of phosphate transport across unmodified and modified CEMs, the model predicts that the addition of HMO to the CEM matric increases the fraction of current carried by phosphate. Moreover, it also accurately calculates transport numbers for the unmodified and low loading HMO-CEM. Thus, for these membranes, our simplifying assumption that accounts for sodium and proton transport during the experiments (see eq. S23 and S24) is valid. However, the model under-predicts the transport number for the high loading HMO-CEM by ~30%, thus indicating that at higher HMO loadings the simplifying assumption fails to appropriately account of fraction of phosphate transport and thus its transport number.

The model predicts a higher gel-phase diffusion coefficient for anions over cations, by nearly two orders of magnitude (Table 7). This could be attributed to the electrostatic attraction between cations and the polymeric fixed charges, which the anions/co-ions do not experience.[260] While this may seem counter-intuitive (since the flux of cations is much higher than that of anions), the higher

flux can be explained by Donnan exclusion, which causes counter ions to partition into the membrane at a higher rate than co-ions, resulting in higher counter ion concentrations within the membrane. Thus, cations are transported across by interaction with the fixed charges in the gel phase of the membrane, while the anions are transported through the electroneutral solution present in the intergel phase and the cation and anion transport are correlated (coupled) to maintain charge-neutrality of the fluid phase. In the HMO phase, the diffusion coefficient of phosphate is higher than that of cations. Importantly, the specific interactions of phosphate ions with the HMO particles enables their partitioning into and diffusion across the HMO-CEM, resulting in a higher diffusion coefficient for the phosphate anions. As a result, phosphate is transported across the membrane through the intergel phase by 'hopping' along the HMO NPs.

Finally, the model was used to estimate the HMO loading that would yield a phosphate flux comparable to phosphate flux through an anion exchange membrane. Increasing the HMO loading of a CEM affects its properties including water uptake, ion exchange capacity, the diffusion coefficient of salt through the membrane, and the volume fraction occupied by the NPs within the membrane. However, since most of these values were obtained from experiments and used as inputs into the model, extrapolating the model to accurately predict phosphate flux at higher HMO loading is riven with uncertainty. During the formation of HMO NPs within the CEM (according to the reactions listed in 1.2), Na^+ displaces the Mn on the charged fixed sites, forming the eventual HMO particles in the vicinity of the gel phase, which could possibly explain the decrease in ion exchange capacity with increase in the HMO loading (Table 2). Assuming that the ion exchange capacity decreases and f_{int} (volume fraction of intergel phase in the membrane) increases linearly with f_p (volume fraction of particles within the membrane), we can estimate that for $f_p = 0.07$, the flux of phosphate would increase to 1.04×10^{-5} mol·m^{-2}·s^{-1}, comparable to the cation flux through

CEM and anion flux through an anion exchange membrane.[261–263] It is also possible that NP size could affect the performance of HMO-CEM. We speculate that a decrease in NP size would lead to decrease in the ion exchange capacity since the smaller sized NPs would block the fixed charges and decrease their charge exclusion effect on the co-ion. However, our model does not account for NP size and the experimental work is beyond the scope of this study.
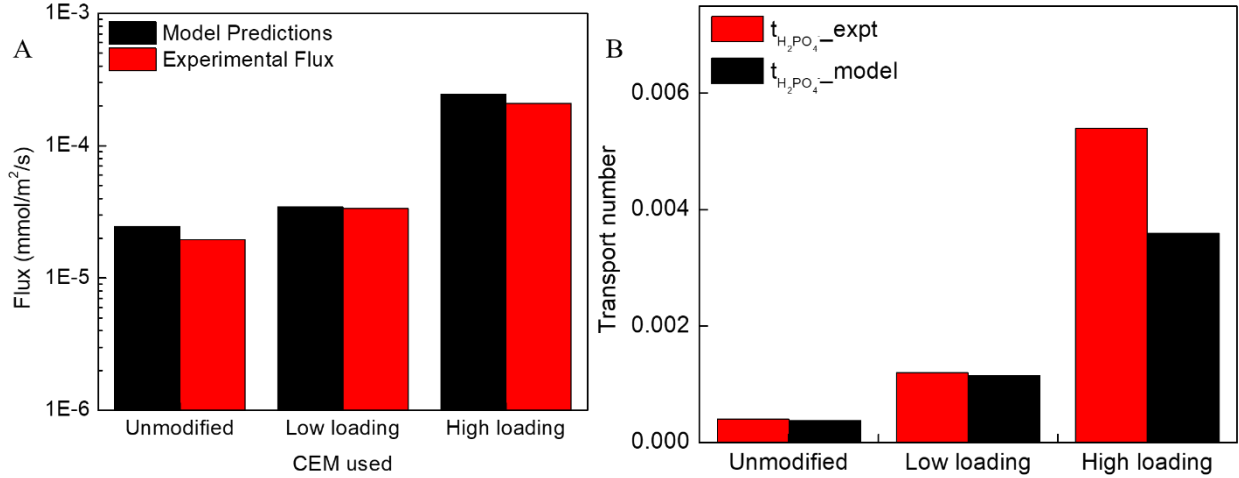
Figure 33: Comparing experimental values and model predictions for A) phosphate flux and B) phosphate transport number.

Table 5: Results from the microheterogenous model

| | C_{co}^{g} | C_{ct}^{g} | D_{co}^{g} [m²/s] | D_{ct}^{g} [m²/s] | D_{co}^{HMO} | D_{ct}^{HMO} | $t_{H_2PO_4^-}$ |
	[mM]	[M]			[m²/s]	[m²/s]	
Unmodified	0.24	4.49	3.00×10^{-9}	2.65×10^{-11}	--	--	0.0004
Low-loading	0.35	3.07	3.01×10^{-9}	3.87×10^{-11}	5.85×10^{-9}	5.89×10^{-9}	0.0012
High-loading	0.62	2.91	3.03×10^{-9}	4.06×10^{-11}	5.82×10^{-9}	5.84×10^{-9}	0.0036

3.6. Feasibility of the process

The HMO-CEM provides superior phosphate selectivity, albeit at a lower flux (comparing Figures 25A&C and 18). In our study we have found that phosphate flux can be improved by providing a

greater driving force (applying a higher voltage), or by increasing the HMO loading of the membrane. However, the higher electrical driving force will lead to higher energy consumption. Based on our experimental data, we determined that the energy required to drive phosphate across the HMO-CEM (0.02 $Kg-PO_4/KWh$) was approximately two orders of magnitude higher than through a standard AEM (5.2 $Kg-PO_4/KWh$). However, this comparison is misleading as the commercial AEM offers little selectivity towards phosphate (with a phosphate separation factor of 5, 1.5, and 1 over sulfate, nitrate, and chloride, respectively, Figure 25B). Based on our modeling effort, we determined that increasing the mass loading of the HMO particles to 35% would increase the phosphate flux to that of a commercial AEM, which would reduce the energy associated with phosphate recovery by two orders of magnitude.

For our low loading and high loading HMO-CEM, the volume fractions of 0.013 and 0.024, respectively, correspond to a mass loading of 6.9 and 11.7% (wt. of MnO_2/wt. of membrane), respectively. An HMO-CEM with 35% HMO NP loading is nearly three times the loading of the highest loading membrane tested in our experiments. Tensile strength analysis of manganese oxide/cellulose membranes by Tang et. al.[264], at 50% mass loading, showed that although the tensile strength of the composite reduced by 44%, the mechanical strength was still appreciably high (~14.2 MPa). For ion exchange membranes, analysis of mixed matrix membranes (nanoparticle/polymer composite) synthesized by Sunarso et. al.[265] showed that at a mass loading of 50%, the membrane exhibited improved proton conductivity and mechanical strength. Another study by Ounissi et. al. shows little change, or in some cases an improvement, in membrane transport properties at nanoparticle loadings of up to 50.5%.[203] Therefore, the needed mass loading (35%) is not expected to damage the physical properties of the HMO-CEM membrane, and is well within the range of previously demonstrated nanoparticle loading range.

Comparing the cost of the phosphate extraction process using an HMO-CEM with conventional processes, such as struvite precipitation, helps us further elucidate the viability of our process. At $0.06/KWh, phosphate recovery using an HMO-CEM is ~$3/Kg-PO$_4$, which is currently an order of magnitude higher than that of struvite precipitation ($0.25/ Kg-struvite).[266] However, increasing the mass loading of HMO nanoparticles in the membrane is expected to result in an increase in phosphate flux by two orders of magnitude, thereby dramatically reducing the cost of phosphate production.

Future work will focus on optimizing the loading of the HMO particles to maximize both phosphate flux and selectivity. Importantly, membrane selectivity is dependent on the charge density and ion exchange capacity of the parent polymer. As can be seen from Table 2, increasing the HMO loading decreases the ion exchange capacity of the membrane, and therefore, higher loadings could possibly lead to a decrease in selectivity when the NP loading decreases ion exchange capacity enough to mitigate the Donnan exclusion effect. Therefore, a careful balance must be identified – what is the HMO loading that maximizes both flux and selectivity.

The prepared membranes could then be employed in real systems to recover phosphate from wastewater. Our experiments show that the HMO-CEM could potentially be used in an electrodialysis system, with little to no change in the operating conditions. In wastewater treatment plants, we propose the membrane be used in the treatment train after aerobic treatment and clarifier (when wastewater has high residual phosphate concentration). The setup would require an additional membrane after the AEM in an electrodialysis setup for the case where desalination can be achieved along with phosphate sequestration. The receiving chamber solution, in this case, would be a phosphate solution so that the process is not current limited (as in Figure 34). The

membrane could also be used as a single membrane in a similar setup as our experiments (Figure 17), separating feed and receiving solution.
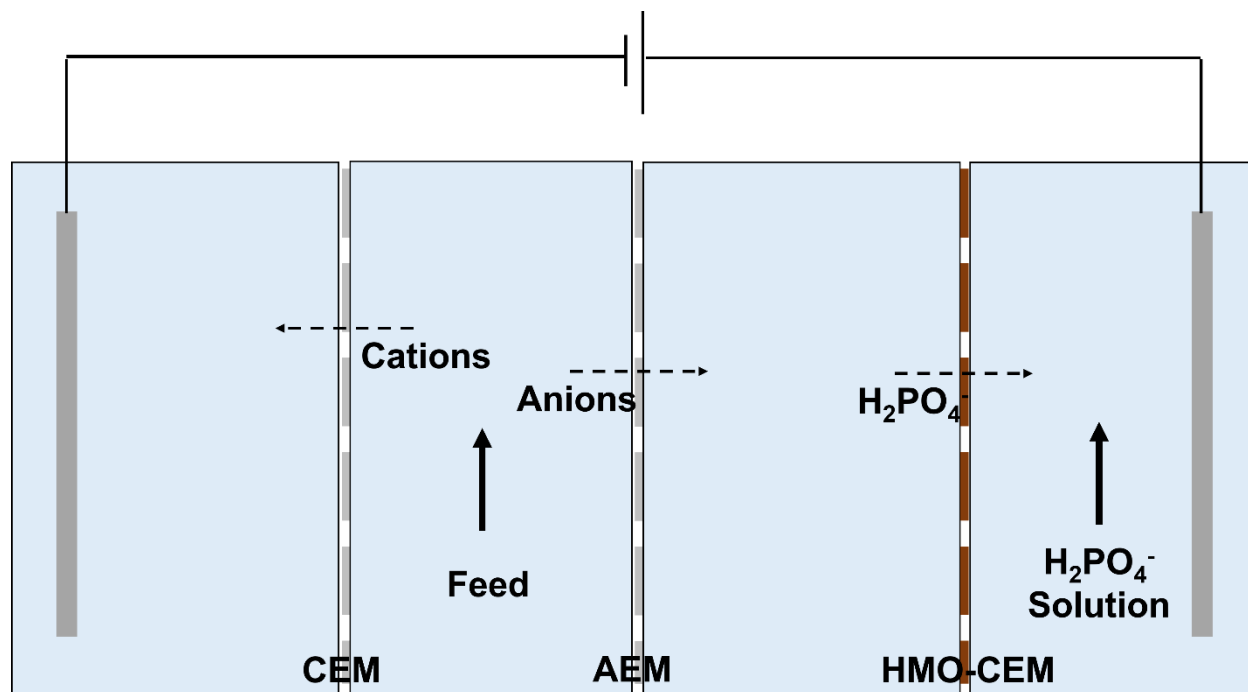
Figure 34: Proposed schematic of experimental setup in real ED system.

3.7. Conclusions

In this study, we successfully synthesized, characterized, and tested a new class of membranes that allow for selective transport of phosphate across a cation exchange membrane. Selective separation is achieved by exploiting the outer-sphere complexation reaction between phosphate and the embedded HMO NPs within the membrane. This technique paves the way towards a novel approach to specific ion recovery, which utilizes similar complexation interactions between the target ions and the embedded extractant groups in ion exchange membranes, while the fixed charges prevent passage of competing co-ions. Other ionic species such as lithium, uranium, gold, and metals that exist as oxy-anions (including arsenic, vanadium, and hexavalent chromium) could possibly be extracted by employing appropriate NPs that complex with the target ion. Thus, these

membranes demonstrate an innovative technology desirable from the perspective of both water quality (due to toxicity) and resource recovery.

Chapter 4:

Summary, Conclusions, & Future Work

The overarching goal of this research was to investigate the role of intermolecular interactions and interfacial science in developing membranes for nutrient recovery. To this end, the role of adding an electrically conducting layer over a hydrophobic membrane to facilitate interfacial reactions was explored and the effect of adding a metal layer to improve surface electrical conductivity was also studied. This research also studied the possibility of selective ion recovery by leveraging intermolecular interactions of the target ion with specific carriers embedded within the membrane.

In chapter 1, we briefly discuss the water stress and resource scarcity issues faced by the world at large and the need for water treatment and removal for nutrients that damage the water ecosystem. We then make a case for the need to recover these nutrients from wastewater, instead of merely removing them, to close the nutrient cycle, and explored the use of membrane technology for this purpose. For background, we delve into the two predominant membrane technologies relevant to the research here- membrane contactors, to recover dissolved gases from wastewater solutions, and ion-exchange and facilitated transport membranes, to understand ion transport through such membranes and possibility of selective ion recovery. Furthermore, we also describe the various intermolecular interactions that exist in nature and narrow them down to those relevant in our research affecting ion transport. Finally, we discuss application of carbon nanotubes (CNTs), their advantages, and their role in making electroactive membranes.

In chapter 2, we developed an electrically conducting hydrophobic membrane to recover nitrogen as ammonia from wastewater. The objective of this study was to study dependence of ammonia recovery on membrane conductivity and pore morphology. We developed three types of electroactive membranes, a polymeric membrane coated with CNT, a second membrane with Ni deposited electrochemically over the CNT layer (over a period of 6 hours), and a third membrane with Ni deposited over 24 hours. These membranes were used as cathodes in an electrochemical

cell, separated from the anode by a cation exchange membrane (CEM). Electrical potential was applied to the membrane surface to facilitate hydrogen evolution reaction and generate hydroxide ions (OH^-). The three membranes characterized using scanning electron microscopy, atomic force microscopy, gas permeability, contact angle measurement, and cyclic voltammetry showed highest gas permeability for the CNT membrane and lowest for the 24-hour Ni membrane. The 6-hour Nickel membrane demonstrated the best performance, evaluated using ammonia recovery rate and energy consumption parameters. Ammonia recovery achieved by circulating an acid solution on the receiving side of the membrane showed superior recovery rates compared to vacuum. Finally, the ammonia recovery experiments, using an acid solution, demonstrated a reduction in energy consumption by 50% compared to conventional ammonia removal processes. The findings from this project were published in *Environmental Science: Nano* in 2020.

The use of CNTs to improve removal of contaminants and facilitate surface reactions has previously been demonstrated to be successful; however, CNTs are plagued with problems such as nonuniform current distribution which can be addressed by growing a layer of Nickel over the CNTs to improve current conduction while also imparting the membrane with catalytic properties. Addition of the metal layer affects the pore size and surface roughness of the membranes; therefore, future research would need to explore further the effects of growing metals on polymeric membranes in terms of membrane performance.

Overall, the results in chapter 2 demonstrate the advantages of using electroactive membranes for ammonia recovery. Such electrically conductive membranes could be used for other applications, such as recovery of volatile fatty acids from wastewater, or hydrogen gas produced during hydrogen evolution.

In chapter 3, we developed a novel membrane that allows for highly selective phosphate transport (an anion) through a cation exchange membrane (CEM). The objective of this study was to investigate the possibility of phosphate recovery as the phosphate ion ($H_2PO_4^-$/PO_4^{3-}), as opposed to a precipitated mixed salt (e.g., struvite, $NH_4MgPO_4.H_2O$). Most membrane-based separation processes rely on either one of two mechanisms- size based or charge based separation, however, facilitated transport membranes allow for transport of target species through a combination of solution-diffusion and complexation reaction, where the complexation reaction provides an additional mechanism for transport of selective molecules. Selective transport was achieved by modifying commercial cation exchange membranes with nanoparticles to leverage specific interaction between the embedded nanoparticle and the target ion that allows for its (ion's) transport. The embedded nanoparticles provided sites for phosphate to selectively bind to, over other competitive anions, and be transported across under the application of a driving force. The molecular dynamics simulations confirmed our experimental findings and hypothesis that the target ion forms outer-sphere interactions with the embedded nanoparticle that allows for its (ion's) hopping from one site to another, and therefore transport across the membrane. These findings are under review to be published in *Nature Nano, 2022*. This project also served as a basis for a patent application (63/240,682, filed on 9/3/2021).

The results from Chapter 3 demonstrate a new pathway for ion transport in facilitated transport membranes using outer-sphere interactions. The mathematical model suggests that addition of the nanoparticles alters the internal structure of the membrane and affects the membrane's inherent properties such as the ion exchange capacity and water uptake. This could be one of the factors influencing the transport of an anion through the cation exchange membrane.

In essence, although the developed membrane exhibits superior phosphate selectivity over other competitive anions, its ion flux is very low. The membrane with high nanoparticle loading shows that with the current preparation route, this attained loading is the maximum possible. Therefore, future studies could focus on improving nanoparticle loading using different ion exchange polymers, increasing ion-exchange capacity, or perhaps a new preparation route. Studies could also investigate the effect of increasing nanoparticle concentration within the membrane, such as its effect on membrane properties, ion selectivity, and flux. Such highly selective membranes could be employed into other applications requiring specificity, such as Lithium extraction from electronic waste or gold extraction from seawater.

In conclusion, intermolecular interactions play an important role in membrane science, from the CNT percolation threshold required to impart surface electrical conductivity to polymeric membranes to providing highly selective pathways to certain ions over other competitive ions. The understanding of these chemistries at play is crucial to the development of new membranes as well as improving upon existing ones.

References

1. UN-Water. Summary Progress Update 2021 : SDG 6 — water and sanitation for all. *UN-Water Integr. Monit. Initiat.* 1–58 (2021).

2. Ma, T. *et al.* Pollution exacerbates China's water scarcity and its regional inequality. *Nat. Commun.* **11**, 1–9 (2020).

3. Cole, M. J., Bailey, R. M., Cullis, J. D. S. & New, M. G. Spatial inequality in water access and water use in South Africa. *Water Policy* **20**, 37–52 (2018).

4. Carr, J. A., Seekell, D. A. & D'Odorico, P. Inequality or injustice in water use for food? *Environ. Res. Lett.* **10**, (2015).

5. El-Dessouky, H. T., Ettouney, H. M. & Al-Roumi, Y. Multi-stage flash desalination: Present and future outlook. *Chem. Eng. J.* **73**, 173–190 (1999).

6. Youssef, P. G., Al-Dadah, R. K. & Mahmoud, S. M. Comparative analysis of desalination technologies. *Energy Procedia* **61**, 2604–2607 (2014).

7. Cohen, Y. *Advances In Water Desalination Technologies*. (World Scientific Publishing Company, 2021).

8. Elimelech, M. & Phillip, W. A. The future of seawater desalination: Energy, technology, and the environment. *Science* vol. 333 712–717 (2011).

9. Khawaji, A. D., Kutubkhanah, I. K. & Wie, J. M. Advances in seawater desalination technologies. *Desalination* **221**, 47–69 (2008).

10. Lior, N. *Advances in Water Desalination*. *Advances in Water Desalination* (2012). doi:10.1002/9781118347737.

11. Cohen-Tanugi, D. & Grossman, J. C. Water desalination across nanoporous graphene. *Nano Lett.* **12**, 3602–3608 (2012).

12. Shahzad, M. W., Burhan, M., Ang, L. & Ng, K. C. Energy-water-environment nexus underpinning future desalination sustainability. *Desalination* **413**, 52–64 (2017).

13. Eke, J., Yusuf, A., Giwa, A. & Sodiq, A. The global status of desalination: An assessment of current desalination technologies, plants and capacity. *Desalination* **495**, 114633 (2020).

14. Song, J., Li, T., Wright-Contreras, L. & Law, A. W. K. A review of the current status of small-scale seawater reverse osmosis desalination. *Water Int.* **42**, 618–631 (2017).

15. Iddya, A., Rao, U., Wang, J., Su, Y. & Jassby, D. Carbon Nanomaterials in Desalination Process. in *Advances in Water Desalination Technologies* 529–581 doi:10.1142/9789811226984_0015.

16. Bøckman, O. C. Fertilizers and biological nitrogen fixation as sources of plant nutrients: Perspectives for future agriculture. *Plant Soil* **194**, 11–14 (1997).

17. Jorgenson, A. K. & Kuykendall, K. A. Globalization, foreign investment dependence and agriculture production: Pesticide and fertilizer use in less-developed countries, 1990-2000. *Soc. Forces* **87**, 529–560 (2008).

18. Endo, A., Tsurita, I., Burnett, K. & Orencio, P. M. A review of the current state of research on the water, energy, and food nexus. *J. Hydrol. Reg. Stud.* **11**, 20–30 (2017).

19. Council), U. N. (United S. N. I. Global Trends 2030: Alternative Worlds. US. *US NIC, Washingt. DC, USA* 137 (2012).

20. Rasul, G. & Sharma, B. The nexus approach to water–energy–food security: an option for adaptation to climate change. *Clim. Policy* **16**, 682–702 (2016).

21. Bazilian, M. *et al.* Considering the energy, water and food nexus: Towards an integrated modelling approach. *Energy Policy* **39**, 7896–7906 (2011).

22. Allan, T., Keulertz, M. & Woertz, E. The water–food–energy nexus: an introduction to nexus concepts and some conceptual and operational problems. *Int. J. Water Resour. Dev.* **31**, 301–311 (2015).

23. Tran, Q. K., Schwabe, K. A. & Jassby, D. Wastewater reuse for agriculture: Development of a regional water reuse decision-support model (RWRM) for cost-effective irrigation sources. *Environ. Sci. Technol.* **50**, 9390–9399 (2016).

24. Xie, M., Shon, H. K., Gray, S. R. & Elimelech, M. Membrane-based processes for wastewater nutrient recovery: Technology, challenges, and future direction. *Water Res.* **89**, 210–221 (2016).

25. Repetto, R. & Holmes, T. The Role of Population in Resource Depletion in Developing Countries. *Popul. Dev. Rev.* **9**, 609–632 (1983).

26. Kominko, H., Gorazda, K. & Wzorek, Z. The Possibility of Organo-Mineral Fertilizer Production from Sewage Sludge. *Waste and Biomass Valorization* **8**, 1781–1791 (2017).

27. Steffen, W. *et al.* Planetary boundaries: Guiding human development on a changing planet. *Science (80-.).* **347**, (2015).

28. Cai, T., Park, S. Y. & Li, Y. Nutrient recovery from wastewater streams by microalgae: Status and prospects. *Renew. Sustain. Energy Rev.* **19**, 360–369 (2013).

29. Zhang, C. *et al.* Phosphate selective recovery by magnetic iron oxide impregnated carbon flow-electrode capacitive deionization (FCDI). *Water Res.* **189**, 116653 (2021).

30. Cordell, D., Drangert, J. O. & White, S. The story of phosphorus: Global food security and food for thought. *Glob. Environ. Chang.* **19**, 292–305 (2009).

31. Cordell, D., Rosemarin, A., Schröder, J. J. & Smit, A. L. Towards global phosphorus security: A systems framework for phosphorus recovery and reuse options. *Chemosphere* **84**, 747–758 (2011).

32. Berg, U., Knoll, G., Kaschka, E., Weidler, P. G. & Nüesch, R. Is phosphorus recovery from waste water feasible? *Environ. Technol.* **28**, 165–172 (2007).

33. Zhao, D. & Sengupta, A. K. Ultimate removal of phosphate from wastewater using a new class of polymeric ion exchangers. *Water Res.* **32**, 1613–1625 (1998).

34. Cornel, P. & Schaum, C. Phosphorus recovery from wastewater: Needs, technologies and costs. *Water Sci. Technol.* **59**, 1069–1076 (2009).

35. Batstone, D. J., Hülsen, T., Mehta, C. M. & Keller, J. Platforms for energy and nutrient recovery from domestic wastewater: A review. *Chemosphere* **140**, 2–11 (2015).

36. Cheng, J. J. & Stomp, A. M. Growing Duckweed to recover nutrients from wastewaters and for production of fuel ethanol and animal feed. *Clean - Soil, Air, Water* **37**, 17–26 (2009).

37. Wang, Y., Huang, X. & Yuan, Q. Nitrogen and carbon removals from food processing wastewater by an anoxic/aerobic membrane bioreactor. *Process Biochem.* **40**, 1733–1739 (2005).

38. Yan, T. *et al.* A critical review on membrane hybrid system for nutrient recovery from wastewater. *Chem. Eng. J.* **348**, 143–156 (2018).

39. Cohen, Y. *Nutrient recovery from wastewater*. (Svedish University of Agricultural Sciences, 2015).

40. Hong, S. P. *et al.* Selective phosphate removal using layered double hydroxide/reduced graphene oxide (LDH/rGO) composite electrode in capacitive deionization. *J. Colloid Interface Sci.* **564**, 1–7 (2020).

41. Stratful, I., Brett, S., Scrimshaw, M. B. & Lester, J. N. Biological phosphorus removal, its role in phosphorus recycling. *Environ. Technol. (United Kingdom)* **20**, 681–695 (1999).

42. Van Loosdrecht, M. C. M., Hooijmans, C. M., Brdjanovic, D. & Heijnen, J. J. Biological phosphate removal processes. *Appl. Microbiol. Biotechnol.* **48**, 289–296 (1997).

43. Pfromm, P. H. Towards sustainable agriculture: Fossil-free ammonia. *J. Renew. Sustain. Energy* **9**, (2017).

44. Hou, D. *et al.* Nickel-Based Membrane Electrodes Enable High-Rate Electrochemical Ammonia Recovery. *Environ. Sci. Technol.* **52**, 8930–8938 (2018).

45. Candido, L. & Gomes, J. A. C. P. Evaluation of anode materials for the electro-oxidation of ammonia and ammonium ions. *Mater. Chem. Phys.* **129**, 1146–1151 (2011).

46. Rosso, D., Larson, L. E. & Stenstrom, M. K. Aeration of large-scale municipal wastewater treatment plants: State of the art. *Water Sci. Technol.* **57**, 973–978 (2008).

47. Liu, H., Ramnarayanan, R. & Logan, B. E. Production of Electricity during Wastewater Treatment Using a Single Chamber Microbial Fuel Cell. *Environ. Sci. Technol.* **38**, 2281–2285 (2004).

48. Venkatesh, G. & Brattebø, H. Energy consumption, costs and environmental impacts for urban water cycle services: Case study of Oslo (Norway). *Energy* **36**, 792–800 (2011).

49. Elías-Maxil, J. A., Van Der Hoek, J. P., Hofman, J. & Rietveld, L. Energy in the urban water cycle: Actions to reduce the total expenditure of fossil fuels with emphasis on heat

reclamation from urban water. *Renew. Sustain. Energy Rev.* **30**, 808–820 (2014).

50. Maurer, M. Ã., Pronk, W. & Larsen, T. A. Treatment processes for source-separated urine. **40**, 3151–3166 (2006).

51. Tarpeh, W. A., Barazesh, J. M., Cath, T. Y. & Nelson, K. L. Electrochemical Stripping to Recover Nitrogen from Source-Separated Urine. *Environ. Sci. Technol.* **52**, 1453–1460 (2018).

52. Iddya, A. *et al.* Efficient ammonia recovery from wastewater using electrically conducting gas stripping membranes. *Environ. Sci. Nano* **7**, 1759–1771 (2020).

53. Cui, Z. F. & Muralidhara, H. S. Membrane Technology. *Membr. Technol.* **3**, 184–249 (2010).

54. Abdullah, N., Rahman, M. A., Othman, M. H. D., Jaafar, J. & Ismail, A. F. *Membranes and Membrane Processes: Fundamentals. Current Trends and Future Developments on (Bio-) Membranes: Photocatalytic Membranes and Photocatalytic Membrane Reactors* (Elsevier Inc., 2018). doi:10.1016/B978-0-12-813549-5.00002-5.

55. Baker, R. W. (Richard W. *Membrane technology and applications*. *J. Wiley* (2004).

56. Lee, A., Elam, J. W. & Darling, S. B. Membrane materials for water purification: Design, development, and application. *Environ. Sci. Water Res. Technol.* **2**, 17–42 (2016).

57. Baker, R. W. & Low, B. T. Gas separation membrane materials: A perspective. *Macromolecules* **47**, 6999–7013 (2014).

58. Koros, W. J. & Fleming, G. K. Membrane-based gas separation. *J. Memb. Sci.* **83**, 1–80 (1993).

59. Luis, P. *Membrane contactors*. *Fundamental Modeling of Membrane Systems: Membrane and Process Performance* (Elsevier Inc., 2018). doi:10.1016/B978-0-12-813483-2.00005-8.

60. Luis, P. Membrane contactors. *Fundam. Model. Membr. Syst. Membr. Process Perform.* 153–208 (2018) doi:10.1016/B978-0-12-813483-2.00005-8.

61. Gabelman, A. & Hwang, S. Hollow fiber membrane contactors. **159**, (1999).

62. Sata, T. Studies on anion exchange membranes having permselectivity for specific anions in electrodialysis - Effect of hydrophilicity of anion exchange membranes on permselectivity of anions. *J. Memb. Sci.* **167**, 1–31 (2000).

63. Alabi, A. *et al.* Review of nanomaterials-assisted ion exchange membranes for electromembrane desalination. *npj Clean Water* **1**, (2018).

64. Luo, T., Abdu, S. & Wessling, M. Selectivity of ion exchange membranes: A review. *J. Memb. Sci.* **555**, 429–454 (2018).

65. Strathmann, H. Electrodialysis, a mature technology with a multitude of new applications. *Desalination* **264**, 268–288 (2010).

66. Zhao, W. Y. *et al.* Waste conversion and resource recovery from wastewater by ion

exchange membranes: State-of-the-art and perspective. *Ind. Eng. Chem. Res.* **57**, 6025–6039 (2018).

67. Asante-Sackey, D., Rathilal, S., Kweinor Tetteh, E., Ezugbe, E. O. & Pillay, L. V. Donnan membrane process for the selective recovery and removal of target metal ions—a mini review. *Membranes (Basel).* **11**, 1–16 (2021).

68. Parvizian, F., Hosseini, S. M., Hamidi, A. R., Madaeni, S. S. & Moghadassi, A. R. Electrochemical characterization of mixed matrix nanocomposite ion exchange membrane modified by ZnO nanoparticles at different electrolyte conditions 'pH/concentration'. *J. Taiwan Inst. Chem. Eng.* **45**, 2878–2887 (2014).

69. Cassady, H. J., Cimino, E. C., Kumar, M. & Hickner, M. A. Specific ion effects on the permselectivity of sulfonated poly(ether sulfone) cation exchange membranes. *J. Memb. Sci.* **508**, 146–152 (2016).

70. Donnan, F. G. The theory of membrane equilibria. *Chem. Rev.* **1**, 73–90 (1924).

71. Gierke, T. D., Munn, G. E. & Wilson, F. C. Morphology in Nafion Perfluorinated Membrane Products, As Determined By Wide- and Small-Angle X-Ray Studies. *J. Polym. Sci. Part A-2, Polym. Phys.* **19**, 1687–1704 (1981).

72. Saito, M., Arimura, N., Hayamizu, K. & Okada, T. Mechanisms of ion and water transport in perfluorosulfonated ionomer membranes for fuel cells. *J. Phys. Chem. B* **108**, 16064–16070 (2004).

73. Porozhnyy, M., Huguet, P., Cretin, M., Safronova, E. & Nikonenko, V. Mathematical modeling of transport properties of proton-exchange membranes containing immobilized nanoparticles. *Int. J. Hydrogen Energy* **41**, 15605–15614 (2016).

74. Subramonian, S. & Clifford, D. Monovalent/divalent selectivity and the charge separation concept. *React. Polym. Ion Exch. Sorbents* **9**, 195–209 (1988).

75. Tzanetakis, N. *et al.* Comparative performance of ion exchange membranes for electrodialysis of nickel and cobalt. *Sep. Purif. Technol.* **30**, 113–127 (2003).

76. Nagarale, R. K., Shahi, V. K., Thampy, S. K. & Rangarajan, R. Studies on electrochemical characterization of polycarbonate and polysulfone based heterogeneous cation-exchange membranes. *React. Funct. Polym.* **61**, 131–138 (2004).

77. Tandon, R. & Pintauro, P. N. Divalent/monovalent cation uptake selectivity in a Nafion cation-exchange membrane: Experimental and modeling studies. *J. Memb. Sci.* **136**, 207–219 (1997).

78. Stenina, I., Golubenko, D., Nikonenko, V. & Yaroslavtsev, A. Selectivity of transport processes in ion-exchange membranes: Relationship with the structure and methods for its improvement. *Int. J. Mol. Sci.* **21**, 1–33 (2020).

79. Stenina, I. A. & Yaroslavtsev, A. B. Ionic Mobility in Ion - Exchange Membranes. *Membranes (Basel).* **11**, (2021).

80. Stenina, I. A. & Yaroslavtsev, A. B. Nanomaterials for lithium-ion batteries and hydrogen

energy. *Pure Appl. Chem.* **89**, 1185–1194 (2017).

81. Bernardo, P. & Clarizia, G. 30 Years of Membrane Technology for Gas Separation. **32**, 1999–2004 (2013).

82. Ismail, A. F., Khulbe, K. C. & Matsuura, T. *Gas Separation Membranes*. (2015). doi:10.1007/978-3-319-01095-3.

83. Noble, R. D. & Koval, C. A. Review of Facilitated Transport Membranes. *Mater. Sci. Membr. Gas Vap. Sep.* 411–435 (2006) doi:10.1002/047002903X.ch17.

84. Suss, M. E. *et al.* Water desalination via capacitive deionization: What is it and what can we expect from it? *Energy Environ. Sci.* **8**, 2296–2319 (2015).

85. Tang, C. & Bruening, M. L. Ion separations with membranes. *J. Polym. Sci.* **58**, 2831–2856 (2020).

86. Li, Y. *et al.* Facilitated transport of small molecules and ions for energy-efficient membranes. *Chem. Soc. Rev.* **44**, 103–118 (2015).

87. Cussler, E. L., Aris, R. & Bhown, A. On the limits of facilitated diffusion. *J. Memb. Sci.* **43**, 149–164 (1989).

88. Ferraz, H. C. *et al.* Recent achievements in facilitated transport membranes for separation processes. *Brazilian J. Chem. Eng.* **24**, 101–118 (2007).

89. Noble, R. D. Facilitated transport mechanism in fixed site carrier membranes. *J. Memb. Sci.* **60**, 297–306 (1991).

90. Almeida, M. I. G. S., Cattrall, R. W. & Kolev, S. D. Recent trends in extraction and transport of metal ions using polymer inclusion membranes (PIMs). *J. Memb. Sci.* **415**–**416**, 9–23 (2012).

91. Liu, W. *et al.* Embedding dopamine nanoaggregates into a poly(dimethylsiloxane) membrane to confer controlled interactions and free volume for enhanced separation performance. *J. Mater. Chem. A* 3713–3723 (2013) doi:10.1039/c3ta00766a.

92. Zumdahl, S. S. Chemical principles. 94 (1995).

93. Ebbing, D. D. & Gammon, S. D. Chemical principles. (2000).

94. Atkins, P. W. (Peter W. & Jones, L. Chemistry : molecules, matter & change. (1997).

95. Rimai, D. S. & Quesnel, D. J. Particle adhesion. *Adhes. Sci. Eng.* 139–191 (2002) doi:10.1016/B978-044451140-9/50003-2.

96. Stumm, W. The Inner-Sphere Surface Complex. in *Acquatic Chemistry* 1–32 (1995). doi:10.1021/ba-1995-0244.ch001.

97. Sposito, G. Adsorption as a Problem in Coordination Chemistry. in *Acquatic Chemistry* 33–57 (1995). doi:10.1021/ba-1995-0244.ch002.

98. Eaton, D. R. Outer Sphere Complexes As Intermediates in Coordination Chemistry. *Res. Chem. Intermed.* **9**, 201–232 (1988).

99. Kuznetsov, V. V. Outer-sphere Complexes in Analytical Chemistry. *Russ. Chem. Rev.* **55**, 1409–1433 (1986).

100. Iddya, A., Rao, U., Wang, J., Su, Y. & Jassby, D. Carbon Nanomaterials in Desalination Process. in *Advances in Water Desalination Technologies* 529–281 (2021). doi:https://doi.org/10.1142/9789811226984_0015.

101. Popov, V. N. Carbon nanotubes : properties and application. **43**, 61–102 (2004).

102. Duan, W. *et al.* Electrochemical mineral scale prevention and removal on electrically conducting carbon nanotube-polyamide reverse osmosis membranes. *Environ. Sci. Process. Impacts* **16**, 1300–1308 (2014).

103. Dudchenko, A. V., Rolf, J., Russell, K., Duan, W. & Jassby, D. Organic fouling inhibition on electrically conducting carbon nanotube-polyvinyl alcohol composite ultrafiltration membranes. *J. Memb. Sci.* **468**, 1–10 (2014).

104. Duan, W., Ronen, A., Walker, S. & Jassby, D. Polyaniline-Coated Carbon Nanotube Ultrafiltration Membranes: Enhanced Anodic Stability for in Situ Cleaning and Electro-Oxidation Processes. *ACS Appl. Mater. Interfaces* **8**, 22574–22584 (2016).

105. Tang, L. *et al.* Enhanced Flux and Electrochemical Cleaning of Silicate Scaling on Carbon Nanotube-Coated Membrane Distillation Membranes Treating Geothermal Brines. *ACS Appl. Mater. Interfaces* acsami.7b12615 (2017) doi:10.1021/acsami.7b12615.

106. Xie, B. *et al.* Engineering carbon nanotubes enhanced hydrophobic membranes with high performance in membrane distillation by spray coating. *J. Memb. Sci.* **625**, 118978 (2021).

107. Ma, L. *et al.* Fabrication and water treatment application of carbon nanotubes (CNTs)-based composite membranes: A review. *Membranes (Basel).* **7**, (2017).

108. Abdalla, S. & Al-ghamdi, A. A. Different Technical Applications of Carbon Nanotubes. *Nanoscale Res. Lett.* (2015) doi:10.1186/s11671-015-1056-3.

109. Liu, Y. *et al.* Recent advances on electroactive CNT-based membranes for environmental applications : The perfect match of electrochemistry and membrane separation. *Chinese Chem. Lett.* **31**, 2539–2548 (2020).

110. Zhu, X. & Jassby, D. Electroactive Membranes for Water Treatment : Enhanced Treatment Functionalities , Energy Considerations , and Future Challenges. (2019) doi:10.1021/acs.accounts.8b00558.

111. Dudchenko, A. V., Rolf, J., Russell, K., Duan, W. & Jassby, D. Organic fouling inhibition on electrically conducting carbon nanotube-polyvinyl alcohol composite ultrafiltration membranes. *J. Memb. Sci.* **468**, 1–10 (2014).

112. Dudchenko, A. V *et al.* Frequency dependent stability of CNT joule heaters in ionizable environments: implications for desalination.

113. Duan, W. *et al.* Electrochemical removal of hexavalent chromium using electrically conducting carbon nanotube/polymer composite ultrafiltration membranes. *J. Memb. Sci.* **531**, 160–171 (2017).

114. Rao, U. *et al.* Mineral Scale Prevention on Electrically Conducting Membrane Distillation Membranes Using Induced Electrophoretic Mixing. *Environ. Sci. Technol.* **54**, 3678–3690 (2020).

115. Dudchenko, A. V., Chen, C., Cardenas, A., Rolf, J. & Jassby, D. Frequency-dependent stability of CNT Joule heaters in ionizable media and desalination processes. *Nat. Nanotechnol.* **12**, 557–563 (2017).

116. Gong, S., Zhu, Z. H. & Haddad, E. I. Modeling electrical conductivity of nanocomposites by considering carbon nanotube deformation at nanotube junctions. *J. Appl. Phys.* **114**, (2013).

117. Li, C., Thostenson, E. T. & Chou, T. W. Dominant role of tunneling resistance in the electrical conductivity of carbon nanotube-based composites. *Appl. Phys. Lett.* **91**, (2007).

118. Yu, L., Shearer, C. & Shapter, J. Recent Development of Carbon Nanotube Transparent Conductive Films. *Chemical Reviews* vol. 116 13413–13453 (2016).

119. Xie, M., Shon, H. K., Gray, S. R. & Elimelech, M. Membrane-based processes for wastewater nutrient recovery: Technology, challenges, and future direction. *Water Res.* **89**, 210–221 (2016).

120. Rulkens, W. H., Klapwijk, A. & Willers, H. C. Recovery of valuable nitrogen compounds from agricultural liquid wastes: Potential possibilities, bottlenecks and future technological challenges. *Environ. Pollut.* **102**, 727–735 (1998).

121. Afif, A. *et al.* Ammonia-fed fuel cells: A comprehensive review. *Renew. Sustain. Energy Rev.* **60**, 822–835 (2016).

122. Zamfirescu, C. & Dincer, I. Ammonia as a green fuel and hydrogen source for vehicular applications. *Fuel Process. Technol.* **90**, 729–737 (2009).

123. Muster, T. H. & Jermakka, J. Electrochemically-assisted ammonia recovery from wastewater using a floating electrode. *Water Sci. Technol.* **75**, 1804–1811 (2017).

124. Zhang, C., Ma, J., He, D. & Waite, T. D. Capacitive Membrane Stripping for Ammonia Recovery (CapAmm) from Dilute Wastewaters. *Environ. Sci. Technol. Lett.* acs.estlett.7b00534 (2017) doi:10.1021/acs.estlett.7b00534.

125. Pfromm, P. H. Towards sustainable agriculture: Fossil-free ammonia. *J. Renew. Sustain. Energy* **9**, (2017).

126. Hou, D. *et al. Nickel Based Membrane Electrodes Enable High Rate Electrochemical Ammonia Recovery. Environmental Science & Technology* (2018). doi:10.1021/acs.est.8b01349.

127. Dewil, R., Baeyens, J. & Goutvrind, R. Ultrasonic treatment of waste activated sludge. *Environ. Prog.* **25**, 121–128 (2006).

128. Liu, Y. Chemically reduced excess sludge production in the activated sludge process. *Chemosphere* **50**, 1–7 (2003).

129. Shin, C., McCarty, P. L., Kim, J. & Bae, J. Pilot-scale temperate-climate treatment of

domestic wastewater with a staged anaerobic fluidized membrane bioreactor (SAF-MBR). *Bioresour. Technol.* **159**, 95–103 (2014).

130. Harb, M. & Hong, P. Anaerobic Membrane Bioreactor Effluent Reuse: A Review of Microbial Safety Concerns. *Fermentation* **3**, 39 (2017).

131. Lettinga, G., Field, J., Van Lier, J., Zeeman, G. & Hulshoff Pol, L. W. Advanced anaerobic wastewater treatment in the near future. *Water Sci. Technol.* **35**, 5–12 (1997).

132. Kartal, B., Kuenen, J. G. & Van Loosdrecht, M. C. M. Sewage treatment with anammox. *Science (80-.).* **328**, 702–703 (2010).

133. Strous, M., Van Gerven, E., Zheng, P., Kuenen, J. G. & Jetten, M. S. M. Ammonium removal from concentrated waste streams with the anaerobic ammonium oxidation (anammox) process in different reactor configurations. *Water Res.* **31**, 1955–1962 (1997).

134. He, Qingyao, Tu, Te, Yan, Shuiping, Yang, Xing, Duke, Mikel, Zhang, Yanlin, Zhao, S. Relating water vapor transfer to ammonia recovery from biogas slurry by vacuum membrane distillation. *Sep. Purif. Technol.* **191**, 182–191 (2018).

135. Masse, L., Massé, D. I., Pellerin, Y. & Dubreuil, J. Osmotic pressure and substrate resistance during the concentration of manure nutrients by reverse osmosis membranes. *J. Memb. Sci.* **348**, 28–33 (2010).

136. Bonmatı, A. & Flotats, X. Air stripping of ammonia from pig slurry: characterisation and feasibility as a pre- or post-treatment to mesophilic anaerobic digestion. *Waste Manag.* **23**, 261–272 (2003).

137. Tao, W. & Ukwuani, A. T. Coupling thermal stripping and acid absorption for ammonia recovery from dairy manure: Ammonia volatilization kinetics and effects of temperature, pH and dissolved solids content. *Chem. Eng. J.* **280**, 188–196 (2015).

138. Milan, Z. *et al.* Ammonia removal from anaerobically treated piggery manure by ion exchange in columns packed with homoionic zeolite. *Chem. Eng. J.* **66**, 65–71 (1997).

139. Uludag-Demirer, S., Demirer, G. N. & Chen, S. Ammonia removal from anaerobically digested dairy manure by struvite precipitation. *Process Biochem.* **40**, 3667–3674 (2005).

140. Etter, B., Tilley, E., Khadka, R. & Udert, K. M. Low-cost struvite production using source-separated urine in Nepal. *Water Res.* **45**, 852–862 (2011).

141. Jordaan, E. M., Ackerman, J. & Cicek, N. Phosphorus removal from anaerobically digested swine wastewater through struvite precipitation. *Water Sci. Technol.* **61**, 3228–3234 (2010).

142. Hou, D., Jassby, D., Nerenberg, R. & Ren, Z. J. Hydrophobic Gas Transfer Membranes for Wastewater Treatment and Resource Recovery. *Environ. Sci. Technol.* **53**, 11618–11635 (2019).

143. Singer, S. *et al.* Anaerobic membrane gas extraction facilitates thermophilic hydrogen production from Clostridium thermocellum. *Environ. Sci. Water Res. Technol.* **4**, 1771–1782 (2018).

144. Mumpton, F. A. & Fishman, p H. THE APPLICATION OF NATURAL ZEOLITES IN

ANIMAL SCIENCE AND AQUACULTURE. *J. Anim. Sci.* **45**, 1188–1203 (1977).

145. Malaisamy, R., Talla-Nwafo, A. & Jones, K. L. Polyelectrolyte modification of nanofiltration membrane for selective removal of monovalent anions. *Sep. Purif. Technol.* **77**, 367–374 (2011).

146. Tran, A. T. K. *et al.* Phosphate pre-concentration from municipal wastewater by selectrodialysis: Effect of competing components. *Sep. Purif. Technol.* **141**, 38–47 (2015).

147. EL-Bourawi, M. S. *et al.* Application of vacuum membrane distillation for ammonia removal. *J. Memb. Sci.* **301**, 200–209 (2007).

148. Renard, J. J., Calidonna, S. E. & Henley, M. V. Fate of ammonia in the atmosphere - A review for applicability to hazardous releases. *J. Hazard. Mater.* **108**, 29–60 (2004).

149. Ding, Z., Liu, L., Li, Z., Ma, R. & Yang, Z. Experimental study of ammonia removal from water by membrane distillation (MD): The comparison of three configurations. *J. Memb. Sci.* **286**, 93–103 (2006).

150. M. J. Rothrock Jr., A. A. Szögi & M. B. Vanotti. Recovery of Ammonia from Poultry Litter Using Gas-Permeable Membranes. *Trans. ASABE* **53**, 1267–1275 (2010).

151. Kuntke, P., Zamora, P., Saakes, M., Buisman, C. J. N. & Hamelers, H. V. M. Gas-permeable hydrophobic tubular membranes for ammonia recovery in bio-electrochemical systems. *Environ. Sci. Water Res. Technol.* **2**, 261–265 (2016).

152. Emerson, K., Russo, R., Lund, R. & Thurston, R. Aqueous Ammonia Equilibrium Calculations: Effect of pH and Temperature. *J. Fish. Res. Board Canada* **32**, 2379–2383 (1975).

153. Kartohardjono, S. *et al.* The removal of dissolved ammonia from wastewater through a polypropylene hollow fiber membrane contactor. *Int. J. Technol.* **6**, 1146–1152 (2015).

154. Tarpeh, W. A., Barazesh, J. M., Cath, T. Y. & Nelson, K. L. Electrochemical Stripping to Recover Nitrogen from Source-Separated Urine. *Environ. Sci. Technol.* **52**, 1453–1460 (2018).

155. Christiaens, M. E. R. *et al.* Electrochemical Ammonia Recovery from Source-Separated Urine for Microbial Protein Production. *Environ. Sci. Technol.* **51**, 13143–13150 (2017).

156. Rodríguez Arredondo, M., Kuntke, P., ter Heijne, A., Hamelers, H. V. M. & Buisman, C. J. N. Load ratio determines the ammonia recovery and energy input of an electrochemical system. *Water Res.* **111**, 330–337 (2017).

157. Luther, A. K., Desloover, J., Fennell, D. E. & Rabaey, K. Electrochemically driven extraction and recovery of ammonia from human urine. *Water Res.* **87**, 367–377 (2015).

158. TERADA, A., HIBIYA, K., NAGAI, J., TSUNEDA, S. & HIRATA, A. Nitrogen Removal Characteristics and Biofilm Analysis of a Membrane-Aerated Biofilm Reactor Applicable to High-Strength Nitrogenous Wastewater Treatment. *J. Biosci. Bioeng.* **95**, 170–178 (2003).

159. Lu, L., Huang, Z., Rau, G. H. & Ren, Z. J. Microbial Electrolytic Carbon Capture for Carbon

Negative and Energy Positive Wastewater Treatment. *Environ. Sci. Technol.* **49**, 8193–8201 (2015).

160. Tang, L. *et al.* Enhanced Flux and Electrochemical Cleaning of Silicate Scaling on Carbon Nanotube-Coated Membrane Distillation Membranes Treating Geothermal Brines. *ACS Appl. Mater. Interfaces* **9**, (2017).

161. Ukwuani, A. T. & Tao, W. Developing a vacuum thermal stripping – acid absorption process for ammonia recovery from anaerobic digester effluent. *Water Res.* **106**, 108–115 (2016).

162. Khayet, M. Membranes and theoretical modeling of membrane distillation: A review. *Adv. Colloid Interface Sci.* **164**, 56–88 (2011).

163. Tomaszewska, M. Preparation and properties of flat-sheet membranes from poly(vinylidene fluoride) for membrane distillation. *Desalination* **104**, 1–11 (1996).

164. Zhou, Y. *et al.* Flame-like Ni(OH) 2 strongly promotes the dissociation of water and can be used to produce an excellent hybrid electrocatalyst for the hydrogen evolution reaction in alkaline media. *Electrochem. commun.* **91**, 66–70 (2018).

165. Gong, M. *et al.* Nanoscale nickel oxide/nickel heterostructures for active hydrogen evolution electrocatalysis. *Nat. Commun.* **5**, 1–6 (2014).

166. Grdeń, M., Alsabet, M. & Jerkiewicz, G. Surface science and electrochemical analysis of nickel foams. *ACS Appl. Mater. Interfaces* **4**, 3012–3021 (2012).

167. Yu, X. *et al.* Nickel-based thin film on multiwalled carbon nanotubes as an efficient bifunctional electrocatalyst for water splitting. *ACS Appl. Mater. Interfaces* **6**, 15395–15402 (2014).

168. Hou, D. *et al.* Preparation, characterization and performance of a novel visible light responsive spherical activated carbon-supported and Er 3+ :YFeO 3 -doped TiO 2 photocatalyst. *J. Hazard. Mater.* **199**–**200**, 301–308 (2012).

169. Xu, C. *et al.* Electrodeposition mechanism and characterization of Ni–Mo alloy and its electrocatalytic performance for hydrogen evolution. *Int. J. Hydrogen Energy* **41**, 13341–13349 (2016).

170. Fan, C., Piron, D. L. & Paradis, P. Hydrogen evolution on electrodeposited nickel-cobalt-molybdenum in alkaline water electrolysis. *Electrochim. Acta* **39**, 2715–2722 (1994).

171. Mitov, M., Chorbadzhiyska, E., Nalbandian, L. & Hubenova, Y. Nickel-based electrodeposits as potential cathode catalysts for hydrogen production by microbial electrolysis. *J. Power Sources* **356**, 467–472 (2017).

172. Shetty, S., Mohamed Jaffer Sadiq, M., Bhat, D. K. & Hegde, A. C. Electrodeposition and characterization of Ni-Mo alloy as an electrocatalyst for alkaline water electrolysis. *J. Electroanal. Chem.* **796**, 57–65 (2017).

173. Tilley, S. D. *et al.* Water photolysis at 12.3% efficiency via perovskite photovoltaics and Earth-abundant catalysts. *Science (80-.).* **345**, 1593–1596 (2014).

174. Li, Z.-F., Wang, Y. & Botte, G. G. Revisiting the electrochemical oxidation of ammonia on carbon-supported metal nanoparticle catalysts. *Electrochim. Acta* **228**, 351–360 (2017).

175. Binninger, T., Fabbri, E., Kötz, R. & Schmidt, T. J. Determination of the Electrochemically Active Surface Area of Metal-Oxide Supported Platinum Catalyst. *J. Electrochem. Soc.* **161**, H121–H128 (2013).

176. Cord-Ruwisch, R., Law, Y. & Cheng, K. Y. Ammonium as a sustainable proton shuttle in bioelectrochemical systems. *Bioresour. Technol.* **102**, 9691–9696 (2011).

177. Kuntke, P. *et al.* (Bio) electrochemical ammonia recovery : progress and perspectives. *Appl. Microbiol. Biotechnol.* **2**, 3865–3878 (2018).

178. Popat, S. C., Ki, D., Rittmann, B. E. & Torres, C. I. Importance of OH-transport from cathodes in microbial fuel cells. *ChemSusChem* **5**, 1071–1079 (2012).

179. Biedermann, P. U. *et al.* Near-surface ion distribution and buffer effects during electrochemical reactions. *Phys. Chem. Chem. Phys.* **13**, 16384 (2011).

180. Katsounaros, I. *et al.* The effective surface pH during reactions at the solid-liquid interface. *Electrochem. commun.* **13**, 634–637 (2011).

181. Zhang, C., Ma, J., He, D. & Waite, T. D. SI: Capacitive Membrane Stripping for Ammonia Recovery (CapAmm) from Dilute Wastewaters. *Environ. Sci. Technol. Lett.* acs.estlett.7b00534 (2017) doi:10.1021/acs.estlett.7b00534.

182. Abu-Zeid, M. A. E. R. *et al.* A comprehensive review of vacuum membrane distillation technique. *Desalination* **356**, 1–14 (2015).

183. Izquierdo-Gil, M. A. & Jonsson, G. Factors affecting flux and ethanol separation performance in vacuum membrane distillation (VMD). *J. Memb. Sci.* **214**, 113–130 (2003).

184. Abu-Zeid, M. A. E. R. *et al.* A comprehensive review of vacuum membrane distillation technique. *Desalination* vol. 356 1–14 (2015).

185. Dykstra, J. E., Biesheuvel, P. M., Bruning, H. & Ter Heijne, A. Theory of ion transport with fast acid-base equilibrations in bioelectrochemical systems. *Phys. Rev. E - Stat. Nonlinear, Soft Matter Phys.* **90**, 1–10 (2014).

186. Chiam, C. K. & Sarbatly, R. Vacuum membrane distillation processes for aqueous solution treatment-A review. *Chem. Eng. Process. Process Intensif.* **74**, 27–54 (2014).

187. Lu, L., Hou, D., Wang, X., Jassby, D. & Ren, Z. J. Active H 2 Harvesting Prevents Methanogenesis in Microbial Electrolysis Cells. *Environ. Sci. Technol. Lett.* **3**, 286–290 (2016).

188. Kuntke, P., Sleutels, T. H. J. A., Saakes, M. & Buisman, C. J. N. Hydrogen production and ammonium recovery from urine by a Microbial Electrolysis Cell. *Int. J. Hydrogen Energy* **39**, 4771–4778 (2014).

189. Jackson, D. T. & Nelson, P. N. Preparation and properties of some ion selective membranes: A review. *J. Mol. Struct.* **1182**, 241–259 (2019).

190. Uliana, A. A. *et al.* Ion-capture electrodialysis using multifunctional adsorptive membranes. *Science (80-.).* **372**, 296–299 (2021).

191. Paltrinieri, L. *et al.* Hybrid polyelectrolyte-anion exchange membrane and its interaction with phosphate. *React. Funct. Polym.* **133**, 126–135 (2018).

192. Zhou, Y., Hu, C., Liu, H. & Qu, J. Potassium-Ion Recovery with a Polypyrrole Membrane Electrode in Novel Redox Transistor Electrodialysis. *Environ. Sci. Technol.* **54**, 4592–4600 (2020).

193. Harris, S. M. *et al.* Gadolinium Complex for the Catch and Release of Phosphate from Water. *Environ. Sci. Technol.* **51**, 4549–4558 (2017).

194. Pan, B. *et al.* New strategy to enhance phosphate removal from water by hydrous manganese oxide. *Environ. Sci. Technol.* **48**, 5101–5107 (2014).

195. Blaney, L. M., Cinar, S. & SenGupta, A. K. Hybrid anion exchanger for trace phosphate removal from water and wastewater. *Water Res.* **41**, 1603–1613 (2007).

196. Bowden, L. I., Jarvis, A. P., Younger, P. L. & Johnson, K. L. Phosphorus removal from waste waters using basic oxygen steel slag. *Environ. Sci. Technol.* **43**, 2476–2481 (2009).

197. Pitakteeratham, N., Hafuka, A., Satoh, H. & Watanabe, Y. High efficiency removal of phosphate from water by zirconium sulfate-surfactant micelle mesostructure immobilized on polymer matrix. *Water Res.* **47**, 3583–3590 (2013).

198. Liu, R. *et al.* Effective and selective adsorption of phosphate from aqueous solution via trivalent-metals-based amino-MIL-101 MOFs. *Chem. Eng. J.* **357**, 159–168 (2019).

199. Pan, B. *et al.* Development of polymer-based nanosized hydrated ferric oxides (HFOs) for enhanced phosphate removal from waste effluents. *Water Res.* **43**, 4421–4429 (2009).

200. Tor, A. Removal of fluoride from water using anion-exchange membrane under Donnan dialysis condition. *J. Hazard. Mater.* **141**, 814–818 (2007).

201. Khor, C. M. *et al.* Electrically Mediated Membrane Pore Gating via Grafted Polymer Brushes. *ACS Mater. Lett.* **1**, 647–654 (2019).

202. Paltrinieri, L. *et al.* Functionalized Anion-Exchange Membranes Facilitate Electrodialysis of Citrate and Phosphate from Model Dairy Wastewater. *Environ. Sci. Technol.* **53**, 2396–2404 (2019).

203. Ounissi, T., Dammak, L., Larchet, C., Fauvarque, J. F. & Selmane Bel Hadj Hmida, E. Novel lithium selective composite membranes: synthesis, characterization and validation tests in dialysis. *J. Mater. Sci.* **55**, 16111–16128 (2020).

204. Scindia, Y. M., Pandey, A. K. & Reddy, A. V. R. Coupled-diffusion transport of Cr(VI) across anion-exchange membranes prepared by physical and chemical immobilization methods. *J. Memb. Sci.* **249**, 143–152 (2005).

205. Ramakrishnam Raju, M. V., Harris, S. M. & Pierre, V. C. Design and applications of metal-based molecular receptors and probes for inorganic phosphate. *Chem. Soc. Rev.* **49**, 1090–1108 (2020).

206. Acelas, N. Y., Martin, B. D., López, D. & Jefferson, B. Selective removal of phosphate from wastewater using hydrated metal oxides dispersed within anionic exchange media. *Chemosphere* **119**, 1353–1360 (2015).

207. Fransiscus, Y., Widi, R. K., Aprilasti, G. O. & Yuharma, M. D. Adsorption of phosphate in aqueous solutions using manganese dioxide. *Int. J. Adv. Sci. Eng. Inf. Technol.* **8**, 818–824 (2018).

208. Yao, W. & Millero, F. J. Adsorption of phosphate on manganese dioxide in seawater. *Environ. Sci. Technol.* **30**, 536–541 (1996).

209. Kawashima, M., Tainaka, Y., Hori, T., Koyama, M. & Takamatsu, T. Phosphate adsorption onto hydrous manganese(IV) oxide in the presence of divalent cations. *Water Res.* **20**, 471–475 (1986).

210. Mustafa, S., Zaman, M. I. & Khan, S. Temperature effect on the mechanism of phosphate anions sorption by β-MnO2. *Chem. Eng. J.* **141**, 51–57 (2008).

211. Su, Q. *et al.* Fabrication of polymer-supported nanosized hydrous manganese dioxide (HMO) for enhanced lead removal from waters. *Sci. Total Environ.* **407**, 5471–5477 (2009).

212. Pan, B. C. *et al.* Highly effective removal of heavy metals by polymer-based zirconium phosphate: A case study of lead ion. *J. Colloid Interface Sci.* **310**, 99–105 (2007).

213. Tongwen, X. & Weihua, Y. Fundamental studies of a new series of anion exchange membranes: Membrane preparation and characterization. *J. Memb. Sci.* **190**, 159–166 (2001).

214. Tuan, L. X. & Buess-Herman, C. Study of water content and microheterogeneity of CMS cation exchange membrane. *Chem. Phys. Lett.* **434**, 49–55 (2007).

215. Lim, T. M., Ulaganathan, M. & Yan, Q. *Advances in membrane and stack design of redox flow batteries (RFBs) for medium- and large-scale energy storage. Advances in Batteries for Medium and Large-Scale Energy Storage: Types and Applications* (Elsevier Ltd., 2015). doi:10.1016/B978-1-78242-013-2.00014-5.

216. Kamcev, J., Paul, D. R. & Freeman, B. D. Effect of fixed charge group concentration on equilibrium ion sorption in ion exchange membranes. *J. Mater. Chem. A* **5**, 4638–4650 (2017).

217. Warwick, C., Guerreiro, A. & Soares, A. Sensing and analysis of soluble phosphates in environmental samples: A review. *Biosens. Bioelectron.* **41**, 1–11 (2013).

218. Luo, H., Agata, W. A. S. & Geise, G. M. Connecting the Ion Separation Factor to the Sorption and Diffusion Selectivity of Ion Exchange Membranes. *Ind. Eng. Chem. Res.* **59**, 14189–14206 (2020).

219. Larchet, C., Auclair, B. & Nikonenko, V. Approximate evaluation of water transport number in ion-exchange membranes. *Electrochim. Acta* **49**, 1711–1717 (2004).

220. Fuller, T. F. & Newman, J. Experimental Determination of the Transport Number of Water in Nafion 117 Membrane. *J. Electrochem. Soc.* **139**, 1332–1337 (1992).

221. Chakrabarty, T. *et al.* Stable ion-exchange membranes for water desalination by electrodialysis. *Desalination* **282**, 2–8 (2011).

222. Wang, X., Nie, Y., Zhang, X., Zhang, S. & Li, J. Recovery of ionic liquids from dilute aqueous solutions by electrodialysis. *Desalination* **285**, 205–212 (2012).

223. Li, P. & Merz, K. M. Metal Ion Modeling Using Classical Mechanics. *Chem. Rev.* **117**, 1564–1686 (2017).

224. Wang, J., Wolf, R. M., Caldwell, J. W., Kollman, P. A. & Case, D. A. Development and testing of a general Amber force field. *J. Comput. Chem.* **25**, 1157–1174 (2004).

225. Li, Z., Song, L. F., Li, P. & Merz, K. M. Systematic Parametrization of Divalent Metal Ions for the OPC3, OPC, TIP3P-FB, and TIP4P-FB Water Models. *J. Chem. Theory Comput.* **16**, 4429–4442 (2020).

226. Izadi, S. & Onufriev, A. V. Accuracy limit of rigid 3-point water models. *J. Chem. Phys.* **145**, (2016).

227. Zarzycki, P. & Gilbert, B. Temperature-dependence of the dielectric relaxation of water using non-polarizable water models. *Phys. Chem. Chem. Phys.* **22**, 1011–1018 (2020).

228. R. W. G. Wyckoff. Crystal Structures. *Mineral. Mag.* **4**, (1968).

229. Berendsen, H. J. C., Postma, J. P. M., Van Gunsteren, W. F., Dinola, A. & Haak, J. R. Molecular dynamics with coupling to an external bath. *J. Chem. Phys.* **81**, 3684–3690 (1984).

230. Goga, N., Rzepiela, A. J., De Vries, A. H., Marrink, S. J. & Berendsen, H. J. C. Efficient algorithms for langevin and DPD dynamics. *J. Chem. Theory Comput.* **8**, 3637–3649 (2012).

231. D.A. Case, S.R. Brozell, D.S. Cerutti, T.E. Cheatham, V.W.D. Cruzeiro, T.A. Darden, R.E. Duke, D. Ghoreishi, H. Gohlke, A.W. Goetz, D. Greene, R. Harris, N. Homeyer, S. Izadi, A. Kovalenko, T.S. Lee, S. LeGrand, L.B. Li, C. Lin, J. Liu, T. Luchko, R. Luo, P. A. K. AMBER 2018. *San Fr. Univ. Calif.* (2018).

232. Berendsen, H. J. C., van der Spoel, D. & van Drunen, R. GROMACS: A message-passing parallel molecular dynamics implementation. *Comput. Phys. Commun.* **91**, 43–56 (1995).

233. Zhang, B., Gao, H., Xiao, C., Tong, X. & Chen, Y. The trade-off between membrane permselectivity and conductivity: A percolation simulation of mass transport. *J. Memb. Sci.* **597**, 117751 (2020).

234. Nikonenko, V. *et al.* Modelling of ion transport in electromembrane systems: Impacts of membrane bulk and surface heterogeneity. *Appl. Sci.* **9**, (2018).

235. Gohil, G. S., Shahi, V. K. & Rangarajan, R. Comparative studies on electrochemical characterization of homogeneous and heterogeneous type of ion-exchange membranes. *J. Memb. Sci.* **240**, 211–219 (2004).

236. Ariono, D., Khoiruddin, Subagjo & Wenten, I. G. Heterogeneous structure and its effect on properties and electrochemical behavior of ion-exchange membrane. *Mater. Res. Express*

4, (2017).

237. Kingsbury, R. S. & Coronell, O. Modeling and validation of concentration dependence of ion exchange membrane permselectivity: Significance of convection and Manning's counter-ion condensation theory. *J. Memb. Sci.* **620**, 118411 (2020).

238. Kamcev, J., Paul, D. R., Manning, G. S. & Freeman, B. D. Ion Diffusion Coefficients in Ion Exchange Membranes: Significance of Counterion Condensation. *Macromolecules* **51**, 5519–5529 (2018).

239. Kim, S. K., Shin, D. M. & Rhim, J. W. Designing a high-efficiency hypochlorite ion generation system by combining cation exchange membrane aided electrolysis with chlorine gas recovery stream. *J. Memb. Sci.* **630**, 119318 (2021).

240. Galama, A. H. *et al.* Membrane resistance: The effect of salinity gradients over a cation exchange membrane. *J. Memb. Sci.* **467**, 279–291 (2014).

241. Berkowitz, M. & Wan, W. The limiting ionic conductivity of Na+ and Cl- ions in aqueous solutions: Molecular dynamics simulation. *J. Chem. Phys.* **86**, 376–382 (1987).

242. Bian, Y., Chen, X. & Ren, Z. J. pH dependence of phosphorus speciation and transport in flow-electrode capacitive deionization pH dependence of phosphorus speciation and transport in flow-electrode capacitive deionization. *Environ. Sci. Technol.* (2020) doi:10.1021/acs.est.0c01836.

243. Nesbitt, H. W. & Banerjee, D. Interpretation of XPS Mn(2p) spectra of Mn oxyhydroxides and constraints on the mechanism of MnO2 precipitation. *Am. Mineral.* **83**, 305–315 (1998).

244. Yang, Z. *et al.* Vertically-aligned Mn(OH)2 nanosheet films for flexible all-solid-state electrochemical supercapacitors. *J. Mater. Sci. Mater. Electron.* **28**, 17533–17540 (2017).

245. Parikh, S. J. & Chorover, J. FTIR spectroscopic study of biogenic Mn-oxide formation by Pseudomonas putida GB-1. *Geomicrobiol. J.* **22**, 207–218 (2005).

246. Wang, X. & Andrews, L. Infrared spectra of M(OH) (M = Mn, Fe, Co, Ni) molecules in solid argon and the character of first row transition metal hydroxide bonding. *J. Phys. Chem. A* **110**, 10035–10045 (2006).

247. Nagarale, R. K., Gohil, G. S., Shahi, V. K. & Rangarajan, R. Preparation and electrochemical characterizations of cation-exchange membranes with different functional groups. *Colloids Surfaces A Physicochem. Eng. Asp.* **251**, 133–140 (2004).

248. Berezina, N. P., Kononenko, N. A., Dyomina, O. A. & Gnusin, N. P. Characterization of ion-exchange membrane materials: Properties vs structure. *Adv. Colloid Interface Sci.* **139**, 3–28 (2008).

249. Mulijani, S., Dahlan, K. & Wulanawati, A. Sulfonated Polystyrene Copolymer: Synthesis, Characterization and Its Application of Membrane for Direct Methanol Fuel Cell (DMFC). *Int. J. Mater. Mech. Manuf.* **2**, 36–40 (2014).

250. Sun, Z. *et al.* Electrostatic shield effect: An effective way to suppress dissolution of polysulfide anions in lithium-sulfur battery. *J. Mater. Chem. A* **2**, 15938–15944 (2014).

251. Othman, M. H. D., Ismail, A. F. & Mustafa, A. Physico-Chemical Study of Sulfonated Poly(Ether Ether Ketone) Membranes for Direct Methanol Fuel Cell Application. *Malaysian Polym. J.* **2**, 10–28 (2007).

252. Lee, E. B., Meng, Q. B., Shin, J. & Lee, Y. S. Preparation and characterization of crosslinked sulfonated poly(ether ether ketone) membranes using 4-vinylbenzyl chloride via electron beam irradiation and subsequent Friedel-Craft reaction. *Macromol. Res.* **22**, 1090–1095 (2014).

253. Jashni, E., Hosseini, S. M., Shen, J. N. & Van der Bruggen, B. Electrochemical characterization of mixed matrix electrodialysis cation exchange membrane incorporated with carbon nanofibers for desalination. *Ionics (Kiel).* **25**, 5595–5610 (2019).

254. Kingsbury, R. S., Zhu, S., Flotron, S. & Coronell, O. Microstructure Determines Water and Salt Permeation in Commercial Ion-Exchange Membranes. *ACS Appl. Mater. Interfaces* **10**, 39745–39756 (2018).

255. NIST X-ray Photoelectron Spectroscopy Database. NIST Standard Reference Database Number 20. *Natl. Inst. Stand. Technol. Gaithersbg. MD, 20899* (retrieved 2021-02-26). doi:10.18434/T4T88K.

256. Luo, F. *et al.* Magnetic amino-functionalized lanthanum metal-organic framework for selective phosphate removal from water. *Colloids Surfaces A Physicochem. Eng. Asp.* 125906 (2020) doi:10.1016/j.colsurfa.2020.125906.

257. Wu, B., Fang, L., Fortner, J. D., Guan, X. & Lo, I. M. C. Highly efficient and selective phosphate removal from wastewater by magnetically recoverable La(OH)3/Fe3O4 nanocomposites. *Water Res.* **126**, 179–188 (2017).

258. Hassan, M. H., Stanton, R., Secora, J., Trivedi, D. J. & Andreescu, S. Ultrafast Removal of Phosphate from Eutrophic Waters Using a Cerium-Based Metal–Organic Framework. *ACS Appl. Mater. Interfaces* **0**, acsami.0c16477 (2020).

259. Kononenko, N. *et al.* Porous structure of ion exchange membranes investigated by various techniques. *Adv. Colloid Interface Sci.* **246**, 196–216 (2017).

260. Lopez, M., Kipling, B. & Yeager, H. L. Ionic Diffusion and Selectivity of a Cation Exchange Membrane in Nonaqueous Solvents. *Anal. Chem.* **49**, 629–632 (1977).

261. Rottiers, T., De la Marche, G., Van der Bruggen, B. & Pinoy, L. Co-ion fluxes of simple inorganic ions in electrodialysis metathesis and conventional electrodialysis. *J. Memb. Sci.* **492**, 263–270 (2015).

262. White, N., Misovich, M., Yaroshchuk, A. & Bruening, M. L. Coating of Nafion membranes with polyelectrolyte multilayers to achieve high monovalent/divalent cation electrodialysis selectivities. *ACS Appl. Mater. Interfaces* **7**, 6620–6628 (2015).

263. Hosseini, S. M., Jeddi, F., Nemati, M., Madaeni, S. S. & Moghadassi, A. R. Electrodialysis heterogeneous anion exchange membrane modified by PANI/MWCNT composite nanoparticles: Preparation, characterization and ionic transport property in desalination. *Desalination* **341**, 107–114 (2014).

264. Tang, L. *et al.* Highly Efficient, Stable, and Recyclable Hydrogen Manganese Oxide/Cellulose Film for the Extraction of Lithium from Seawater. *ACS Appl. Mater. Interfaces* **12**, 9775–9781 (2020).

265. Sunarso, J. *et al.* Characterization of hybrid organic and inorganic functionalised membranes for proton conduction. **179**, 477–482 (2008).

266. Munir, M. T. *et al.* Phosphate recovery from hydrothermally treated sewage sludge using struvite precipitation. *Bioresour. Technol.* **239**, 171–179 (2017).